Velocimetry-based pressure information for spray analysis – novel experimental, processing and evaluation strategies

Zur Erlangung des akademischen Grades eines
DOKTORS DER INGENIEURWISSENSCHAFTEN (Dr.-Ing.)

von der KIT-Fakultät für Maschinenbau des
Karlsruher Instituts für Technologie (KIT)
angenommene

DISSERTATION

von

M.Sc. Nils Herbert Kling

Tag der mündlichen Prüfung:	28. Juli 2022
Hauptreferentin:	Prof. Dr.-Ing. B. Frohnapfel
Korreferent:	Prof. Dr. rer. nat. habil. C. J. Kähler

Acknowledgements

First and foremost, I would like to thank Prof. Bettina Frohnapfel for giving me the opportunity to work on the present research project at the Institute of Fluid Mechanics (ISTM) at the Karlsruhe Institute of Technology (KIT) and for providing me with extensive support in the process. I would also like to thank Prof. Christian Kähler for refereeing this thesis. I fondly remember the encouraging dinner talk at the Lisbon laser symposium 2018 that reinforced my intention to develop the DPSA technique. From an operations view, I want to thank the Robert Bosch GmbH for supporting and funding the research project.
I would like to offer my special thanks to Jochen Kriegseis, Lars Opfer and Philipp Rogler for their great support, expertise and encouragement during my research. Thank you for your trust and provision of a free, agile and fruitful way of working, which allowed me to pursue the research in breadth and depth. Your feedback pushed me to sharpen my thinking.
I want to thank former colleagues of the Robert Bosch GmbH and the Institute of Fluid Mechanics. Many thanks to Dmitrii Mamaikin and Maximilian Miller for the great time and well-founded friendship. I also would like to thank former students Miao Zhang, Florian Haller and Kerrin Fischer for their work and dedication.
During my research I enjoyed great support from dear people outside of work. Particularly, I would like to thank Maike, Petra, Theresa and Til for sharing their happiness and charity with me. You have reminded me that there is so much more to life – something that people like me often forget.
Finally, I want to thank my family for their never-ending love. Without the support, empathy and patience of my parents, Inge and Jürgen, my studies would not have been possible. You have always promoted the very best in all of your doings – miraculously nothing, no matter how burdensome, has been able to stop you. Another miracle for which I am very grateful is the birth of my nephew Theodor and niece Matilda. Thanks to my dear sister Pia and her husband Michael for gifting our family two lovely souls.

Schätze,
die man im Geist aufbewahrt,
vermodern nicht.

(Japanisches Sprichwort)

Abstract

In the present thesis, the spray transport of complex gasoline direct injection (GDI) sprays was investigated by means of velocimetry-based pressure evaluation. For this purpose, novel experimental, processing and evaluation strategies were introduced to qualify pressure evaluation of spray-induced flow and expand its capabilities. This includes a statistical approach based on the Unsteady Reynolds-Averaged Navier-Stokes (URANS) equations and ensemble averaging that allows for velocimetry-based pressure evaluation of unsteady, statistically stationary flows by means of standard Particle Image Velocimetry (PIV). Further, a novel technique referred to as Dual-Plane Stereo Astigmatism (DPSA) was developed which enables the evaluation of instantaneous pressure fields and thus the analysis of individual injection events using a stereoscopic setup and a single light source. Lastly, the data-driven modelling technique of Physics-Informed Neural Networks (PINNs) was successfully adopted from the field of deep learning to experimental fluid mechanics and spray analysis. The technique of PINNs extends the limits of current velocimetry-based pressure evaluation and enables the evaluation of yet hidden flow regimes, both in space and time.
Using the developed methods, the interplay between spray and ambient gas flow was studied for varying operating conditions and spray layouts. It was shown that the momentum exchange increases with higher injection pressure, gas density, fuel temperature, greater relative velocity, larger spray-gas interface, spray expansion, stronger atomisation and flash-boiling. As a major finding, it was revealed that the deflection of spray respectively the phenomena of jet-to-jet interaction and spray contraction is traced back to a net momentum exerting on individual spray plumes as a result of pressure forces that are induced by the interplay between spray and ambient gas flow. In this context, the presence of the so far hypothesised lower pressures in the centre area of multi-hole sprays was experimentally confirmed. It was shown that the effect of jet-to-jet interaction and spray contraction is facilitated by a narrow spray layout and targeting, strong atomisation and enhanced droplet tracking behaviour.

Kurzfassung

In der vorliegenden Arbeit wurde der Spraytransport von komplexen Benzindirekteinspritzungssprays (GDI) mittels auf Geschwindigkeitmessung basierter Druckauswertung untersucht. Für diesen Zweck wurden neue Versuchs-, Verarbeitungs- und Auswertestrategien eingeführt, um eine Druckauswertung der Spray-induzierten Strömung zu befähigen und deren Möglichkeiten auszuweiten. Dies umfasst unter anderem ein statistisches Verfahren auf Basis der Unsteady Reynolds-Averaged Navier-Stokes (URANS) Gleichungen und Ensemble-Mittelung, welche die Druckauswertung transienter, statistisch stationärer Strömungen mittels konventioneller Particle Image Velocimetry (PIV) ermöglicht. Darüber hinaus wurde eine neuartige Technik namens Dual-Plane-Stereo-Astigmatismus (DPSA) entwickelt, die die Auswertung momentaner Druckfelder und damit die Analyse einzelner Einspritzereignisse unter Verwendung eines stereoskopischen Aufbaus und einer einzigen Lichtquelle ermöglicht. Abschließend wurde die Methode der Physics-Informed Neural Networks (PINNs) erfolgreich aus dem Bereich des Deep Learnings in die experimentelle Strömungsmechanik und Spray-Analyse übertragen. Das PINN-Verfahren weitet die Möglichkeiten der bisherigen auf Geschwindigkeitsmessung basierenden Druckauswertung aus und ermöglicht die Auswertung von bislang nicht auswertbaren Strömungsbereichen, sowohl in Raum und Zeit. Unter Verwendung der beschriebenen Methoden wurde die Wechselwirkung zwischen Spray und Umgebungsgasströmung für unterschiedliche Betriebsbedingungen und Sprayauslegungen untersucht. Es zeigte sich, dass der Impulsaustausch mit höherem Einspritzdruck, Gasdichte, Kraftstofftemperatur, größerer Relativgeschwindigkeit, Spray-Gas-Grenzfläche, Sprayexpansion und stärkerer Zerstäubung bzw. Flash-Boiling zunimmt. Als eine wesentliche Erkenntnis wurde festgestellt, dass die Ablenkung von Sprays bzw. das Phänomen der Strahl-zu-Strahl-Wechselwirkung und Spraykontraktion auf einen Nettoimpuls zurückzuführen ist, der auf einzelne Spraykeulen infolge von induzierten Druckkräften wirkt. In diesem

Zusammenhang wurde das Vorhandensein eines Niederdruckgebiets im Zentrum von Mehrlochsprays experimentell bestätigt. Es wurde aufgezeigt, dass das Ausmaß der Strahl-zu-Strahl-Wechselwirkung und der Spraykontraktion durch eine enge Spritzlochanordnung und -ausrichtung, eine starke Zerstäubung und ein erhöhtes Tropfen-Folgeverhalten begünstigt wird.

Contents

1 Introduction

1.1 Motivation

In the design and development of gasoline direct injection (GDI), the realisation of a good mixture preparation and the prevention of combustion chamber wetting are decisive for the optimisation of performance, efficiency and particle emissions [1, 2]. Due to the large range of engine operating points (torque, speed, combustion chamber flow, etc.), thermodynamic conditions (cold start, warmed-up engine, etc.) and operating strategies (multiple injection, start of injection, etc.), the provision of a robust and tailored spray represents a particular challenge for the design and layout of injection systems. Depending on the operating conditions, injector design and spray layout, the spray transport is largely determined by the interplay between spray and ambient gas flow as well as by the upstream, preconditioning mechanisms of internal nozzle flow, atomisation, flash-boiling and droplet break-up.
In the range of typical engine operating points, the spray transport of conventional GDI multi-hole sprays can be subject to considerable variation as illustrated in Figure 1.1. As a function of fuel temperature, injection pressure and ambient gas pressure, the spray transport transitions from a separate propagation of individual spray plumes to a full contraction of the spray into a single, unified jet. Such a change in spray transport is usually met with significant implications on mixture preparation and engine combustion [1–3]. While an efficient, well-guided spray transport enables a highly-desired, premixed and evenly distributed combustion across the combustion chamber, an unfavourable, less well-guided spray transport results in an imperfect mixture homogenisation with proportions of lean and rich combustion which should be avoided in view of efficient and low-emission combustion. In this regard, a rather undesirable event is due to strongly penetrating sprays, which are typically observed under

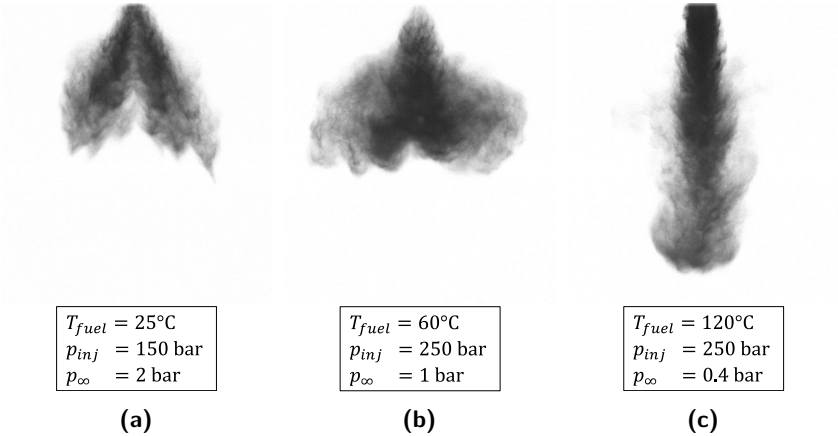

Figure 1.1: The influence of thermodynamic conditions on the spray transport of a GDI 6-hole nozzle visualised by processed shadowgraphy images at the same time after start of injection (SOI) – transition from non-contracting (a) to contracting sprays (b, c). $T_\infty = 25°C$ is the ambient gas temperature, p_{inj} is the injection pressure, p_∞ is the ambient gas pressure and T_{fuel} is the fuel temperature. n-Heptane was used as fuel.

specific conditions for contracted multi-hole sprays as shown in Figure 1.1c. Such sprays typically bear the increased risk of combustion chamber wall wetting [3], which is associated with rich, non-premixed combustion, increased soot formation and potential formation of deposits and hotspots [4–7]. With the introduction of the EU6-RDE cycle [8], ensuring good mixture preparation and spray transport have become more important as a greater coverage in the engine map and a larger share of dynamic driving is stipulated.

In order to improve and optimise today's systems and processes, great efforts are being made in research and development. In this context, multiple experimental and numerical investigations were devoted to the characterisation and evaluation of sprays. Apart from traditional testing and spray visualisation such as shadowgraphy, schlieren imaging and spray patternation, more extensive investigations [9] were carried out using advanced optical measurement technology like particle-image, laser-Doppler

or phase-Doppler velocimetry (PIV, LDV, PDV) [10, 11]. Major correlations concerning spray properties such as spray penetration [12, 13], spray cone angle [13, 14], droplet size/distribution/velocity [11], spray pattern [15, 16] and spray and ambient gas velocities [15–27] were derived for varying operating conditions [23, 28–36], spray layouts and nozzle design parameters [26, 37]. A strong interplay between spray and ambient gas flow was revealed by PIV-investigations on spray-induced flow. In the works of Lee *et al.* [15, 16] simultaneous PIV-snapshots of the spray and ambient gas flow of a GDI spray showed a strong interrelation between spray transport, momentum exchange and surrounding gas flow for different ambient gas pressures and split injection events. In line with spray formation, a vortex-like structure is found to be a possible characteristic flow pattern of the spray-induced flow of contracted GDI multi-hole sprays. In this respect, a stronger momentum exchange was reported for elevated ambient pressures by Prosperi *et al.* [22] and Sepret *et al.* [23], and smaller droplet sizes and greater spray expansions by Zhang *et al.* [27]. Beyond the above-mentioned efforts, Zhang *et al.* [30] provided a sound phenomenological characterisation of the spray contraction process from individually propagating spray plumes to a single unified jet using laser-light-sheet imaging and PIV. Parametric studies by Krämer *et al.* [32] and Payri *et al.* [38] showed an increased tendency for spray contraction with narrow spray layouts and targetings, higher spray-hole numbers, larger injection pressures, higher fuel temperatures and higher ambient gas temperatures and densities. Furthermore, it was shown that the process of spray contraction can be inhibited by shorter injection durations as a result of reduced interaction between spay and ambient gas. In addition to experimental studies, further investigations were conducted using computational fluid mechanics (CFD) to explore the fundamental cause of spray contraction and to derive crucial information about the conditions and design parameters under which spray contraction occurs. Based on computed pressure fields of contracting and non-contracting multi-hole sprays, Weber [39] reported the presence of a lower pressure region in the centre of sprays, which was hypothesised to be responsible for the contraction of spray by exerting a deflective force on the spray plumes. The observation of a central lower pressure region was confirmed in successive numerical studies [40–42].

Despite these earlier efforts, a more thorough understanding of spray transport or a validation of numerical studies and existing hypotheses is still

pending, as highly-desired experimental data on the momentum exchange between spray and ambient gas flow, and pressure field information of the gaseous phase are yet not available. Even though numerical simulations have strongly contributed to the current understanding of sprays, their application is so far limited to either highly simplified models given the complexity of the physics, or direct numerical simulations (DNS) that usually cover sub-areas like the injector near field or primary atomisation [9]. The CFD study of complex sprays with a high level of detail is not practicable by today's standards, nor is it conceivable to carry out extensive parameter studies on different nozzle design parameters or operating conditions.
In the field of experimental fluid mechanics, however, a promising approach has evolved in recent years that allows the evaluation of pressure fields based on time-resolved velocity data, usually obtained by Particle Image Velocimetry (PIV) [10]. The so-called 'pressure from PIV' method [43, 44] was so far applied to several different flows [45–47], however, an application to sprays and GDI is still pending, as both the velocimetry and pressure evaluation pose a great challenge in multiple respects.
Successful pressure evaluation of spray-induced flow would provide highly-anticipated information on the interrelation between spray transport, momentum exchange and ambient gas flow. The cause-effect relationship between spray transport, operating conditions and nozzle design parameters would be accessible as well as special spray transport phenomena such as jet-to-jet interaction and spray contraction.

1.2 Objectives and outline

The superordinate objective of the present work is the analysis of spray transport and spray-gas interaction of complex gasoline direct injection (GDI) sprays by means of velocimetry-based pressure evaluation. The present thesis attempts to experimentally identify and characterise essential cause-effect relationships between spray transport, momentum exchange and ambient gas flow as a function major injection parameters such as operating conditions, spray layout and spray targeting. Due to the large influence on spray transport and subsequent processes such as mixture preparation and engine combustion, a special concern of the present work is the investigation and assessment of the mechanism of jet-to-jet interaction.

Especially the phenomenon of spray contraction is of vital interest as it strongly affects the propagation and characteristics of spray.
In this context, a major focus of the thesis is the qualification of velocimetry-based pressure evaluation [44, 48] for spray-induced flow analysis. Due to the high requirements and limiting factors, the application is regarded as particularly challenging. Besides the need for time-resolved volumetric velocimetry and small length and time scales, the presence of low signal-to-noise ratios due to intense multi-scattering and the necessary phase separation by optical filtering and fluorescent particle seeding require the use of sophisticated measurement technology and processing techniques as well as carefully executed and well-designed experiments. For such conditions and requirements, tomographic PIV (Tomo-PIV) [49] is generally considered as suitable. However, within the bounds of the present thesis the measurement technology is limited to a stereoscopic setup that is generally not capable of performing pressure from PIV due to its lack of out-of-plane gradient determination.
Therefore, in the framework of the present work, two different techniques were developed to enable velocimetry-based pressure evaluation by means of stereoscopic PIV (stereo-PIV) for future spray investigations. On the one hand a statistical approach [50] based on the Unsteady Reynolds-Averaged Navier-Stokes (URANS) equations and on the other hand a novel approach referred to as Dual-Plane Stereo Astigmatism (DPSA) [51]. The statistical approach allows for the reconstruction of ensemble-averaged velocity fields based on multiple spatial and temporal independent measurements in order to fully characterise the governing equations. The DPSA technique, on the other hand, enables the determination of the full velocity gradient tensor in planar domain by means of astigmatism-based depth codification and image processing. In contrast to the statistical approach, the DPSA technique allows for the evaluation of unsteady pressure fields of single injection events.
Finally, in order to enhance the current capability of spray-induced flow evaluation, a promising method from the field of deep learning is introduced to velocimetry-based pressure evaluation and spray analysis. The method, which is generally known as physics-informed neuronal network (PINN) [52, 53], is a data-driven modelling approach that takes advantage of the powerful merits of neural networks to fully exploit the potential of available data and a priori information such as laws of physics and empirical correlations. In the present work, a PINN architecture is presented,

that allows for the pressure evaluation of spray-induced flow in yet hidden flow regimes, where no velocimetry data is available, such as the area of optically dense sprays, by utilising the equations of mass and momentum conservation.
The thesis is structured as follows. An overview of atomisation and sprays including the associated mechanisms of internal nozzle flow, cavitation and aerodynamic forces is given in Chapter 2. Chapter 3 outlines the principles of stereo-PIV and the specifics of its application to spray-induced flow velocimetry. In Chapter 4, the fundamentals of pressure from PIV and the principles of the statistical approach based on URANS and ensemble averaging are presented. Chapter 5 describes the basic experimental setup and its specific adaptation for the velocimetry of spray-induced flow. In Chapter 6, the statistical approach for pressure from PIV is applied to the spray-induced flow of a two-hole spray. For the purpose of validation, the pressure evaluation is assessed by a comparative pressure measurement with a piezoelectric pressure sensor. Apart from that, an uncertainty quantification of the pressure evaluation was performed to gain valuable insights into the propagation of errors and to derive best practice knowledge for pressure evaluation. In addition, a scale and sensitivity analysis of the governing equations is carried out to identify potential measures for the optimisation of the used methodology. In chapters 7 and 8, the developed pressure evaluation of spray-induced flow is used to investigate the interplay between spray and ambient gas flow including the phenomena of jet-to-jet interaction and spray contraction. The spray transport and momentum exchange between spray and ambient gas flow is studied for varying injection pressures, fuel temperatures and ambient gas pressure under flash-boiling and non-flash-boiling conditions. For the investigation, various spray layouts and targetings are used ranging from single jets in Chapter 7 up to 3-hole sprays and complex GDI multi-hole sprays in Chapter 8. In Chapter 9, the methodology of the Dual-Plane Stereo Astigmatism (DPSA) approach is presented. The DPSA approach is demonstrated on both synthetic and experimental data. A thorough analysis of different processing schemes is given. In Chapter 10, the deep learning approach of physics-informed neuronal networks (PINN) is introduced and applied to velocimetry-based pressure evaluation of spray-induced flow. Based on incomplete velocimetry data, the full velocity and pressure field of a contracted, dense multi-hole spray is evaluated. The result of the PINN-based pressure evaluation is compared with conventional pressure from PIV processing.

Overall, each chapter provides a comprehensive overview of the state of the art. For the sake of clarity, a nomenclature was chosen that is consistent with the literature of the respective fields of study (e.g. fluid mechanics, PIV, deep learning). The chapters 6-10 close with a subsequent discussion and/or concluding remark. Finally, the research and development of the present thesis is concluded in Chapter 11. A detailed overview and classification of the major findings is given, while promising research topics and potential trends are outlined.

2 Fundamentals of atomisation and sprays

The atomisation of spray describes the process of liquid bulk disintegration into small fractions of ligaments and droplets (primary atomisation) and the subsequent breakup into smaller fragments (secondary atomisation) [54]. Disrupting liquid velocities, turbulence and aerodynamic forces but also disturbances in form of surface displacements and fluctuations in thermodynamic and material properties such as pressure, temperature, surface tension, density and viscosity may lead to the growth of instabilities and eventually to the breakup of the liquid [54]. The disintegration of a liquid bulk generally requires surface tension forces to be overcome by disruptive forces. In GDI, pressure atomisers with plain orifices are used to discharge and disintegrate liquid fuel under high pressure by converting pressure energy into kinetic energy and eventually surface tension energy and viscous dissipation. Sprays generated by such pressure atomisers are classified into different breakup regimes [55, 56]. In Figure 2.1 the breakup regimes are shown as a function of the liquid jet velocity v_l. The classification is based on macroscopic spray characteristics such as the length of the intact liquid column L_{jet} and the size of the resulting droplets. With increasing jet velocity, a distinction is made between dripping, Rayleigh, first-wind-induced regime, second-wind-induced regime and atomisation regime [56]. Due to the high injection pressures and discharge velocities, the injection event in GDI takes place almost exclusively in the atomisation regime, in which the liquid jet disintegrates at the nozzle in a highly chaotic and irregular manner [54]. The resulting droplet diameters are considerably smaller than the spray hole diameter. The other breakup regimes are confined in time to the nozzle opening and closing events, which is traced back to a throttling at the needle seat and thus lower jet velocities. A detailed review of the breakup regimes is given in Lefebvre & McDonell [54].

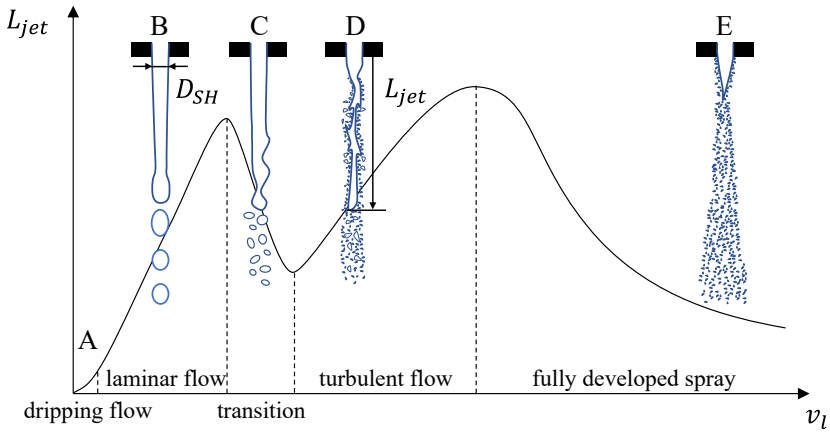

Figure 2.1: Spray characteristics and breakup regimes for pressure atomisers with plane orifices as a function of jet velocity. Regimes: (A) dripping, (B) Rayleigh, (C) first wind-induced regime, (D) second wind-induced regime, (E) atomisation regime. Adapted from Lefebvre & McDonell [54].

For the characterisation of atomisation, various non-dimensional numbers are typically used. Key figures are the Weber number We, the Ohnesorge number Oh and the Reynolds number Re. The Weber number describes the ratio of inertial forces to surface tension forces. It indicates whether a liquid is stable or tends to break up. For the analysis in the present work, the liquid Weber number We_l is used to characterise the disintegration tendency of a liquid due to the interaction between spray and surrounding gas flow. The liquid Weber number is given by

$$We_l = \frac{\rho_l v_{rel}^2 l}{\sigma_l} = \frac{\rho_l v_{rel}^2 D_{SH}}{\sigma_l}, \tag{2.1}$$

where ρ_l is the liquid density, l is a characteristic length scale (here $l = D_{SH}$), D_{SH} is the spray hole diameter, v_{rel} is the relative velocity between the liquid and gaseous phases and σ_l is the liquid surface tension. The Weber number does not take into account viscous effects. Viscosity generally inhibits the growth of instabilities and delays the onset of disintegration. To account for viscosity, the Ohnesorge number is commonly used. The

Ohnesorge number Oh describes the ratio between viscous forces on the one hand and inertial and surface forces on the other hand. It is given by

$$Oh = \frac{\mu_l}{\sqrt{\rho_l \sigma_l l}} = \frac{\mu_l}{\sqrt{\rho_l \sigma_l D_{SH}}}, \tag{2.2}$$

where μ_l is the dynamic viscosity of the liquid. Qualitatively, the lower the Ohnesorge number, the more energy is converted into surface tension energy and the stronger the tendency of the liquid to disintegrate. Conversely, the higher the Ohnesorge number, the more dominant the viscous dissipation and the lower the tendency to break up. The Ohnesorge number is a velocity and flow rate independent quantity. It is specified by the material properties and the geometry of the fluid (here specified by the spray hole diameter D_{SH}). To characterise the flow and its effect on atomisation, the Reynolds number is used. The Reynolds number relates inertia forces to viscous forces. In the present work, the liquid jet Reynolds number

$$Re_l = \frac{\rho_l v_l l}{\mu_l} = \frac{\rho_l v_l D_{SH}}{\mu_l} \tag{2.3}$$

is employed to describe the internal nozzle flow.

2.1 GDI sprays and terminology

Figure 2.2 schematically shows the nozzle geometry and spray layout of a conventional GDI multi-hole nozzle. There are various design parameters that influence and control the processes of spray formation. Key design parameters are the number of spray holes (with or without pre-hole step), their orientation and arrangement as well as their individual spray-hole lengths L_{SH} and spray-hole diameters D_{SH} [54, 57, 58]. Some designs feature conical and/or rounded spray holes to favourably influence the flow pattern [59].
In the field of GDI, the term 'spray targeting' is used to describe the target directions of the individual spray plumes. The spray targeting is largely defined by the geometric orientation of the spray holes. Due to the influence of various processes including internal nozzle flow, atomisation and spray-gas interaction, the actual trajectories of the spray plumes generally differ from the nominal spray targeting [32, 60, 61].

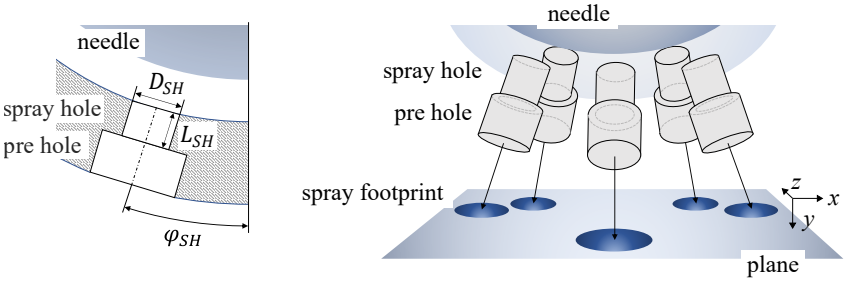

Figure 2.2: Schematical illustration and terminology of a typical gasoline direct injection (GDI) nozzle; left: internal nozzle geometry, where φ_{SH} describes the spray-hole angle; right: multi-hole spray layout and targeting.

2.2 Spray formation

In the following sections, the principles of atomisation and spray transport including the mechanisms of internal nozzle flow, cavitation and aerodynamic forces are presented briefly. For more detailed information, the reader is referred to Lefebvre & McDonell [54], Ashgriz [62] and Brennen [63].

2.2.1 Internal nozzle flow

The internal nozzle flow of a pressure atomiser significantly determines the quality of primary atomisation and thus strongly influences the subsequent processes of secondary atomisation and spray-gas interaction [64]. Depending on the nozzle geometry, surface roughness, turbulence, cavitation, fluid properties, injection pressure and velocity, the internal nozzle flow exhibits perturbing radial velocities, turbulent structures and instabilities which may overcome the cohesive surface tension forces and eventually result in the breakup of the liquid.
Internal nozzle flows with pronounced radial velocities at the spray-hole outlet show commonly an increased level of atomisation [65]. A key design parameter of pressure atomisers with plain orifices is the ratio of the spray-hole length L_{SH} and spray-hole diameter D_{SH}. The L_{SH}/D_{SH} ratio determines, inter alia, whether the flow at the spray hole outlet is

more regular/aligned or rather chaotic with stronger radial velocities. In GDI, flow separations due to severe geometric changes, typically at the spray hole inlet or due to cavitation, often have a significant impact on the flow pattern [57, 66, 67], both by introducing additional turbulence and irregularities to the flow. It shall be noted, that a fully turbulent liquid jet can disintegrate without the presence of external forces such as aerodynamic forces [54]. Turbulent structures can dissolve from the main corpus and form droplets or ligaments, while small-scale structures may disrupt the surface topology. However, even if there are no radial velocity components at the nozzle exit, shear stresses in the liquid jet lead to a relaxation of the velocity profile and the formation of potentially perturbing radial velocities after discharge.

2.2.2 Cavitation

In GDI, the phase transition from the liquid to the vapour phase plays a pivotal role in atomisation. In general, two different processes are distinguished – cavitation and boiling [63, 68]. Both processes are based on similar mechanisms, however the thermodynamic paths are different, as shown in the phase diagram in Figure 2.3. While cavitation describes the isothermal process of nucleation in a liquid that occurs when the pressure p falls below the saturation vapour pressure p_v, boiling refers to the isobaric process of nucleation when the temperature T rises above the saturation temperature T_s. If a liquid is superheated ($T - T_s > 0$) or in tension ($p_v - p > 0$), a spontaneous phase transition from the metastable to a stable state may occur due to local instabilities starting from vapour-bubble nucleation through bubble growth to eventually liquid-vapour equilibrium. The level of superheat and tension depends on the purity of the liquid, wall roughness, fluctuations and temporal time scales [63]. The faster the process of isobaric heating or isothermal depressurisation, the more intense the evaporation. The extent to which a fluid can be superheated or brought in tension without evaporation is determined by the spinodal curve $(\partial p/\partial v)_T = 0$, where v is the specific volume. A prerequisite for phase transition is the presence of sufficient nucleation [63]. Nucleation is distinguished by two different types, homogeneous and heterogeneous nucleation. In homogeneous nucleation, the occurrence of thermal motions at molecular level may form temporarily voids that can

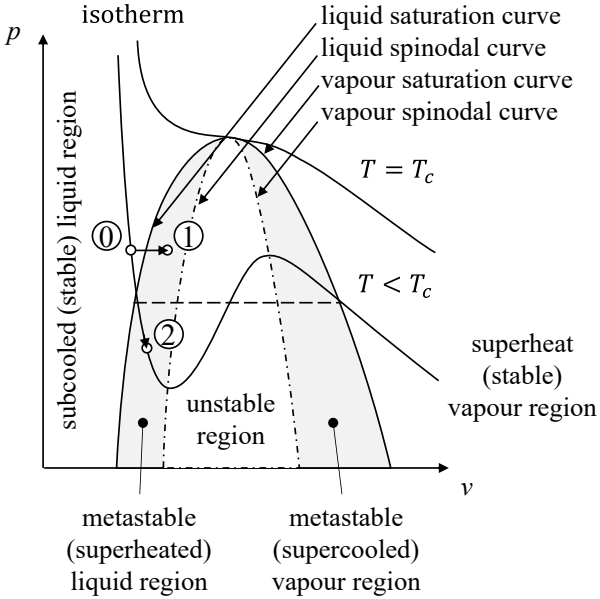

Figure 2.3: Processes of cavitation and boiling. Phase diagram adapted from Blander & Katz [69] and Brennen [63]. T_c describes the critical temperature.

result in stable and growing nucleation sites. The homogeneous nucleation takes place in the volume rather than at the container wall. In contrast, the heterogeneous nucleation refers to the nucleation at the interfaces between the liquid and the container wall or contaminants such as dissolved gases or suspended solids. In GDI, mostly heterogeneous nucleation takes place due to impurities, turbulence and wall roughness. Bubble growth and phase transition is initiated by rapid depressurisation. Detailed information on nucleation theory and bubble growth are given in Brennen [63].

Cavitation in gasoline direct injection

In the following, cavitation and its effects on spray formation in GDI are briefly outlined. Figure 2.4 schematically shows the internal nozzle flow of a

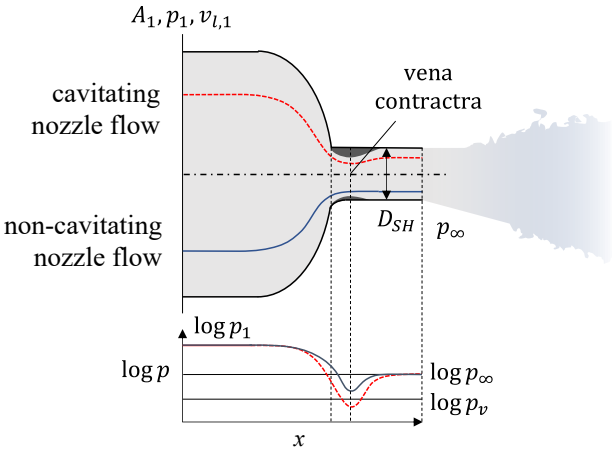

Figure 2.4: Pressure profiles along the flow filaments of a cavitating and a non-cavitating (edge-rounded) single-hole nozzle flow [59].

single-hole injector nozzle in case of a cavitating and a non-cavitating flow. Heading downstream, the nozzle geometry tapers to a sharp/rounded edge at the spray hole inlet. Pressure energy is converted into kinetic energy and partially dissipated.

In approximation, the relationship between the cross-sectional area, velocity and pressure can be described by Bernoulli's equation according to the stream filament theory of an incompressible flow [70]. Assuming negligible effect of potential energy, the pressure along the stream filament can be described by

$$p(x) = p_1 + \rho_l \frac{v_{l,1}^2}{2} \left(1 - \frac{A_1^2}{A(x)^2} \right) - \Delta p_{loss}(x), \tag{2.4}$$

where A describes the size of the cross-sectional area, x the spatial coordinate along the nozzle axis, p the local pressure and Δp_{loss} the pressure loss through energy dissipation.

In GDI, cavitating flow typically occurs at the spray-hole inlet [57, 66, 67], where the pressure drops due to cross-sectional taper and flow-induced lateral accelerations (local pressure minimum). Flow separations at the leading edge

further intensify the effect of the pressure drop. If the fluid is in tension and sufficiently stable nucleation sites are present, bubble growth is initiated [63]. The formation of cavitation bubbles at the spray hole inlet is referred to as 'sheet cavitation' [63]. To mitigate sheet cavitation, conical spray-hole designs and edge rounding are conceivable [59]. Besides sheet cavitation, a further occurrence of cavitation in GDI is due to vortex flow. The so-called 'string cavitation' [71–73] typically forms in the center of the spray hole, induced by non-uniform, eccentric inflow at the spray-hole inlet. String cavitation depends on several factors including spray-hole arrangement, nozzle design [74], spray-hole conicity [57], needle lift [75, 76], fuel properties [77] and operating conditions [78]. The effects of cavitation on spray formation are manifold. Cavitation alters the flow profile and produces additional turbulence, disturbances and radial velocities [78]. The collapse of bubbles may lead to enormous local pressures and temperatures followed by pressure waves and fluctuations. Cavitating flows usually exhibit increased jet breakup. Macroscopically, larger spray-cone angles are observed [57]. On the other hand, cavitating flows are also associated with reduced mass flows due to additional flow losses. In some cases, the mass flow is significantly reduced. In GDI, cavitating internal nozzle flow is deemed rather undesirable since it is quite challenging to robustly control the intrinsically stochastic process over a wide range of operating conditions due to its sensitivity to unsteady flow, fluctuations, manufacturing, impurities and thermodynamic conditions. In GDI, a special type of cavitation referred to as flash-boiling [74, 78] is considered an extremely important process that significantly influences spray transport and mixture preparation. When a subcooled liquid fuel (stable) becomes superheated (metastable) during rapid depressurisation from injection/system pressure to ambient pressure (see Figure 2.3, state 0 to 2; drop below saturation vapour pressure), intense nucleation, bubble growth and eventually severe rupture of the liquid takes place. The faster the process, the higher the reachable level of superheat and the more disruptive the evaporation [63]. In contrast to atomisation by mechanical means (radial velocities, turbulence, aerodynamic forces, etc.), flash-boiling atomisation exhibits markedly smaller mean droplet diameters (Sauter mean diameter (SMD)), higher homogeneity in droplet distribution, larger spray cone angles and shorter penetration lengths [28, 57, 74, 79] with the exception of certain jet-to-jet phenomena. In Figure 2.5, the influence of flash-boiling atomisation on the spray formation of a single jet is illustrated for different levels of superheat.

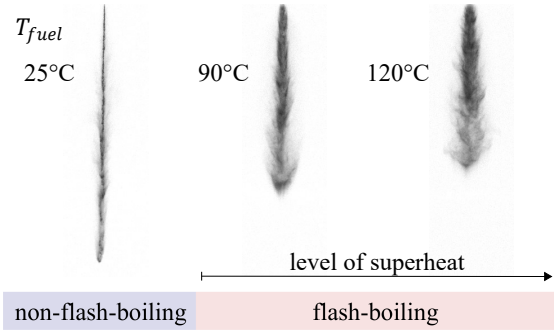

Figure 2.5: Effect of flash-boiling atomisation on the spray formation of a single jet for $T_{fuel} = 25°C$, 90°C and 120°C at $p_{inj} = 250$ bar, $p_\infty = 0.4$ bar and $T_\infty = 25°C$. Processed shadowgraphy snapshots at the same time after SOI.

In GDI, flash boiling is mainly facilitated by high fuel temperatures, low back pressures and volatile fuel components with high saturation vapour pressures. Flash-boiling allows for strong liquid atomisation even at relatively low injection pressures. During engine operation, both flash-boiling and non-flash-boiling conditions occur. This is mainly related to whether the engine is warmed up or in a cold state. Accordingly, there are high demands on the design of the injector, spray layout and targeting to provide good atomisation, spray transport and mixture preparation under all engine operating conditions.
For the characterisation of cavitating flows, the Cavitation number Ca and the Jakob number Ja are commonly used. The Cavitation number

$$Ca = \frac{p - p_v}{\frac{1}{2}\rho_l v_l^2} \tag{2.5}$$

describes the ratio between the pressure difference of local and vapour pressure to kinetic energy. The Cavitation number is well-suited for the characterisation of string and sheet cavitation, as the processes rely on local flow conditions. In terms of flash-boiling, the Jakob number [78]

$$Ja = \frac{\rho_l c_{p,l} \left(T_{fuel} - T_s\right)}{\rho_v h} = \frac{\rho_l c_{p,l} T_s \left(p_v - p_\infty\right)}{\left(\rho_v h\right)^2} \tag{2.6}$$

is generally used, where $c_{p,l}$ is the liquid heat capacity, h is the latent heat and ρ_v is the vapour density. The Jakob number describes the ratio between sensible and latent heat. A review of different cavitation regimes for different Ja, Re_l and Oh numbers is given in Bar-Kohany & Levy [78].

2.2.3 Aerodynamic forces

In primary and secondary atomisation, aerodynamic forces are significantly involved [54]. Normal and shear stresses exert forces on the liquid that may lead to disturbances, deformations and ultimately liquid disintegration. Aerodynamic forces largely depend on the relative velocity between the liquid and surrounding gas flow, their material properties, specifically density and viscosity, and the size and topology of the liquid surface. The strength of aerodynamic forces increases with larger and more fissured surface area. Accordingly, there is a close relationship between atomisation and aerodynamic forces. To some degree, both processes are mutually amplifying. The quality of internal nozzle flow and primary atomisation is preconditioning for the subsequent processes of spray-gas interaction and spray transport.

2.2.4 Spray transport

Apart from atomisation, the momentum exchange between the liquid and surrounding gas strongly affects the transport of spray and ambient gas flow [27, 61]. For instance, in Figure 2.6, the spray formation of a contracting GDI multi-hole spray is shown. During the event of spray formation, the injected momentum of the liquid induces an ambient gas flow (entrainment (1), displacement (2), recirculation (3) and wake flow (4)), which in turn influences the transport of the spray. Visually, the interaction between the spray and ambient gas flow is most evident towards the end of spray formation. As the momentum exchange progresses, both flows increasingly converge – in this case to a common vortex flow.
In the present example of spray transport, the interaction between spray and ambient gas flow also becomes apparent at the beginning of spray formation. At the start of injection (SOI), the individual spray plumes

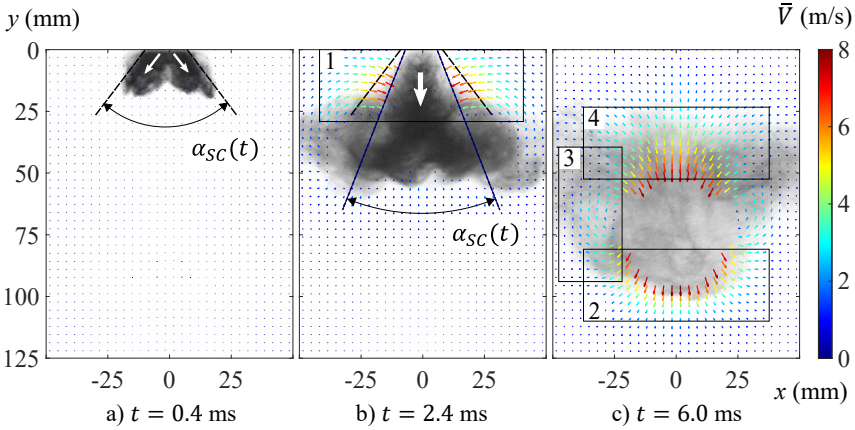

Figure 2.6: Spray transport and ambient gas flow of a contracting multi-hole spray visualised by shadowgraphs and PIV-derived velocities. $\overline{V}$ is the absolute ensemble-averaged velocity and t is the time after SOI. Operating conditions: $p_\infty = 2$ bar, $p_{inj} = 150$ bar, $T_{fuel} = 90°$C. Marked areas: entrainment flow (1), displacement flow (2), recirculation flow (3), wake flow (4).

propagate according to the directions specified by the spray-hole orientations (targeting directions). However, as the event progresses, the spray envelope in the injector near-field that is described by the spray-cone angle α_{SC} narrows and the upstream trajectories of the individual spray plumes merge into a common, centrally aligned jet. This phenomenon of contracting spray plumes is referred to as 'spray contraction'. It is considered to be caused by the interplay between spray and ambient gas flow, however, the mechanism has not been fully disclosed yet. Spray contraction and jet-to-jet interaction are subject of the present thesis' investigation.
In general, the interplay between spray and ambient gas flow is highly nonlinear, especially in terms of multi-hole sprays where jet-to-jet interaction occurs. The complex spatio-temporal interplay between spray propagation, momentum exchange and ambient gas flow largely governs the process of spray formation [27, 61] and thus defines macroscopic spray characteristics such as penetration length, spray cone angle and shape.

3 Particle Image Velocimetry

Particle Image Velocimetry (PIV) is a non-intrusive, indirect, optical measurement technique that allows for the evaluation of velocity fields by means of image processing. The principle of PIV is based on the seeding of flows with tracer particles and the subsequent tracking of their motion over time. A prerequisite for PIV is an adequate tracking behaviour of the tracers used in relation to the flow under investigation. Depending on the flow and application, various tracers have been used in research and engineering, including oil droplets, helium-filled bubbles [80, 81], smoke [82] up to snowflakes [83], seats and bacteria [84] for specific large-scale and micro applications.
In the field of PIV, several techniques were developed to provide and optimise velocimetry for different applications (Micro-PIV [85], combustion engine [86, 87], wind tunnel [88]), measurement conditions/restraints (optical accessibility, two-phase flow) and expenses of measurement technology (number/type of cameras and light sources). Various principles, including the use of multiple camera views, light properties and diffraction-based depth coding are utilised. The techniques are commonly classified by the number of measured dimensions (D) and velocity components (C).
PIV ranges from conventional planar PIV (2D2C) and stereoscopic PIV (stereo-PIV) [89] (2D3C) to quasi-volumetric/multi-plane PIV (2.5D3C) (Dual-Plane Stereo PIV (DSPIV) [90], multi-plane stereoscopic PIV (XPIV) [91]) up to volumetric PIV (3D3C) (3D Particle Tracking Velocimetry (3D-PTV) [92], Tomographic PIV (Tomo-PIV) [49], Astigmatism Particle Tracking Velocimetry (APTV) [93, 94], Defocusing PIV [95], Holographic PIV (HPIV) [96]) and time-resolved Particle Tracking Velocimetry (4D-PTV) (Shake-The-Box (STB) [97]). Detailed information about the velocimetry techniques is reviewed in Discetti & Coletti [98].
In the framework of the present thesis, stereo-PIV is used for the measurement of spray-induced flow. In the following sections, the fundamentals of stereo-PIV, particle motion and tracking behaviour, particle imaging, PIV evaluation (displacement analysis) and the specifics for the measurement of spray-induced

flow are described. Further information about the fundamentals of PIV is given in Raffel *et al.* [10]. A nomenclature consistent with the literature [10] is used.

3.1 Stereo-PIV

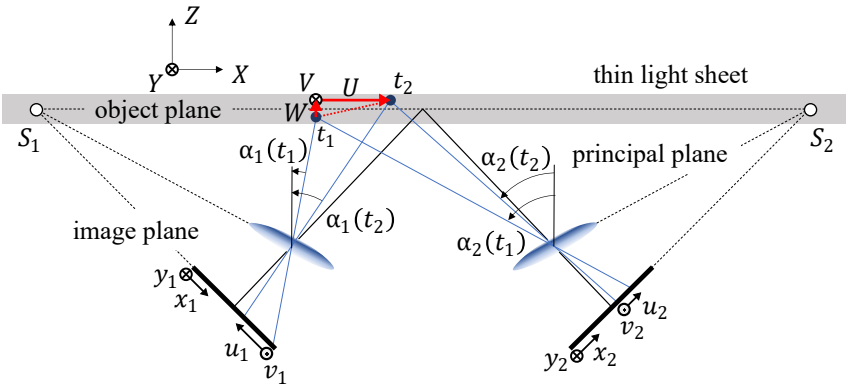

Figure 3.1: Stereoscopic setup [10].

In contrast to conventional PIV, stereo-PIV allows for the reconstruction of the out-of-plane velocity component W by using two projections of the in-plane displacements. In Figure 3.1, a stereoscopic PIV setup including a thin light sheet, two imaging systems and an exemplary particle displacement is shown. To ensure a continuous depth of field (DOF) over the entire field of view (FOV), the Scheimpflug criterion [99] is applied by having the lens, image and object planes of the cameras intersect in common lines S_1 and S_2. For such a setup, the object plane velocity components are given by [100]

$$U = \frac{U_1 \tan\alpha_2 + U_2 \tan\alpha_1}{\tan\alpha_1 + \tan\alpha_2} \tag{3.1}$$

$$V = \frac{V_1 \tan\beta_2 + V_2 \tan\beta_1}{\tan\beta_1 + \tan\beta_2} \tag{3.2}$$

$$W = \frac{U_1 + U_2}{\tan\alpha_1 + \tan\alpha_2} = \frac{V_1 + V_2}{\tan\beta_1 + \tan\beta_2}, \tag{3.3}$$

where $U_i = u_i/M_i$ and $V_i = v_i/M_i$ are the projected object plane velocities of the respective cameras denoted by $i = 1, 2$, u_i and v_i are the corresponding image plane velocities, M_i is the optical magnification, t_j with $j = 1, 2$ are the acquisition times, and α_i and β_i are the enclosed angles between the Z-axis and the particle's light ray through the intersection of the optical axis and the principal plane projected onto the XZ- and YZ-planes, respectively. As the viewing distance is typically much greater than the particle displacements, the angular changes of α_i and β_i are negligible. It applies $\alpha_i(t_j) \approx \alpha_i$ and $\beta_i(t_j) \approx \beta_i$.
Due to the inclined camera perspectives, the optical magnifications M_i are not constant across the FOV. For this purpose, a mapping between the image and object space as well as certain information about the viewing directions of the cameras are required. Typically, a calibration of the stereo-PIV setup is done based on the imaging of a multi-level target plate at the level of the measurement plane. The target plate consists of a known pattern (e.g. dots, crosses) that allows for the formulation of mapping functions and the reconstruction of camera viewing directions through image processing. Another approach often used to refine a base calibration is the self-calibration procedure [101]. In this procedure, image recordings from the two cameras at the same time of acquisition t_j are used to identify and correct possible disparities through image processing, usually by image cross-correlation (see Section 3.4). The self-calibration procedure enables the correction of various sources of error, including a misalignment of the calibration target relative to the light sheet (e.g. out-of-plane position, rotation), which is usually present to some degree.

3.2 Tracking characteristics

The motion of a spherical particle in an unsteady flow can be described mathematically by the Basset-Boussinesq-Oseen (BBO) equation [102, 103].

The BBO equation describes the Lagrangian acceleration of a particle as the sum of viscosity, gravity, buoyancy, virtual mass and Basset forces acting on the particle. It is given by

$$\frac{\pi d_p^3}{6}\rho_p\frac{\mathrm{d}u_p}{\mathrm{d}t} = -3\pi\mu_f d_p\left(u_p-u_f\right)+\frac{\pi d_p^3}{6}\rho_f\frac{\mathrm{d}u_f}{\mathrm{d}t} - \frac{1}{2}\frac{\pi d_p^3}{6}\rho_f\frac{\mathrm{d}\left(u_p-u_f\right)}{\mathrm{d}t} - \frac{3}{2}d_p^2\sqrt{\pi\mu_f\rho_f}\int_{t_0}^{t}\frac{\mathrm{d}\left(u_p-u_f\right)}{\mathrm{d}\xi}\frac{d\xi}{(t-\xi)^{1/2}}, \quad (3.4)$$

where d_p, ρ_p and u_p are the particle diameter, density and velocity, while ρ_f, μ_f and u_f are the density, dynamic viscosity and velocity of the surrounding fluid. ξ denotes a time variable used for the computation of the Basset forces.

The assumption of a spherical particle applies to small and monodisperse particles [104]. For high density ratios ρ_p/ρ_f, as is usually the case with gas flows and conventional tracer media, the Equation 3.4 simplifies to

$$\frac{du_p}{dt} = C\left(u_p-u_f\right) \quad (3.5)$$

with

$$C = \frac{3}{4}C_D Re_p\frac{\mu_f}{\rho_p d_p^2} \quad (3.6)$$

and

$$Re_p = \frac{\rho_f\left(u_p-u_f\right)d_p}{\mu_f}, \quad (3.7)$$

where C is the characteristic frequency of the particle motion, C_D is the drag coefficient and Re_p is the particle Reynolds number. For particle Reynolds numbers below one ($Re_p \leq 1$), Stokes' law of resistance with $C_D = 24/Re_p$ applies

$$C = \frac{18\mu_f}{\rho_p d_p^2}. \quad (3.8)$$

The tracking capability of a particle is estimated by its frequency response. According to Melling [104], the frequency response of a particle in a turbulent flow for a high density ratio is given by

$$\frac{\overline{u_p^2}}{\overline{u_f^2}} = \left(1+\frac{\omega_c}{C}\right)^{-1}, \quad (3.9)$$

where $\overline{u_p^2}$ and $\overline{u_f^2}$ are the kinetic energies of the particle and fluid fluctuations and ω_c denotes the highest frequency. In gas flows the typical particle diameter for adequate tracking behaviour is about 1 μm and smaller [104].

3.3 Particle imaging

According to the Fraunhofer approximation, the point spread function (PSF) of an aberration-free imaging system with circular aperture describes a circular pattern with successive intensity maxima and minima as shown in Figure 3.2a. In focus, the resulting intensity distribution corresponds to the square of the first order Bessel function (Airy function) with a dominant central intensity peak. With increasing out-of-focus distance, the diffraction pattern changes (see Figure 3.2b), whereby the intensity distribution shifts in favour of the outer rings. The particle image is given by the convolution of the point spread function with the geometric image of the particle [10]. Olsen & Adrian [105] proposed a formulation of the imaged particle diameter considering the contributions of geometric optics and diffraction. The out-of-focus effect is approximated by the geometric spread of the particle image. The contribution of diffraction is characterised by the central maximum of the Airy function. The change of the point spread function due to defocusing is neglected. The estimate of the imaged particle diameter according to Olsen & Adrian [105] is given by

$$d_e = \left(M^2 d_p^2 + 5.95 f_\#^2 \left(M+1\right)^2 \lambda^2 + \frac{M^2 z^2 D_a^2}{\left(s_o + z\right)^2} \right)^{1/2}, \tag{3.10}$$

where M is the optical magnification, $f_\# = f/D_a$ is the f-number, f is the focal length, D_a is the aperture diameter, λ is the wavelength of light, z is the out-of-focus coordinate and s_o is the object distance.
The depth of field (DOF) of an optical system is described by the distance at which the circle of confusion or blurring of a point source is within the range of a predefined criterion. In PIV, a suitable criterion for the DOF is the range in which the circle of confusion of a point source is imaged with a size that corresponds to a particle image size favourable

(a) Lateral section (focal plane) **(b)** Axial section

Figure 3.2: Point spread function (PSF) of a circular aperture.

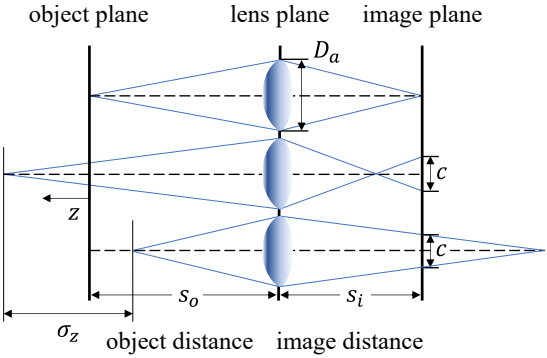

Figure 3.3: Schematic illustration of the depth of field σ_z, where s_i is the image distance. Adapted from Raffel *et al.* [10].

for PIV evaluation, for instance ∼2.2 px in case of double-exposure image cross-correlation [106]. Figure 3.3 illustrates the relationship between the out-of-focus position and the circle of confusion c. The depth of field is given by

$$\sigma_z = \frac{2f_{\#}c\,(M+1)}{M^2 + \left(\frac{f_{\#}c}{f}\right)^2} \approx \frac{2f_{\#}c\,(M+1)}{M^2}\,[10]. \tag{3.11}$$

3.4 PIV evaluation via image cross-correlation

To determine the image-plane displacement fields in Stereo-PIV (see Section 3.1), various image processing methods are used to extract desired information about the motion of particles or features between two successive PIV recordings. Besides the tracking of individual particles, which is usually applied for measurements with sparse particle image densities [92, 94, 95] or extensive measurements with time-resolved data [97], a widely-used approach for deriving velocity information is the method of image cross-correlation [10], which is used to quantify the correlation or match of an image pair as a function of relative displacement.
In PIV, the image cross-correlation is employed to analyse the displacement of particle image ensembles. To obtain evaluation of a displacement field with multiple vectors and a given spatial resolution, the method of image cross-correlation is performed on multiple subsets of image pairs referred to as interrogation areas (IAs) or interrogation windows (IWs), as illustrated in Figure 3.4. For each pair of interrogation windows, a displacement vector is quantified by comparing the intensity distributions between both recordings for different relative shifts x and y as shown in Figure 3.5. A mathematical formulation [10] of the cross-correlation function for a pair of images of equal size with rectangular shape and discrete pixel values can be described by

$$R_I(x,y) = \frac{1}{A_{IW}(x,y)} \sum_{i=max(1,1-x)}^{min(N_x,N_x-x)} \sum_{j=max(1,1-y)}^{min(N_y,N_y-y)} I_1(i,j)\, I_2(i+x, j+y) \tag{3.12}$$

with

$$A_{IW}(x,y) = (N_x - |x|)\,(N_y - |y|)\,, \tag{3.13}$$

where I_1 and I_2 are the intensity distributions of the PIV recordings, $N_x \times N_y$ is the pixel resolution of the interrogation windows and A_{IW} is the overlapping area of the interrogation windows. For each relative shift, the pixel-wise product of the intensity distributions are summed up and normalised within the area of mutual overlap. The shift associated with the highest correlation value is used as estimate for the actual displacement of the particle ensemble within the interrogation window, as illustrated in

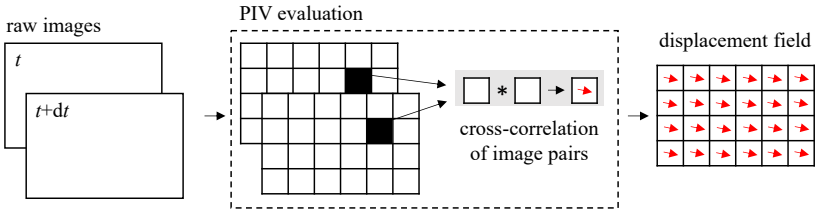

Figure 3.4: Flow chart of PIV evaluation using image cross-correlation.

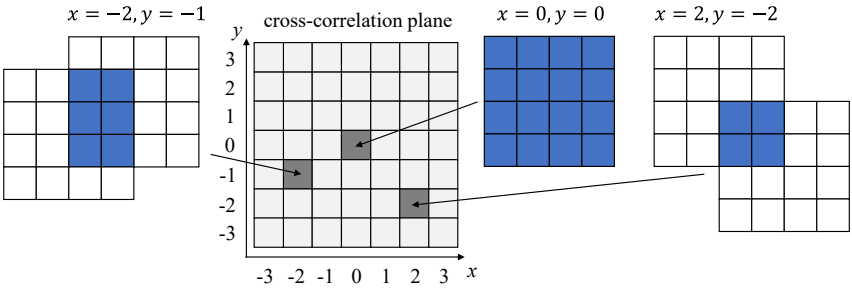

Figure 3.5: Schematic illustration of an image cross-correlation process for different relative pixel shifts. Adapted from Raffel *et al.* [10].

Figure 3.6. The result of image cross-correlation yields integer values. To gain subpixel accuracy, further processing is required which is outlined in the following Subsection (see 3.4.1).

The maximum relative shift in image cross-correlation for two equally sized interrogation windows is given by $[\pm N_x - 1, \pm N_y - 1]$ [10]. However, since the signal strength, and thus the accuracy, decreases for larger relative shifts as the number of possible particle matches becomes smaller, a widely used guideline is to limit the maximum relative shift to one-fourth of the interrogation window size $[\pm N_x/4, \pm N_y/4]$ [106], which is also known as the 'one-quarter rule' in PIV. In general, the maximum recoverable particle image displacement is not limited by the maximum usable relative shift in image cross-correlation. Some techniques such as grid refinement or window offset (see Section 3.4.1) allow for the evaluation of larger particle image displacements.

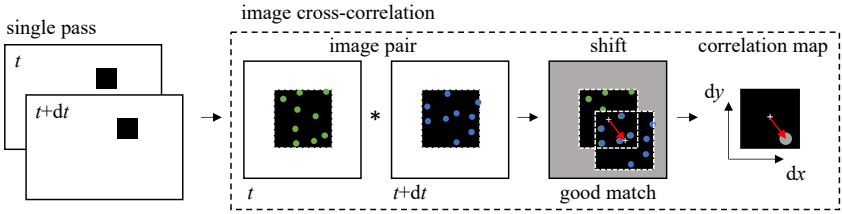

Figure 3.6: Illustration of a single pass image cross-correlation.

The choice of the interrogation window size relies on multiple aspects that affect the performance and accuracy of displacement analysis including particle image density, particle image size, signal-to-noise level, out-of-plane particle loss of pairs (particle that is not imaged at both recordings due to out-of-plane motion) etc. Common interrogation window sizes used in PIV evaluation are 16×16 px and 32×32 px. However, the interrogation window size or shape can be chosen freely, as there are no specific constraints such as a necessity for a square/rectangular shape or an even/quadratic number of pixels.

3.4.1 Advanced digital techniques

To improve the performance of PIV evaluation and to extend its capabilities, several different processing techniques were introduced. In the following, a selection of the most common concepts of advanced digital PIV processing are briefly outlined. For more detailed information about PIV evaluation and associated post-processing techniques, the reader is referred to the corresponding articles and literature such as Raffel *et al.* [10].

Subpixel accuracy

One of the most important metrics in digital PIV evaluation is the minimum recoverable pixel shift as it largely determines the attainable accuracy and dynamic range of velocity measurement. Given the discretised input data, the standard computation of the image cross-correlation function (Equation

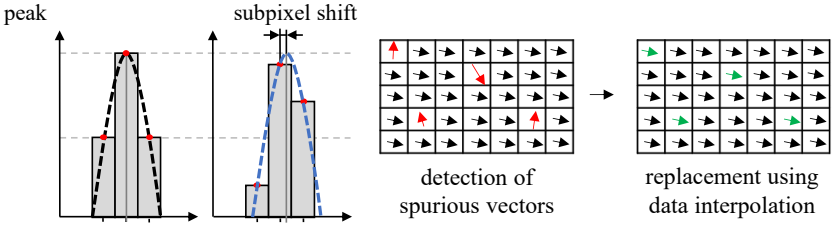

(a) Subpixel accuracy **(b)** Outlier detection and replacement

Figure 3.7: Subpixel accuracy via three-point estimator [10] (a) and data validation by means of outlier detection and data interpolation [10] (b).

3.12) yields integer shifts with no subpixel accuracy. To overcome this limitation, several methods have been introduced that use the resultant cross-correlation data to estimate the position of the correlation peak with subpixel accuracy. A common strategy to achieve subpixel accuracy is to fit the correlation data to a specific function that mimics the cross-correlation function of particle images. Since the cross-correlation function of properly focused particle images is characterised by an airy function (see Section 3.3), a widely used method for fitting the correlation data is a three-point estimator with a Gaussian intensity profile, as illustrated in Figure 3.7a. Depending on the actual position of the correlation peak – whether the shift has an integer or a non-integer pixel value – the correlation data of the peak and its adjacent values have an inclined intensity profile or not. By the use of such estimation strategies, a subpixel accuracy of about 1/10th to 1/20th of a pixel (for 32×32 px IA size, 8-bit image depth) can be reached according to simulation data [10].

Outlier detection

After PIV evaluation, a certain number of displacement vectors are usually found as visibly spurious. In such cases, the proper detection of the correct correlation peak of matching particle images is typically disturbed by noise (pixel noise, backlight, reflections) or other negative aspects such as insufficient/inhomogeneous particle seeding, imperfect illumination (laser

pulse alignment, intensity profiles), out-of-plane motion, in-plane/out-of-plane velocity gradients or low signal intensity (low scattered light intensity, insufficient light-source intensity, short exposure time) [107].
Beyond the general desire for good data quality, many post-processing techniques such as the calculation of derivatives, the application of advanced PIV evaluation methods or the evaluation of pressure rely on acceptable data quality. Therefore, to ensure the validity of the data and to prevent the corruption of good data by error propagation, the detection and replacement of spurious vectors or outliers (Figure 3.7b) is an essential task in PIV processing.
For data validation, a variety of different approaches were introduced [10]. This includes methods that range from the utilisation of fluid mechanical properties (continuity, flow structures), to the use of redundant information (time-resolved data, multiple views), to indicative criteria from the cross-correlation function (minimal correlation value, ratio between first and second highest correlation peaks, signal-to-noise ratio), up to the comparison of adjacent displacement vectors.
A frequently used method for data validation is the 'normalized median filter' [108]. The principle of the normalized median filter relies on the statistical analysis of neighbouring velocity vectors. If the magnitude and/or direction of the velocity vector or its components exceeds a specific criterion as illustrated in Figure 3.7a, the vector under investigation is considered as likely invalid. Thanks to its simplicity, robustness and certain degree of generalisation, the normalized median filter is an effective method for most of the PIV applications. In PIV evaluation, typically multiple different data validation techniques are used in conjunction to maximise data quality.

Window offset

A valuable method to enhance the signal-to-noise ratio in PIV evaluation and thus to decrease measurement uncertainty is to use an iterative processing scheme consisting of multiple passes of image cross-correlation that considers a window offset of the image pairs based on the estimation of previous passes [109]. By offsetting the interrogation window according to the mean displacement as shown in Figure 3.8, the proportion of matching to non-matching particle pairs increases which in turn enhances the correlation peak and signal-to-noise ratio. According to simulations with synthetic

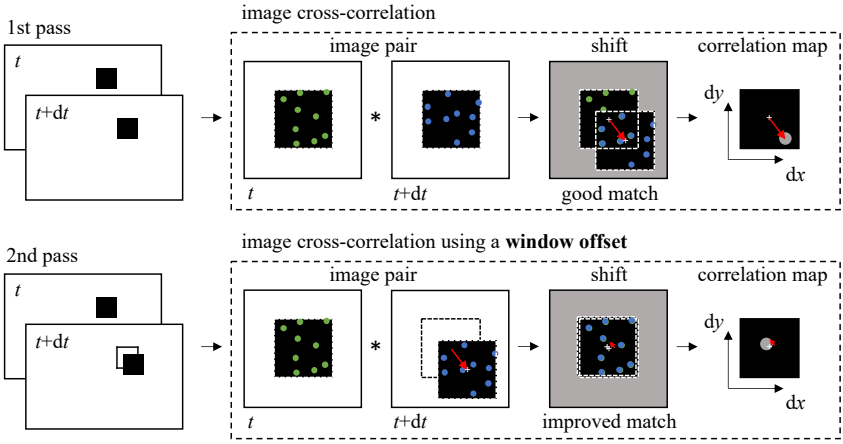

Figure 3.8: Window offset.

data, the uncertainty of image cross-correlation decreases considerably with smaller particle image displacements [109]. The increase in signal-to-noise ratio provides less uncertainty, higher robustness – especially for noise-susceptible measurements such as PIV of spray-induced flow – and overall a more accurate estimation of displacement. The improved accuracy of image cross-correlation also implicitly allows for the use of smaller interrogation areas and thus for higher spatial resolutions. The increased computational expense due to the use of multiple passes can be substantially lowered by utilising preceding estimates to limit the area of cross-correlation for subsequent passes. The window offset method can be implemented such that a central differencing scheme with a second-order accuracy in time is achieved by using a symmetric offset of both particle images [110], as illustrated in Figure 3.8, rather than a simple offset of one of the particle images which corresponds to a forward or backward differencing scheme.

Window deformation

Since most practical flows typically exhibit velocity gradients and thus different particle displacements/trajectories within an interrogation win-

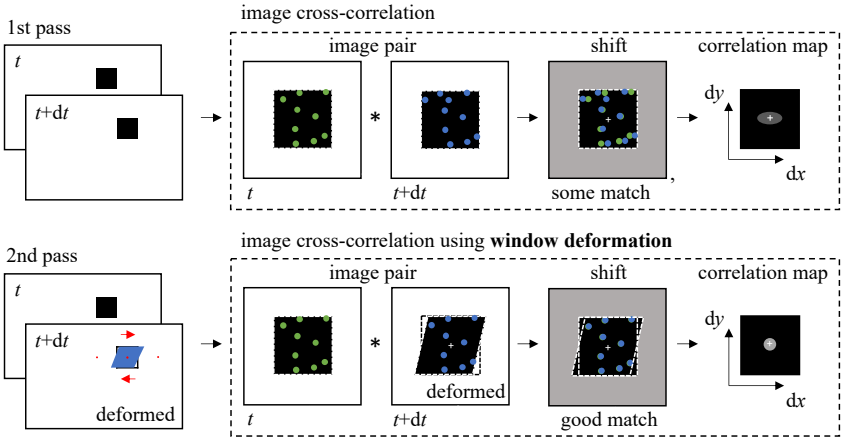

Figure 3.9: Window deformation.

dow, the prevailing assumption of approximately uniform particle motion in image cross-correlation is often violated. If no additional precautions are taken in such cases, the uncertainty of the measurement may increase significantly as a result of a lower signal-to-noise ratio [10]. In the presence of a substantial spread in particle displacements, the peak of the cross-correlation function tends to become wider and smaller, while the level of noise increases. Furthermore, since the particle velocities span a range of different particle displacements, the cross-correlation may yield multiple correlation peaks instead of a unique particle displacement, greatly increasing the risk of a spurious vector as a result of image cross-correlation. One possible way to reduce the undesired effect of velocity gradients would be to reduce the size of the interrogation windows in PIV evaluation [10]. However, despite its effectiveness, there are usually limits to this measure at some point as no further reduction of the interrogation window size is practical.

A viable and widely used strategy to compensate for the negative influence of velocity gradients in image cross-correlation is to deform the interrogation windows or raw images [111] according to an initial estimate of the velocity field, usually derived by a prior image cross-correlation pass, as shown in Figure 3.9. By the deformation of the interrogation windows

or raw images, the proportion of particle image matches increases, which in turn leads to an increase in correlation and signal-to-noise ratio, and furthermore to a narrowing of the correlation peak and an increase in accuracy. In analogy to window offset, the increased signal-to-noise ratio in image cross-correlation justifies the use of higher spatial resolutions when using window deformation. The method of window deformation can be implemented as an iterative processing scheme that runs until a certain convergence criteria is reached. It shall be noted, that the use of iterative window deformation is subject to a selective amplification of wavelengths smaller than the interrogation windows, which however can be mitigated by low-pass filtering of the intermediate results as shown by Schrijer and Scarano [112].

Grid refinement

To extend the dynamic range and spatial resolution of PIV evaluation which is limited by the size of the interrogation windows and corresponding maximum shift (one-quarter rule [113], see Section 3.4), a hierarchical approach [100, 114] in which the interrogation grid and window sizes are successively refined over multiple passes (see Figure 3.10) is commonly adopted. By starting on a coarse grid with relatively large interrogation window sizes, and thus higher applicable shifts in image cross-correlation, the approach is able to account for larger displacements. For successive interrogation passes with gradually refined interrogation grids and window sizes, the resultant displacements of preceding passes are used as initial estimates for window-offset passes to ensure proper correlation of image pairs, even in the case of exceeding displacements relative to the reduced interrogation window sizes. The refinement of the interrogation grid and window sizes is typically performed until a certain criterion is reached that indicates a significant increase in uncertainty of PIV evaluation, e.g. when the correlation value or signal-to-noise ratio falls below a certain threshold. According to simulations, the uncertainty increases rapidly when the number of matching particle images is less than four [10]. As the grid refinement approach allows for smaller interrogation window sizes than displacements, higher spatial resolutions can be achieved. In accordance to other multiple pass interrogation approaches, the validation of data between successive passes is pivotal to ensure convergence.

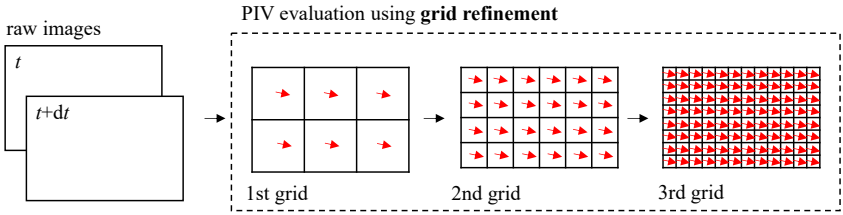

Figure 3.10: Grid refinement.

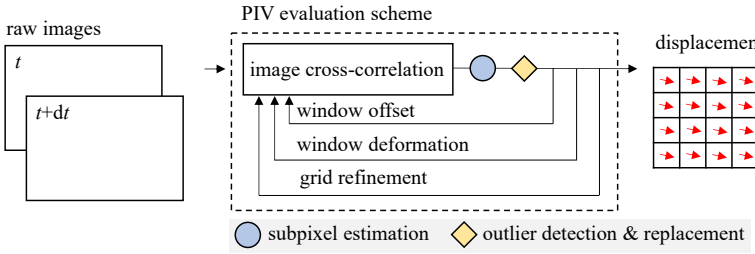

Figure 3.11: Multiple pass PIV evaluation scheme with grid refinement, window deformation and window offset.

3.4.2 PIV processing scheme

The use of PIV processing techniques and the definition of its parameters largely depends on the quality of the image recordings, the experimental setup and the flow under investigation. Beyond standard image cross-correlation, many PIV processing techniques are viable methods to increase the performance of PIV evaluation by enhancing its accuracy, robustness and spatial resolution as pointed out before. In the present thesis, a combination of the aforementioned processing techniques is used for the evaluation of PIV recordings of spray-induced flow. The PIV processing scheme consists of a multiple pass interrogation scheme with grid refinement [100, 114], window deformation [111] and window offset [109], as shown in Figure 3.11. For subpixel accuracy, a Gaussian three-point estimator [10] is used, while spurious vectors are detected and replaced by a normalised median filter [108] and linear interpolation.

3.5 The application of stereo-PIV to spray-induced flow

Due to the small time and length scales involved, the application of PIV to the spray-induced flow of GDI sprays is a challenging task that requires the use of sophisticated measurement technology and well-designed experiments. Therefore, to provide adequate particle imaging, a high-speed system with a powerful light source, usually a laser-light source, and a short exposure time is typically needed. Beyond the requirements on the measurement technology and experimentation, the velocimetry of spray-induced flow is furthermore subject to some specific challenges due to the presence of a finely atomised fluid. As the intensity of Mie-scattered light is proportional to $\sim d_p^2$, the recorded signal from the necessarily small tracer particles (see Section 3.2) is significantly lower than the signal of the larger spray droplets and ligaments as shown in Figure 3.12a. For dilute sprays, the use of intensity-based filters might be applicable [18], however, for dense sprays, the spread of the scattered light intensity exceeds the dynamic range of today's camera sensors, so that no sufficient signal-to-noise ratio is available for PIV evaluation.
A viable approach to improve the signal-to-noise ratio and to enable PIV evaluation for dense sprays is the use of fluorescent tracer particles and

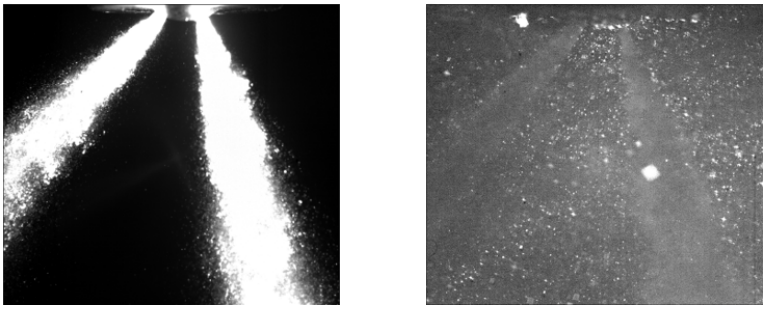

(a) No filtering: Mie signal **(b)** With filtering: LIF signal

Figure 3.12: The influence of using fluorescent tracer particles and optical filtering on the signal-to-noise ratio in PIV of spray-induced flow.

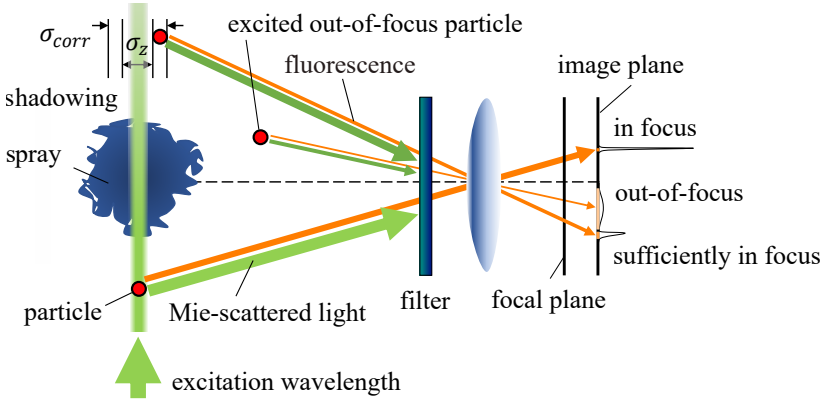

Figure 3.13: Illustration of the used concepts of optical filtering and depth of correlation.

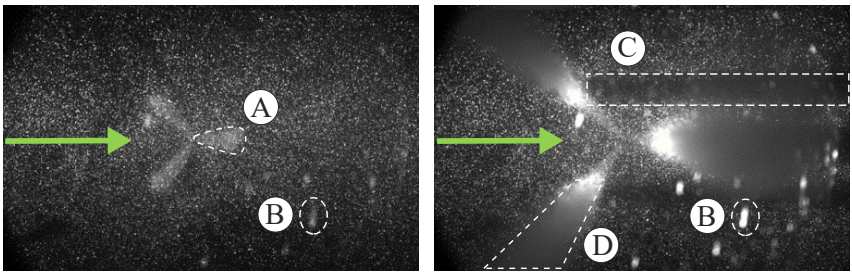

(a) No light-sheet intersection **(b)** Light-sheet intersection with spray

Figure 3.14: Negative aspects on the signal-to-noise ratio of PIV recordings of spray-induced flow: background noise due to multi-scattered light from the spray (A) or surfaces and deposits (B); light-sheet attenuation (C) through scattering at the spray; disturbance of the tracer signal (D) due to multi-scattering at the spray and associated out-of-focus blurring. The direction of the light-sheet is indicated by a green arrow.

optical filtering. As shown in Figure 3.13, the principle of the method relies on the absorption of the Mie-scattered light (predominantly from the spray) at a long-pass filter, while the emitted fluorescence signal from the tracer particles is transmitted to the camera sensor. Due to the optical filtering and phase separation, the signal from the tracer particles becomes clearly visible as shown in Figure 3.12b. The prominent scattered light from the spray is largely absorbed. Only a slight impression of the spray is still noticeable, which is mainly due to the absence of tracer particles and the excitation of out-of-plane particles caused by the intense light scattering at the spray.

Despite the gain from optical filtering, it should be noted that the use of fluorescence is associated with a significantly lower signal level compared to the Mie scattered light signal. In some cases, e.g. in the case of light-sheet attenuation, multi-scattering, blurring or strong background noise (see Figure 3.14), the signal level might be too low for PIV evaluation, however, for most of the configurations and measurement conditions, the achievable signal-to-noise ratio is sufficient.

Another aspect of spray-induced flow measurement is the specific limitation of the measurement domain. In conventional planar PIV, the measurement domain is usually constrained by the thickness of the light sheet. This does not apply to spray-induced flow measurements with intense light scattering and beam expansion, as otherwise illuminated out-of-plane tracer particles contribute unintentionally to the PIV evaluation. In such a case, the measurement domain needs to be confined by the depth of field as used in Micro-PIV [10]. According to Meinhart *et al.* [115], the measurement domain is limited to about twice the depth of field (depth of correlation $\sigma_{corr} \approx 2\sigma_z$), since the contribution of particles in image cross-correlation becomes negligible with further defocusing due to strong blurring and loss in peak intensity. In Figure 3.13, the concept of depth of correlation is schematically shown.

4 Pressure from PIV by means of URANS and ensemble averaging

In this chapter, the methodology of velocimetry-based pressure evaluation using URANS and ensemble averaging [50] is presented. The method was introduced in the context of the present work to enable pressure evaluation of spray-induced flow by means of planar stereo-PIV. In contrast to conventional pressure evaluation, which requires the use of volumetric velocimetry to fully characterise the governing equations, the statistical approach overcomes the limitation of out-of-plane gradient determination by allowing the description/construction of ensemble-averaged, quasi-volumetric velocity fields based on multiple spatially and temporally independent measurements. As an extension of the existing Reynold-averaged approach [43, 44, 116], the method allows for the treatment of unsteady flows by including local acceleration. The following sections are based on the publication of Kling *et al.* [50]. A nomenclature with index notation and Einstein summation convention is used, as is common in classical continuum mechanics [70].

4.1 Fundamentals

"The pressure evaluation by means of Particle Image Velocimetry relies on the inverse solution of the Navier-Stokes equations. By invoking the Navier-Stokes equations, the pressure computation is obtained by spatial integration of the pressure gradient. In general, the pressure gradient is related to spatio-temporal information about the velocity field, density, viscosity and body forces. By the implementation of supplementary relations for density and viscosity, an integral description of the pressure

gradient is given in terms of velocity field information." [50]
In pressure evaluation of spray-induced flow, the computation is usually confined to the spray-surrounding airflow as no accurate velocimetry data is available in the region of optically dense spray (hidden flow regime). For modelling the ambient gas flow, the following assumptions are made within the scope of the present thesis' investigations. "The flow is considered as compressible, while density fluctuations are neglected due to the presence of low Mach-numbers and the minor effect in terms of pressure evaluation [116]. Mass and heat transfer are assumed to be minimal due to the presence of low and uniform temperatures. Consequently, a constant gas composition [...] is expected [117]. Viscous effects are considered to be Newtonian and gravity is taken into account. The corresponding URANS equations are given by

$$\begin{aligned}\rho\frac{\mathrm{D}\overline{u}_i}{\mathrm{D}t} &= \rho\left(\frac{\partial\overline{u}_i}{\partial t}+\overline{u}_j\frac{\partial\overline{u}_i}{\partial x_j}\right)\\ &= -\frac{\partial\overline{p}}{\partial x_i}+\frac{\partial}{\partial x_j}\left[\mu\left(\frac{\partial\overline{u}_i}{\partial x_j}+\frac{\partial\overline{u}_j}{\partial x_i}\right)\right]-\frac{2}{3}\frac{\partial}{\partial x_i}\left(\mu\frac{\partial\overline{u}_j}{\partial x_j}\right)-\frac{\partial}{\partial x_j}\left(\rho\overline{u_i'u_j'}\right)+\rho\overline{f}_i,\end{aligned} \tag{4.1}$$

where $\overline{p}$ is the ensemble-averaged pressure, $\overline{u}_i$ are the ensemble-averaged velocity components, u_i' are the velocity fluctuations, ρ is the density, μ is the dynamic viscosity, $\overline{f}_i$ describes the gravitational force and $\rho\overline{u_i'u_j'}$ are the Reynolds stresses.
In the case of spray-induced flow measurements, the ensemble average describes the mean behaviour of several injection events. Due to its stochastic nature provoked by instabilities, turbulence, cavitation and other physically complex phenomena, the experiments are naturally not perfectly repeatable. Therefore, the ensemble average contains additional contributions of injection stochastics." [50] In the present work, the ensemble average and fluctuation of an arbitrary quantity θ is described by

$$\overline{\theta}(x,t) = \frac{1}{N}\sum_{n=1}^{N}\theta_n(x,t), \tag{4.2}$$

$$\theta_n'(x,t) = \theta_n(x,t)-\overline{\theta}(x,t), \tag{4.3}$$

where the index n denotes the experiment and N is the number of experiments.

"In the following discussion, the full URANS equations are considered in order to guarantee completeness. Consequently, the mean pressure gradient is described by

$$\begin{aligned}\frac{\partial \overline{p}}{\partial x_i} = &-\rho\frac{\mathrm{D}\overline{u}_i}{\mathrm{D}t} + \frac{\partial}{\partial x_j}\left[\mu\left(\frac{\partial \overline{u}_i}{\partial x_j} + \frac{\partial \overline{u}j}{\partial x_i}\right)\right] \\ &- \frac{2}{3}\frac{\partial}{\partial x_i}\left(\mu\frac{\partial \overline{u}_j}{\partial x_j}\right) - \frac{\partial}{\partial x_j}\left(\rho\overline{u_i' u_j'}\right) + \rho\overline{f}_i." \text{ [50]}\end{aligned} \tag{4.4}$$

4.1.1 Pressure gradient integration

"In the past, two different integration-strategies have been employed. One of the strategies is a spatial marching scheme [118], whose procedure describes the direct integration of the pressure gradient along a specified marching route in the domain of interest." [50] The other strategy is based on "[...] the divergence of the momentum equation and its subsequent solving. In the present work, the pressure computation is performed by utilising the divergence equation according to

$$\begin{aligned}\frac{\partial^2 \overline{p}}{\partial x_i \partial x_i} = &-\frac{\partial}{\partial x_i}\left[\rho\left(\frac{\partial \overline{u}_i}{\partial t} + \overline{u}_j\frac{\partial \overline{u}_i}{\partial x_j}\right)\right] + \frac{\partial^2}{\partial x_i \partial x_j}\left[\mu\left(\frac{\partial \overline{u}_i}{\partial x_j} + \frac{\partial \overline{u}_j}{\partial x_i}\right)\right] \\ &- \frac{2}{3}\frac{\partial^2}{\partial x_i \partial x_i}\left(\mu\frac{\partial \overline{u}_j}{\partial x_j}\right) - \frac{\partial^2\left(\rho\overline{u_i' u_j'}\right)}{\partial x_i \partial x_j} + \frac{\left(\rho\overline{f}_i\right)}{\overline{x}_i}." \text{ [50]}\end{aligned} \tag{4.5}$$

In the case of a two-dimensional problem, such as a spray with a symmetrical spray layout, the Equation 4.5 simplifies to

$$\begin{aligned}\frac{\partial^2 \overline{p}}{\partial x_1^2} + \frac{\partial^2 \overline{p}}{\partial x_2^2} = &-\frac{\partial}{\partial x_1}\left[\rho\left(\frac{\partial \overline{u}_1}{\partial t} + \overline{u}_j\frac{\partial \overline{u}_1}{\partial x_j}\right)\right] - \frac{\partial}{\partial x_2}\left[\rho\left(\frac{\partial \overline{u}_2}{\partial t} + \overline{u}_j\frac{\partial \overline{u}_2}{\partial x_j}\right)\right] \\ &+ \frac{\partial^2}{\partial x_1 \partial x_j}\left[\mu\left(\frac{\partial \overline{u}_1}{\partial x_j} + \frac{\partial \overline{u}_j}{\partial x_1}\right)\right] + \frac{\partial^2}{\partial x_2 \partial x_j}\left[\mu\left(\frac{\partial \overline{u}_2}{\partial x_j} + \frac{\partial \overline{u}_j}{\partial x_2}\right)\right] \\ &- \frac{2}{3}\left[\frac{\partial^2}{\partial x_1^2}\left(\mu\frac{\partial \overline{u}_j}{\partial x_j}\right) + \frac{\partial^2}{\partial x_2^2}\left(\mu\frac{\partial \overline{u}_j}{\partial x_j}\right)\right] \\ &- \frac{\partial^2\left(\rho\overline{u_1' u_j'}\right)}{\partial x_1 \partial x_j} - \frac{\partial^2\left(\rho\overline{u_2' u_j'}\right)}{\partial x_2 \partial x_j} + \frac{\partial\left(\rho\overline{f}_1\right)}{\partial x_1} + \frac{\partial\left(\rho\overline{f}_2\right)}{\partial x_2}.\end{aligned} \tag{4.6}$$

"The in-plane pressure determination requires reduced computational and measurement expense in comparison to the 3D formulation, which in turn allows [for] the characterisation of volumetric pressure distributions. In case of incompressibility, the 3D divergence becomes time independent. However, local accelerations continue to occur in the description of the Neumann boundary conditions." [50]

4.1.2 Compressibility

"In order to take compressible flow into account, Souverein *et al.* [119] proposed an eligible formulation based on the assumptions of perfect gas and adiabatic flow. The application of the perfect gas law allows [for] the substitution of the density in terms of temperature and pressure. In conjunction with adiabatic flow, the temperature is a function of velocity magnitude

$$\frac{\overline{T}}{\overline{T}_\infty} = 1 + \frac{\gamma + 1}{2} \overline{Ma}_\infty^2 \left(1 - \frac{\overline{V}^2}{\overline{V}_\infty^2} \right), \tag{4.7}$$

where $\overline{T}_\infty$, $\overline{Ma}_\infty$, $\overline{V}_\infty$ are the mean environmental quantities for temperature, Mach number and absolute velocity; γ is the heat capacity ratio. The governing equations are exclusively described by velocity information and material properties. In terms of spray-induced flow, the assumptions of adiabatic flow and perfect gas are considered as feasible in case of negligible mass and heat transfer and moderate temperatures due to the presence of low Mach-numbers [17–21, 25, 27, 120, 121]. Based on the assumptions, the formulations of the URANS equations 4.4 are modified

$$\left(\delta_{ij} + \frac{\overline{u_i' u_j'}}{R\overline{T}} \right) \frac{\partial \overline{p}}{\partial x_j} + \frac{\overline{p}}{R\overline{T}} \left(\frac{\partial \overline{u}_i}{\partial t} + \overline{u}_j \frac{\partial \overline{u}_i}{\partial x_j} + \frac{\partial \left(\overline{u_i' u_j'} \right)}{\partial x_j} - \frac{1}{\overline{T}} \frac{\partial \overline{T}}{\partial x_j} \overline{u_i' u_j'} + \overline{f}_i \right)$$
$$= \frac{\partial}{\partial x_j} \left[\mu \left(\frac{\partial \overline{u}_i}{\partial x_j} + \frac{\partial \overline{u}_j}{\partial x_i} \right) \right] - \frac{2}{3} \frac{\partial}{\partial x_i} \left(\mu \frac{\partial \overline{u}_j}{\partial x_j} \right). \tag{4.8}$$

The 3D and 2D divergences (4.5) and (4.6) are changed accordingly to

$$
\begin{aligned}
&\frac{\partial^2\overline{p}}{\partial x_i\partial x_i}+\frac{\overline{u_i'u_j'}}{R\overline{T}}\frac{\partial^2\overline{p}}{\partial x_i\partial x_j}\\
&+\left[\frac{\partial}{\partial x_j}\left(\frac{\overline{u_i'u_j'}}{R\overline{T}}\right)+\frac{1}{R\overline{T}}\left(\frac{\partial\overline{u}_i}{\partial t}+\overline{u}_j\frac{\partial\overline{u}_i}{\partial x_j}+\frac{\left(\partial\overline{u_i'u_j'}\right)}{\partial x_j}-\frac{1}{\overline{T}}\frac{\partial\overline{T}}{\partial x_j}\overline{u_i'u_j'}+\overline{f}_i\right)\right]\frac{\partial\overline{p}}{\partial x_i}\\
&+\frac{1}{R\overline{T}}\left[-\frac{1}{\overline{T}}\frac{\partial\overline{T}}{\partial x_i}\left(\frac{\partial\overline{u}_i}{\partial t}+\overline{u}_j\frac{\partial\overline{u}_i}{\partial x_j}+\frac{\partial\left(\overline{u_i'u_j'}\right)}{\partial x_j}-\frac{1}{\overline{T}}\frac{\partial\overline{T}}{\partial x_j}\overline{u_i'u_j'}+\overline{f}_i\right)\right.\\
&\left.+\frac{\partial}{\partial x_i}\left(\frac{\partial\overline{u}_i}{\partial t}+\overline{u}_j\frac{\partial\overline{u}_i}{\partial x_j}+\frac{\partial\left(\overline{u_i'u_j'}\right)}{\partial x_j}-\frac{1}{\overline{T}}\frac{\partial\overline{T}}{\partial x_j}\overline{u_i'u_j'}+\overline{f}_i\right)\right]\overline{p}\\
&=\frac{\partial^2}{\partial x_i\partial x_j}\left[\mu\left(\frac{\partial\overline{u}_i}{\partial x_j}+\frac{\partial\overline{u}_j}{\partial x_i}\right)\right]-\frac{2}{3}\frac{\partial^2}{\partial x_i\partial x_i}\left(\mu\frac{\partial\overline{u}_j}{\partial x_j}\right)
\end{aligned}
\tag{4.9}
$$

and

$$
\begin{aligned}
&\frac{\partial^2\overline{p}}{\partial x_1^2}+\frac{\partial^2\overline{p}}{\partial x_2^2}+\frac{\overline{u_1'u_j'}}{R\overline{T}}\frac{\partial^2\overline{p}}{\partial x_1\partial x_j}+\frac{\overline{u_2'u_j'}}{R\overline{T}}\frac{\partial^2\overline{p}}{\partial x_2\partial x_j}+\left[\frac{\partial}{\partial x_1}\left(\frac{\overline{u_1'u_j'}}{R\overline{T}}\right)+\frac{\partial}{\partial x_2}\left(\frac{\overline{u_2'u_j'}}{R\overline{T}}\right)\right]\frac{\partial\overline{p}}{\partial x_j}\\
&+\frac{1}{R\overline{T}}\left(\frac{\partial\overline{u}_1}{\partial t}+\overline{u}_j\frac{\partial\overline{u}_1}{\partial x_j}+\frac{\partial\left(\overline{u_1'u_j'}\right)}{\partial x_j}-\frac{1}{\overline{T}}\frac{\partial\overline{T}}{\partial x_j}\overline{u_1'u_j'}+\overline{f}_1\right)\frac{\partial\overline{p}}{\partial x_1}\\
&+\frac{1}{R\overline{T}}\left(\frac{\partial\overline{u}_2}{\partial t}+\overline{u}_j\frac{\partial\overline{u}_2}{\partial x_j}+\frac{\partial\left(\overline{u_2'u_j'}\right)}{\partial x_j}-\frac{1}{\overline{T}}\frac{\partial\overline{T}}{\partial x_j}\overline{u_2'u_j'}+\overline{f}_2\right)\frac{\partial\overline{p}}{\partial x_2}\\
&+\frac{1}{R\overline{T}}\left[\frac{\partial}{\partial x_1}\left(\frac{\partial\overline{u}_1}{\partial t}+\overline{u}_j\frac{\partial\overline{u}_1}{\partial x_j}+\frac{\partial\left(\overline{u_1'u_j'}\right)}{\partial x_j}-\frac{1}{\overline{T}}\frac{\partial\overline{T}}{\partial x_j}\overline{u_1'u_j'}+\overline{f}_1\right)\right.\\
&+\frac{\partial}{\partial x_2}\left(\frac{\partial\overline{u}_2}{\partial t}+\overline{u}_j\frac{\partial\overline{u}_2}{\partial x_j}+\frac{\partial\left(\overline{u_2'u_j'}\right)}{\partial x_j}-\frac{1}{\overline{T}}\frac{\partial\overline{T}}{\partial x_j}\overline{u_2'u_j'}+\overline{f}_2\right)\\
&-\frac{1}{\overline{T}}\frac{\partial\overline{T}}{\partial x_1}\left(\frac{\partial\overline{u}_1}{\partial t}+\overline{u}_j\frac{\partial\overline{u}_1}{\partial x_j}+\frac{\partial\left(\overline{u_1'u_j'}\right)}{\partial x_j}-\frac{1}{\overline{T}}\frac{\partial\overline{T}}{\partial x_j}\overline{u_1'u_j'}+\overline{f}_1\right)\\
&\left.-\frac{1}{\overline{T}}\frac{\partial\overline{T}}{\partial x_2}\left(\frac{\partial\overline{u}_2}{\partial t}+\overline{u}_j\frac{\partial\overline{u}_2}{\partial x_j}+\frac{\partial\left(\overline{u_2'u_j'}\right)}{\partial x_j}-\frac{1}{\overline{T}}\frac{\partial\overline{T}}{\partial x_j}\overline{u_2'u_j'}+\overline{f}_2\right)\right]\overline{p}\\
&=\frac{\partial^2}{\partial x_1\partial x_j}\left[\mu\left(\frac{\partial\overline{u}_1}{\partial x_j}+\frac{\partial\overline{u}_j}{\partial x_1}\right)\right]+\frac{\partial^2}{\partial x_2\partial x_j}\left[\mu\left(\frac{\partial\overline{u}_2}{\partial x_j}+\frac{\partial\overline{u}_j}{\partial x_2}\right)\right]\\
&-\frac{2}{3}\left[\frac{\partial^2}{\partial x_1^2}\left(\mu\frac{\partial\overline{u}_j}{\partial x_j}\right)+\frac{\partial^2}{\partial x_2^2}\left(\mu\frac{\partial\overline{u}_j}{\partial x_j}\right)\right],
\end{aligned}
\tag{4.10}
$$

respectively[, where R is the specific gas constant].
The 2D and 3D divergences are second order partial differential equations with mixed partial derivatives. Note that the in-plane divergence of the URANS equations is no longer 2D but 3D due to the occurrence of corresponding first and second order mixed partial derivatives originating from the Reynolds shear stresses. [...] However, in case of negligible Reynolds shear stresses, the in-plane partial differential equation remains 2D." [50]

4.1.3 Viscosity

"In the present work, the dynamic viscosity is described by Sutherland's law [122], which is based on the kinetic gas theory. It describes the dynamic viscosity as a function of temperature. By the assumptions of perfect gas and adiabatic flow, a substitution of the temperature in terms of Equation 4.7 provides a description of the dynamic viscosity exclusively dependent on flow variables and additional material and model coefficients. Sutherland's law is given by

$$\mu = \mu_0 \left(\frac{\overline{T}}{T_0} \right)^{\frac{3}{2}} \frac{T_0 + S}{\overline{T} + S}, \tag{4.11}$$

where S is the Sutherland's temperature, T_0 is a reference temperature and μ_0 is the dynamic viscosity at the reference temperature T_0." [50]

4.1.4 Reynolds stresses

"The Reynolds stresses are determined by the variance and covariance of the sample populations of the velocity components. The equations 4.12 and 4.13 are estimates of the parent population and converge for $N \to \infty$ to the exact value." [50]

Reynolds normal stresses:

$$R_{u_i u_i} = \sigma_{u_i}^2 = \frac{1}{N-1} \sum_{n=1}^{N} (u_{i,n} - \overline{u}_i)^2 \tag{4.12}$$

Reynolds shear stresses:

$$R_{u_i u_j} = \sigma^2_{u_i u_j} = \frac{1}{N-1} \sum_{n=1}^{N} \left(u_{i,n} - \overline{u}_i\right) \left(u_{j,n} - \overline{u}_j\right), \; i \neq j \tag{4.13}$$

As the standard deviation of the velocity contains both contributions from true velocity fluctuations, including turbulence and injection stochastics, and fluctuations from random errors, the Reynolds normal and shear stresses are subject to potential systematic errors. If the uncertainties of the measured velocities are quantified or otherwise known, a more accurate estimate of the Reynolds stresses can be obtained. In terms of the Reynolds normal stresses, a correction can be made by subtracting the mean square of the instantaneous velocity uncertainties $\overline{U^2_{u_i}}$ from the measured Reynolds normal stresses – $R_{u_i u_i,corr} = R_{u_i u_i} - \overline{U^2_{u_i}}$ [123]. For the Reynolds shear stresses, there is no systematic error if there is no correlation between the errors of the velocity components. Depending on the experimental setup and camera configuration, a stereo PIV measurement may lead to proportionate systematic errors as reported by Sciacchitano & Wieneke [123]. However, systematic errors of Reynolds shear stresses are usually, by definition, much smaller than those of Reynolds normal stresses.

4.2 Uncertainty quantification

"The assessment of measurement accuracy is essential in order to identify an uncertainty interval that covers the actual value of the measurement quantity. Throughout the procedure of PIV measurement and pressure evaluation, multiple sources of systematic and random errors contribute to the final pressure uncertainty. As a selection of contributions, there are errors due to the PIV setup, velocity evaluation, assumptions, models, numerics, statistics, boundary conditions and imperfect experimental repeatability. Furthermore, the present case implies injection stochastics as an additional uncertainty source. Regarding the PIV setup, errors may arise due to misalignment, optical aberrations, insufficient calibration and temporal discretisation. The implementation of models and assumptions such as perfect gas, adiabatic flow or incompressibility poses additional

sources of error. Furthermore, numerical differentiation, discretisation, statistical convergence and linearisation contribute to the resulting pressure accuracy.
A Bayesian framework for the uncertainty quantification of PIV-based pressure evaluation was proposed [by Azijli *et al.*] [124], which allows the combination of retrieved velocity uncertainties with a priori knowledge about the velocity field. The combined velocity uncertainties are successively propagated to the pressure field by either analytic expressions or Monte Carlo simulation." [50]
In this thesis, a methodology was developed which enables the uncertainty quantification of pressure within the statistical approach based on URANS and ensemble-averaging. The methodology includes the quantification of uncertainty from PIV evaluation and the subsequent propagation to the statistical quantities of ensemble-averaged velocity, Reynolds normal and shear stresses, and eventually ensemble-averaged pressure. The propagation of uncertainty is performed using analytical expressions and Monte Carlo simulation. A schematic illustration of the stepwise processing within the uncertainty quantification is shown in 4.1.

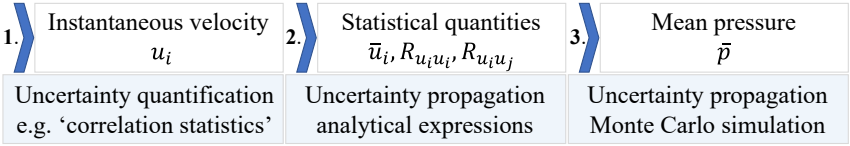

Figure 4.1: Process diagram of the uncertainty quantification used [50].

4.2.1 Uncertainty quantification of instantaneous velocities

For the estimation of random errors in PIV evaluation, different a posteriori uncertainty quantification methods were proposed. In Timmins *et al.* [125], the results of Monte Carlo simulations on synthetic data are used as a look-up table to estimate the velocity uncertainty as a function of particle density, particle image size, displacement and shear. In Charonko & Vlachos [126], the velocity uncertainty is empirically estimated by the

ratio between the highest and the second highest correlation peak ('peak ratio' method). In Sciacchitano *et al.* [127], residual particle displacements of matched particle image pairs are used for uncertainty quantification ('particle disparity' method). In Wieneke [128], the velocity uncertainty is estimated by a statistical analysis of the PIV correlation process using differences in the intensity pattern of a matched image pair ('correlation statistics' method). The method has shown good results on synthetic data for random Gaussian noise, particle image sizes, particle densities and in-plane and out-of-plane particle motions.
A review and comparative assessment of the available a posteriori uncertainty quantification methods is given in Sciacchitano *et al.* [129].

4.2.2 Uncertainty propagation of the instantaneous velocities to the ensemble-averaged velocity field and Reynolds stresses

For the propagation of the instantaneous velocity uncertainties to the ensemble-averaged velocity field and Reynolds normal and shear stresses, analytical expressions derived in Sciacchitano & Wieneke [123] are used. Assuming independent samples and normally distributed standard deviations σ_{u_i} of the instantaneous velocities u_i with index $i = 1, 2, 3$, the expressions of the standard uncertainties are:

Uncertainty of mean velocities:

$$U_{\overline{u}_i} = \frac{\sigma_{u_i}}{\sqrt{N}} = \frac{\sqrt{\sum_{n=1}^{N} \left(u_{i,n} - \overline{u}_i\right)^2}}{\sqrt{(N-1)N}} \tag{4.14}$$

Uncertainty of Reynolds normal stresses:

$$U_{R_{u_i u_i}} = \sigma_{u_i}^2 \sqrt{\frac{2}{N-1}} = R_{u_i u_i} \sqrt{\frac{2}{N-1}} \tag{4.15}$$

Uncertainty of Reynolds normal stresses (corrected):

$$\begin{aligned} U_{R_{u_iu_i},corr} &= \sqrt{U^2_{R_{u_iu_i}} + U^2_{\overline{U^2_{u_i}}}} \\ &= \sqrt{R^2_{u_iu_i} + \left(\sqrt{2}\sigma_{U_{u_i}}\overline{U_{u_i}}\sqrt{1+\frac{\sigma^2_{U_{u_i}}}{2\overline{U_{u_i}}^2}}\right)^2} \cdot \sqrt{\frac{2}{N}} \end{aligned} \tag{4.16}$$

Uncertainty of Reynolds shear stresses:

$$U_{Ru_iu_j} = \sigma_{u_i}\sigma_{u_j}\sqrt{\frac{1+\rho^2_{u_iu_j}}{N-1}}, \text{ with } i \neq j = 1,2,3 \tag{4.17}$$

$$\rho_{u_iu_j} = \frac{R_{u_iu_j}}{\sigma_{u_i}\sigma_{u_j}} \tag{4.18}$$

U_{u_i} is the standard deviation of the instantaneous velocity u_i. $\overline{U_{u_i}}$ and $\sigma_{U_{u_i}}$ are the associated mean and standard deviation of the uncertainty U_{u_i}. $U_{\overline{U^2_{u_i}}}$ is the uncertainty of the mean-square uncertainty $\overline{U^2_{u_i}}$ and $\rho_{u_iu_j}$ is the cross-correlation coefficient of the velocity components u_i and u_j.

4.2.3 Uncertainty propagation to the pressure field

In the present work, the uncertainty propagation from the statistical quantities to the ensemble-averaged pressure field is realised by Monte Carlo simulation. The method is well-suited for non-linear problems, such as the governing equations of velocimetry-based pressure evaluation are. The Monte Carlo simulation is carried out by performing several pressure evaluations with randomly generated velocity fields based on the mean values and uncertainties of the statistical quantities. The resulting distribution of the pressure values are used to quantify the uncertainty of the ensemble-averaged pressure field. The procedure does not take into account systematic uncertainties due to spatial and temporal resolution, spatial correlation [123, 124] and boundary conditions.

5 Experimental setup and evaluation

This chapter describes the basic setup, procedure and post-processing of the PIV and pressure evaluation used in the present thesis for the analysis of spray-induced flows. Specifications on the individual experiments and investigations such as the spray layout, operating conditions and measurement configurations are given in the respective sections.

5.1 Experimental setup

The experiments are carried out on a test bench with an optically accessible, pressurised chamber and supplementary units for the control of injection pressure, back pressure, fuel temperature, chamber circulation, particle seeding and injection control. Figure 5.1 shows the arrangement of the Stereo-PIV setup used. The setup comprises two CMOS cameras (*Phantom v1612*) and a double-pulsed Nd-YAG laser (*Photonics DM100-532*) with a wavelength of light of 532 nm. For imaging, macro lenses with fixed focal lengths of 100 mm (*Tokina AT-X M100 AF Pro D*) and 200 mm (*NIKON AF Micro-Nikkor*) are employed. The laser-light sheet is spanned by a collimator optic and introduced perpendicular to the observation view. The test bench allows for a fine positioning and traversing of the cameras and the light-sheet optics.
Two different injector positions are used – a top-mounted position that provides a longitudinal section in line with the propagation of spray and a side-mounted position that allows the flow to be studied in between the spray plumes, as illustrated on the right hand side of Figure 5.1.
To ensure inert gas composition, the chamber is constantly flushed by nitrogen circulation. The impact of the circulation on the spray-induced

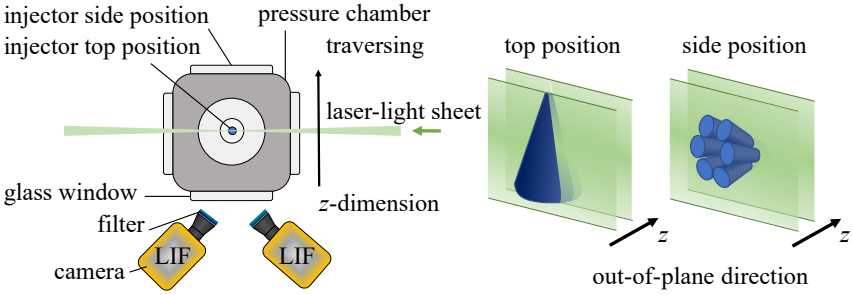

Figure 5.1: Experimental setup used for the velocimetry of spray-induced flow. Adapted from [50].

flow is considered negligible due to its low and steady flow. For the supply of particle seeding, an aerosol generator according to the Laskin-nozzle [10] principle is used. The tracer aerosol is supplied via the nitrogen circulation to promote uniform seeding. In previous works on spray-induced flow measurement, Rhodamine B [24], Rhodamine 6G [27] and DCM [19, 22, 23] were used as fluorescent tracer medium for an excitation wavelength of 532 nm (Nd:YAG laser). In the present work, a solution of propylene carbonate and fluorescent DCM dye (0.2 g/l [19]) is employed. DCM has been reported as an efficient laser dye with fluorescent emission at a wavelength of 630 – 680 nm [130]. It is particularly suited for an excitation wavelength of 532 nm due to its pronounced frequency shift. For optical filtering, the cameras are equipped with OD4 long-pass filters with a cut-off wavelength of 600 nm and a transmission range from 610 – 1650 nm.

5.2 PIV and pressure evaluation

For the PIV evaluation, an iterative multi-grid, multi-pass evaluation scheme [131, 132] with window deformation [111] and Gaussian peak fit [10] is used. Outliers are detected and removed by a normalised median filter [108] (3×3 neighborhood). The ensemble-averaged velocities and Reynolds stresses are calculated by a number of about 50 measurement samples to provide statistical significance. If required, the out-of-plane velocity

gradients are reconstructed based on the measurement in several successive out-of-plane positions (traversing) using finite differences. The spacing between the measurement planes is set in the order of an interrogation area depending on the FOV.
The pressure evaluation is carried out on the basis of a self-developed in-house code. As the velocity field contour changes with spray propagation, the code is designed to automatically analyse available information of neighbouring nodes, both in space and time, to adjust the computational domain and the type of used differencing scheme (forward, backward and central differencing scheme) accordingly. Depending on the degree of modelling, whether compressible or incompressible, with or without Reynolds stresses, viscosity and body forces, the underlying governing equations are adapted.
For the solution of the partial differential equation (PDE), Neumann boundary conditions (Equation 4.4) are used almost exclusively, especially in the vicinity of spray and areas of unsteady flow. To impose uniqueness of the solution, Dirichlet boundary conditions are set in the far field, where ambient conditions apply. In the scope of the present work only a few boundary nodes are selected as Dirichlet boundary conditions. The location of the Dirichlet boundary condition is determined by the minimum of the time- and space-averaged norm of the pressure gradient, which proved to be a particularly well-suited criterion to identify boundary nodes for ambient flow conditions. The Dirichlet boundary condition is set according to the prevailing ambient gas pressure.

6 Pressure evaluation of spray-induced flow

In the present chapter, the spray-induced flow of a GDI research sample is investigated by means of velocimetry-based pressure evaluation using the statistical approach based on URANS and ensemble averaging [50] according to Chapter 4. For the purpose of validation and analysis, the investigation includes a comparative pressure sensor measurement, an uncertainty quantification of the pressure evaluation, and a scale and sensitivity analysis of the governing equations and modelling. In part, the results were published in the works of Kling *et al.* [50, 121]. In this chapter, the same nomenclature applies as in Chapter 4.

6.1 Pressure evaluation of the spray-induced flow of a two-hole nozzle

For the investigation, a two-hole research sample with large spray hole inclination angles φ_{SH} was used to ensure good optical accessibility and to allow for a convenient integration of a pressure transducer without interfering sensor wetting. The measurements were carried out under non-flash-boiling conditions ($Ja = -5243$) at $p_\infty = 1$ bar ambient gas pressure, $T_{fuel} = 25°\text{C}$ fuel temperature, $T_\infty = 25°\text{C}$ ambient gas temperature and $p_{inj} = 100$ bar injection pressure, while n-heptane was used as fuel. The velocimetry of spray-induced flow was conducted with an acquisition frequency of $f_{acq} = 5$ kHz, an interframing time of $\mathrm{d}t_{PIV} = 20$ μs and a FOV of 127×82 mm^2. The statistical quantities were calculated based on 50 measurement samples.
In Figure 6.1, the resultant ensemble-averaged velocity and pressure fields

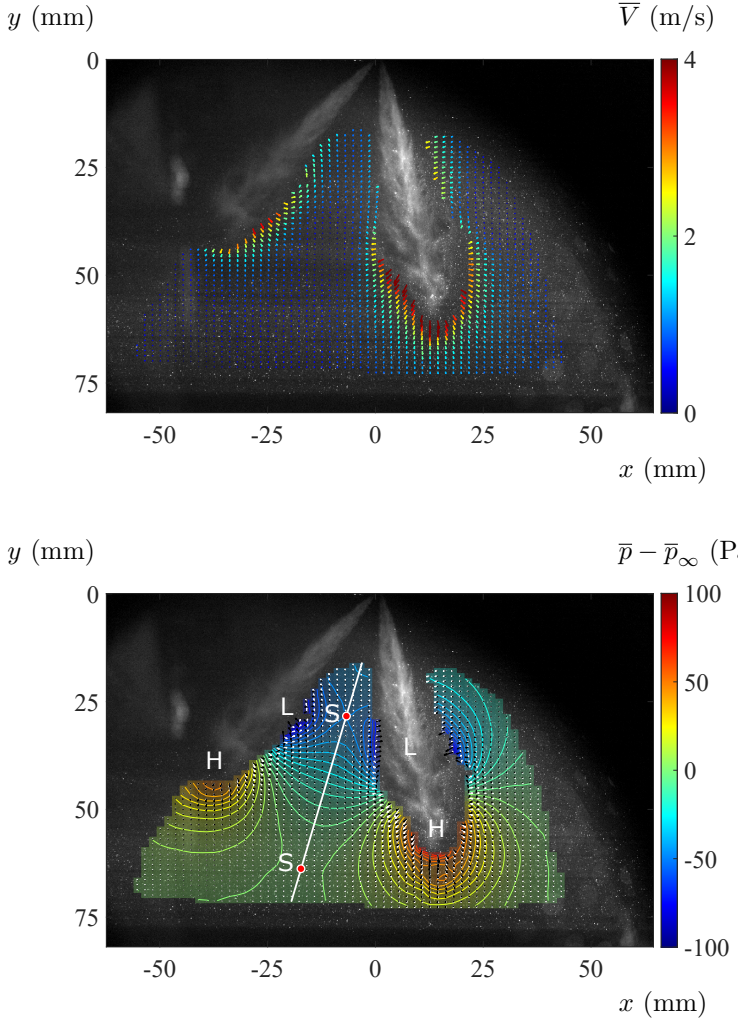

Figure 6.1: Ensemble-averaged velocity and pressure fields of the spray-induced flow of a two-hole GDI spray. Labels: low pressure area (L), high pressure area (H), saddle point (S), vanishing material acceleration in normal direction (white line). Absolute ensemble-averaged velocity $\overline{V}$.

of the spray-induced flow are shown. The velocity field indicates typical flow structures like entrainment, displacement and recirculation flow. The greatest velocities are observed at the spray plume tips and in the upstream areas of the gas entrainment. In accordance with the flow field, the pressure distribution shows high and low pressures, which are associated with the displacement and entrainment flows, respectively. The displacement flows are characterised by high pressures at the spray plume tips, while the entrainment flows are accompanied by low pressures towards the central areas of the spray plumes. The differential pressures in the spray surrounding are in the order of 100 Pa. As the contour lines indicate, significantly higher differential pressures are to be expected in the hidden flow regime of the spray (blind spot of velocimetry). The pressure distribution in the area between the spray plumes shows a spatial separation in terms of material acceleration. Along the white line, the pressure gradient disappears in the normal direction. Depending on the relative position, a liquid mass is accelerated to either one or the other spray plume. At the saddle points (S) the pressure gradient also disappears in tangential direction. In the area between the saddle points, from the displacement to the entrainment flow and presumably beyond that to the the wake flow, the fluid masses experience an acceleration in the direction of the spray plumes.

6.2 Comparative assessment with a pressure sensor measurement

In order to assess the pressure evaluation of spray-induced flow using URANS and ensemble averaging, a comparative measurement with a piezoelectric sensor (*PCB-106B50*) was carried out. The pressure sensor is specifically designed for small dynamic pressures such as for turbulence, noise and pulsations. For the measurements, the pressure sensor was mounted on a stand and positioned in between the spray plumes of the 2-hole spray, as shown in Figure 6.2. The position is particularly suitable as it is likely to provide a sequence of the characteristic high and low pressures of the displacement, entrainment and wake flow. The measurement was performed separately from the PIV measurement. The signal was acquired with an oscilloscope. The used acquisition frequency of the

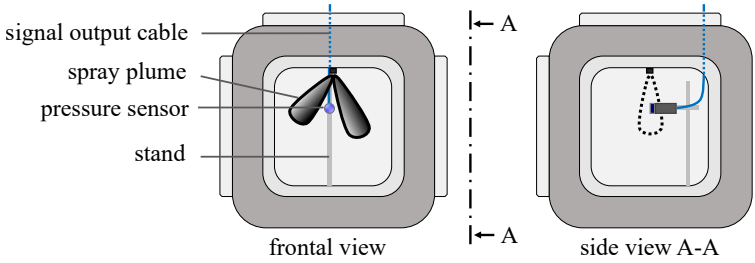

Figure 6.2: Experimental setup used for the pressure measurement with the piezoelectric sensor [50]. The pressure sensor was mounted on a stand and placed between the spray plumes of the 2-hole spray.

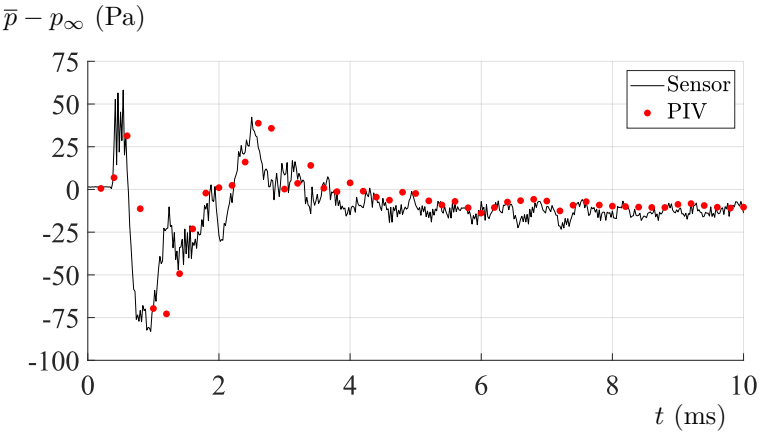

Figure 6.3: Measured temporal course of the ensemble-averaged pressure in the area between the spray plumes [50]; black curve - pressure sensor, red dots - pressure from PIV.

measurement is 100 kHz. While the pressure transducer has a nominal resolution of 0.61 Pa, the obtained signal shows a noise level of about 2.2 Pa. Consistent with the pressure from PIV evaluation, the results of 50 injection events were processed to calculate the ensemble-averaged pressure equivalently. To match the results from pressure from PIV and the pressure sensor measurement, the relative position of the pressure transducer was determined by using image calibration.
In Figure 6.3, the temporal course of the ensemble-averaged pressure is shown for the results of the pressure from PIV evaluation and from the pressure sensor measurement. The abscissa origin corresponds to the SOI. The results show a good level of agreement, both qualitatively and quantitatively. The successive maxima and minima of displacement, entrainment and wake flow as well as the subsequent flow attenuation are well reproduced. The result of the pressure sensor measurement confirms the magnitude of the occurring pressure differences predicted by the pressure from PIV evaluation. The differential pressures range between -80 and 60 Pa. Higher frequencies as indicated by the pressure sensor measurement are not covered by the temporal resolution of the velocimetry and pressure from PIV evaluation.

6.3 Uncertainty quantification

To further assess the introduced methodology of pressure evaluation of spray-induced flow by means of URANS and ensemble averaging, an uncertainty quantification and analysis was carried out according to Section 4.2. For the quantification of the instantaneous velocity uncertainties, the correlation statistics method [128] was employed. The statistical quantities and their corresponding uncertainties were computed using 50 measurement samples. The uncertainty propagation to the ensemble-averaged pressure field was done by a Monte Carlo simulation with 2.000 iterations. As shown in Figure 6.4, the Monte Carlo simulation reached advanced convergence for such a number of iterations. The standard uncertainties of the mean and standard deviation of the ensemble-averaged pressure are about $U_{\overline{U_{\overline{p}}}} = 10^{-1}$ Pa and $U_{\sigma_{U_{\overline{p}}}} = 10^{-1}$ Pa, which implies that there is practically no additional uncertainty to the ensemble-averaged pressure field due to Monte Carlo simulation.

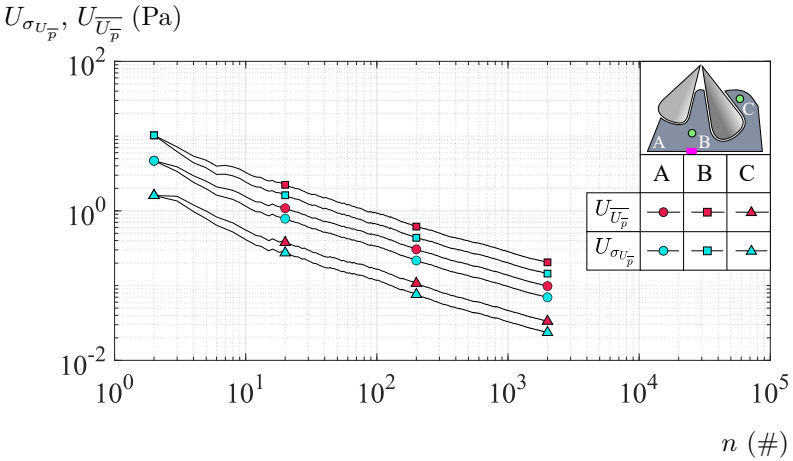

Figure 6.4: Convergence of the Monte Carlo simulation illustrated by the mean and standard deviation of the ensemble-averaged pressure uncertainty as a function of n iterations. The uncertainties are shown for three different scenarios/locations: (A) spatially averaged, (B) at close distance to the Dirichlet boundary nodes, (C) in far distance to the Dirichlet boundary nodes. The Dirichlet boundary nodes are marked with magenta color in the sketch.

In Figure 6.5, the mean and standard uncertainty of the instantaneous velocity uncertainty are shown. The largest values of velocity uncertainty are observed in the vicinity of spray. To some extent the larger values are traced back to the flow field, however, as the uncertainty significantly increases at the interface between spray and ambient gas, a likely cause for the increase is due to the interfering influence of the imaged spray on the PIV evaluation. At the interface between the spray and the surrounding gas flow, the PIV evaluation is subject to spurious contributions from the spray propagation and a reduced signal-to-noise ratio. The standard uncertainty of the instantaneous velocity uncertainties shows a good level of confidence in the estimate of the mean instantaneous velocity uncertainty.
In Figure 6.5d, the estimated uncertainty of the ensemble averaged velocity is shown. In contrast to the mean of the instantaneous velocity uncertainty (Figure 6.5a), the level of uncertainty is nearly zero for most of the evalua-

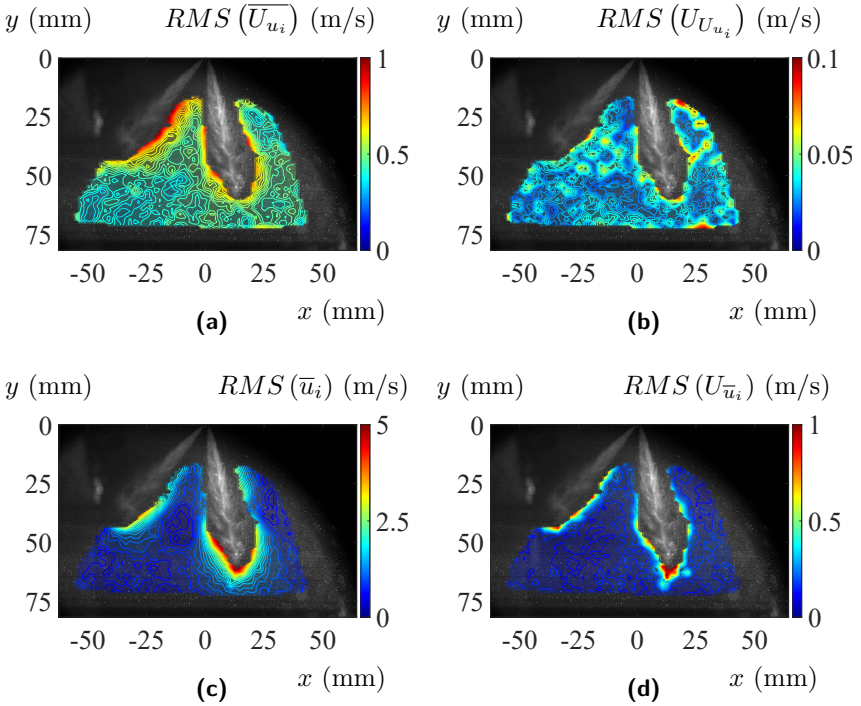

Figure 6.5: Velocity magnitude and associated uncertainties: (a) mean of the instantaneous velocity uncertainties, (b) uncertainty of the instantaneous velocity uncertainties, (c) ensemble-averaged velocity, (d) uncertainty of the ensemble-averaged velocity. The uncertainties are represented as root mean square square (RMS).

tion domain. Consequently, in terms of random errors from PIV evaluation there is a good confidence in the values of the ensemble-averaged velocity field. However, in the vicinity of the spray, larger values are observed, especially in the area of the spray plume tip. Besides the contribution of turbulence and random errors from PIV evaluation, the increased velocity uncertainty is attributed to the influence of injection stochastics. The variance in spray formation and spray propagation leads to a rather strong variation in local velocities, especially in the close vicinity of the spray, where there is a high sensitivity to changes in spray transport and spray-gas interaction. The increased uncertainty at the spray plume tip is likely due to the variation in spray tip penetration. Random errors from PIV evaluation are not expected to be causal, since no correlation with the uncertainty of the instantaneous velocity uncertainty is observed (Figure 6.5b). With increasing number of considered measurement samples, the ensemble-averaged velocity field (Figure 6.5c) converges towards the actual values, assuming no bias error.
Consistent with the definition, the Reynolds normal and shear stresses as well as the corresponding uncertainties show qualitatively similar distributions to that of the standard uncertainty of the ensemble-averaged velocity field, as shown in Figure 6.6. While there are large values in the vicinity of the spray, most of the evaluation domain features comparatively low values. In contrast to the estimation of the ensemble-averaged velocity, the Reynolds normal stresses and in some cases the Reynolds shear stresses (correlation of error [123]) inherently include undesired contributions of random errors and injection stochastics, which can not be addressed by additional measurement samples but by knowledge about the respective contributions. In terms of random errors from PIV evaluation, the mean square of the instantaneous velocity uncertainty $\overline{U_{u_i}^2}$ is used as estimate for the correction of the Reynolds normal stresses (see Section 4.1.4). In the present case, the Reynolds normal stresses adjust noticeably to smaller values, as illustrated in figures 6.6a and 6.6c. High values, however, are still present in the close range of the spray. As there is no differentiation between injection stochastics and turbulence, the Reynolds stresses, particularly the Reynolds normal stresses, tend to be overestimated. Generally, though, the Reynolds stresses are typically underestimated as turbulent flow is usually not fully resolved by the spatial and temporal resolution of the PIV measurement, as was demonstrated by the comparative pressure sensor measurement in Section 6.2.

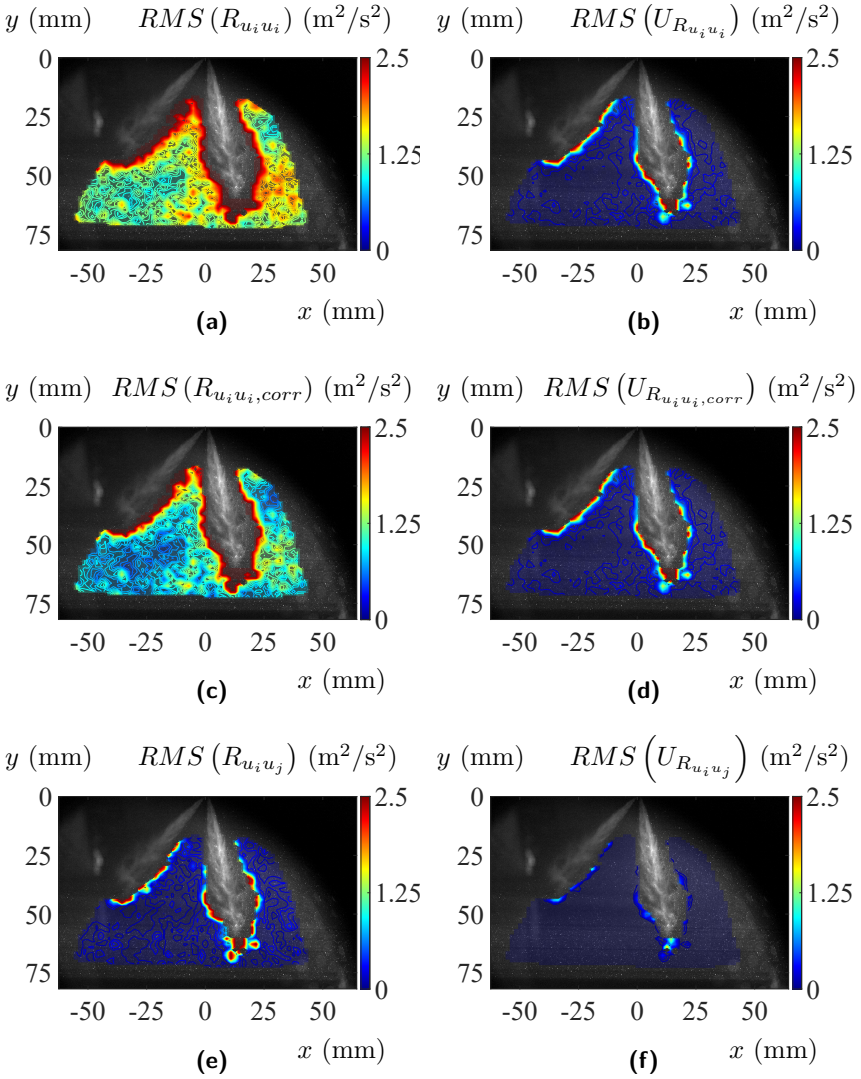

Figure 6.6: Reynolds normal and shear stresses as well as associated uncertainties. The quantities are represented as RMS.

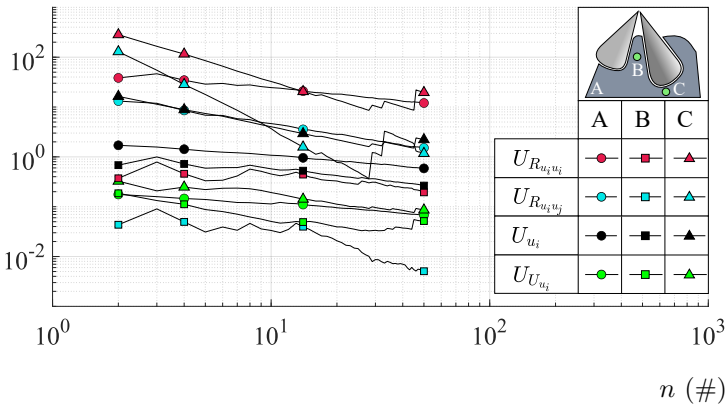

Figure 6.7: The influence of the considered measurement samples on the uncertainty of the Reynolds stresses, the instantaneous velocities and the ensemble-averaged velocities. The uncertainties are shown for three different scenarios/locations in double logarithmic representation: (A) spatially averaged, (B) in the spray plume interspace, (C) at the spray plume tip. The uncertainties are presented as RMS.

In Figure 6.7, the convergence of the ensemble-averaged velocity, instantaneous velocity uncertainty and Reynolds normal and shear stresses are shown as a function of measurement samples for three different scenarios/locations - spatially averaged (A), in the spray plume interspace (B) and at the spray plume tip (C). The quantities are represented in double logarithmic representation. In linear approximation, the quantities converge roughly with the expected -1/2 gradient, which is typical for the standard uncertainty. Overall, the quantities reach a good level of confidence for 50 measurement samples. Especially in the spray plume interspace (B), where there is low interfering influence by injection stochastics or random errors from PIV evaluation, the values reach a particular low level. In the vicinity of the spray (A), on the other hand, the uncertainties of the ensemble-averaged velocity and the Reynolds stresses are about one and two orders higher compared to the values in the surrounding gas flow (B). As shown in Figure 6.8, the uncertainties of the velocity field and Reynolds

stresses have propagated to the ensemble-averaged pressure gradient and pressure. In agreement with previous observations, the largest values are observed in the vicinity of the spray with a substantial peak at the spray plume tip. The ensemble-averaged pressure field shows an accumulation of uncertainty over the range of evaluation, starting from the Dirichlet boundary conditions. The distribution demonstrates the importance of defining proper and spatially distributed Dirichlet boundary conditions to minimise the effect of uncertainty accumulation or error propagation. In the present case, the limited FOV restricts the definition of additional reliable Dirichlet boundary conditions close to the desired remote areas. The ensemble-averaged pressure field indicates some irregular pressure values in the area of displacement flow (A) (Figure 6.8c). Using 50 measurement samples for the calculation of the statistical quantities and a single location with Dirichlet boundary conditions, the uncertainty quantification estimates a pressure uncertainty of up to 10 Pa in the remote area (B) (Figure 6.8d) and a peak value of 15 Pa at the spray plume tip.
Although the pressure field suggests a rather accurate evaluation, some flawed pressure values are observed in front of the spray plume tip in the area of displacement flow (A). As shown in Figure 6.9, the spurious values are attributed to the contribution of Reynolds stresses, respectively injection stochastics. By omitting the Reynolds Stresses from the pressure evaluation, the spurious values disappear. A selective omission of irregular Reynolds Stresses can markedly improve the accuracy of the evaluated pressures, as indicated by the reduced degree of uncertainty in Figure 6.9b.
Unlike many other flows, the pressure evaluation of spray-induced flow requires the adaptation of the numerical approximation as the range of evaluation changes in time through the propagation of spray. The use of forward and backward differences is a viable measure to account for the changing domain of evaluation and to ensure a pressure evaluation that is close to the spray, especially in the area of displacement flow. In Figure 6.10, the differencing schemes used for the present case numerical approximation of the local acceleration are shown. It shall be noted, that in case of a coarse temporal resolution, the numerical approximation might be insufficient for an accurate evaluation. In the present case, however, the temporal resolution seems to be adequate, as there is no visible pressure plateau at the displacement flow, which is typical in such a case.

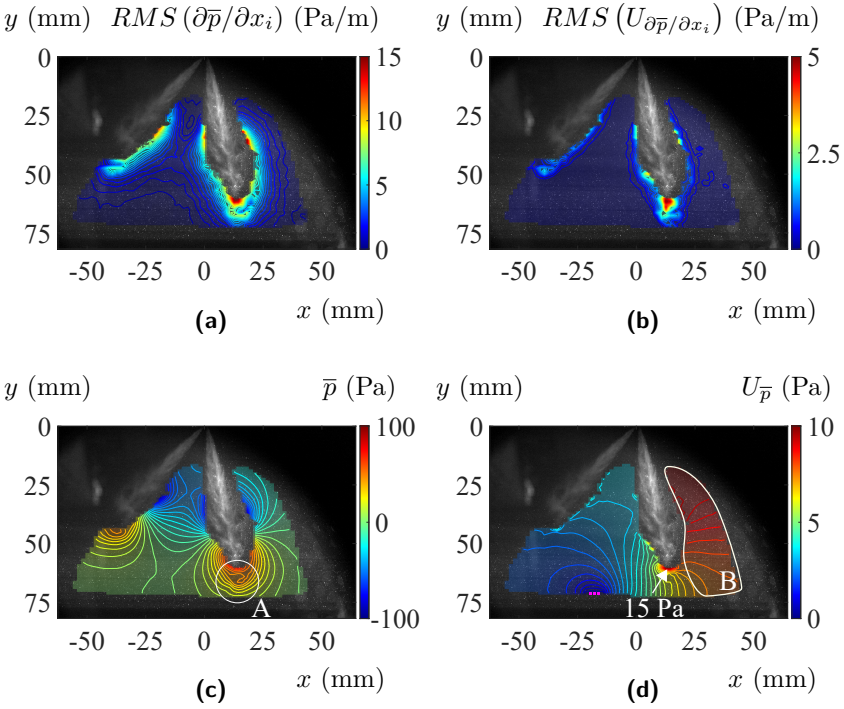

Figure 6.8: Values and uncertainties of the ensemble-averaged pressure gradient and the ensemble-averaged pressure. (a) ensemble-averaged pressure gradient, (b) uncertainty of the ensemble-averaged pressure gradient, (c) ensemble-averaged pressure, (d) uncertainty of the ensemble averaged pressure. The pressure gradient is represented as RMS. Dirichlet boundary nodes are marked with magenta color.

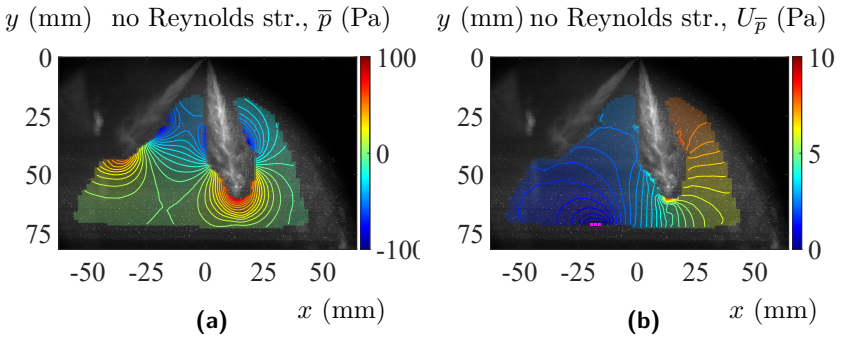

Figure 6.9: Evaluated pressure field and corresponding uncertainty when omitting the contribution of the Reynolds stress terms. (a) ensemble-averaged pressure, (b) uncertainty of the ensemble-averaged pressure. Dirichlet boundary nodes are marked with magenta color.

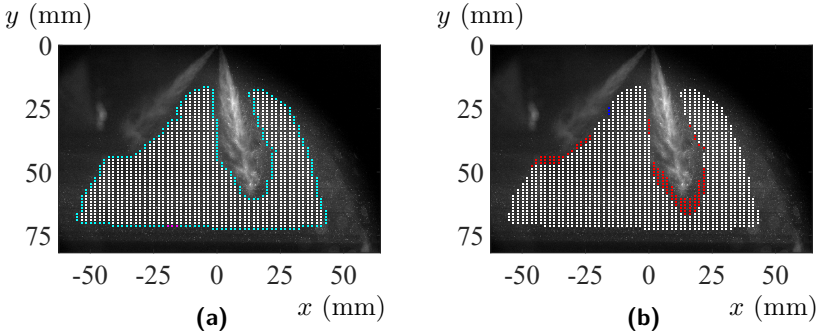

Figure 6.10: "Evaluation domain with color coded nodes representing the implemented boundary conditions and differencing schemes; left - boundary conditions: magenta - Dirichlet boundary condition, cyan - Neumann boundary condition, white - inner node; right - used differencing schemes for the calculation of the time derivatives: white - central differecing scheme, blue - forwards differencing scheme; red - backwards differencing scheme; background: raw image." [50]

6.4 Scale and sensitivity analysis

A scale and sensitivity analysis was carried out to identify possible measures to optimise or simplify the methodology of pressure evaluation of spray-induced flow. In Figure 6.11, the scales of local acceleration, convective acceleration, Reynolds stresses, viscosity and gravity are shown in relation to the pressure gradient. For the present flow, the local acceleration is identified as the major term. Over the entire range of evaluation, the local acceleration is in the order of the pressure gradient. A good temporal resolution is therefore desirable for an accurate pressure evaluation. It should be noted that the statistical approach allows a refinement of the temporal resolution by performing time-shifted measurements. For some setups and applications, this capability is of great value as it allows to overcome possible limitations of the measurement technology used. The convective acceleration and Reynolds stresses, on the other hand, are spatially confined to the close vicinity of the spray. At a comparatively short distance, the values drop by an order of magnitude. With respect to viscosity and gravity, a negligible effect is observed. In the relevant areas of spray-induced flow, the scales are at least three orders of magnitude smaller than the pressure gradient.
In Figure 6.12 the influence of convective acceleration, Reynolds stresses and compressibility on the result of the pressure evaluation of the spray-induced flow is illustrated. The differential pressures shown describe the difference between a full modelling and a modelling that excludes corresponding terms or physics. The omission of the convective acceleration and Reynolds stresses results in a pressure difference of up to 10 and 20 Pa respectively. The largest differential pressures are observed in the vicinity of the spray, at the spray plume tip (A) (Figure 6.12b) and in the area remote from the Dirichlet boundary conditions (B) (Figure 6.12a). Under the assumption of low mass and heat transfer, the compressibility has a negligible effect on the result of the pressure evaluation as shown Figure 6.12c.

6.5 Discussion

For the first time, the pressure field of a spray-induced flow was experimentally quantified. The ability to quantify pressure fields adds an important fluid mechanical quantity to the existing spectrum for spray analysis and

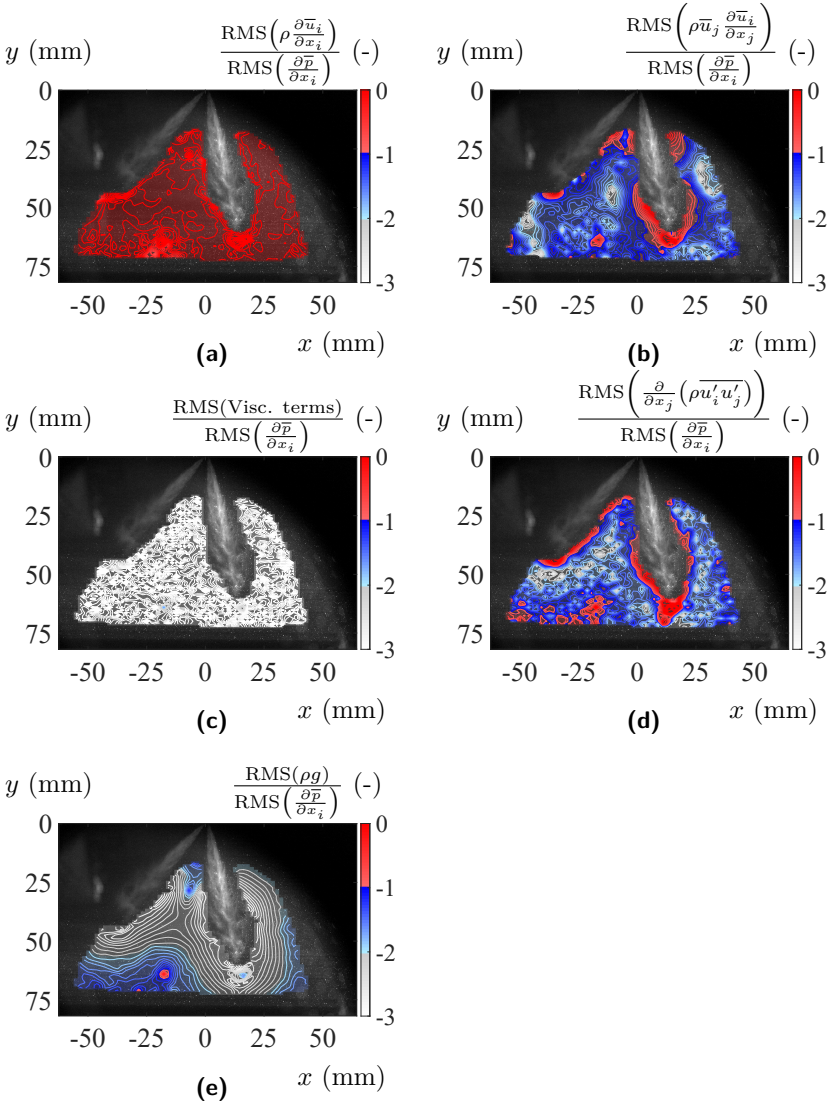

Figure 6.11: Scale analysis [50] showing the ratios between individual terms of the URANS equations and the pressure gradient: (a) local acceleration, (b) convective acceleration, (c) viscosity, (d) Reynolds stresses, (e) gravity, where g is the gravitational force. Contours: red - O(0) to O(-1) to O(2), white - O(-2) to O(-3).

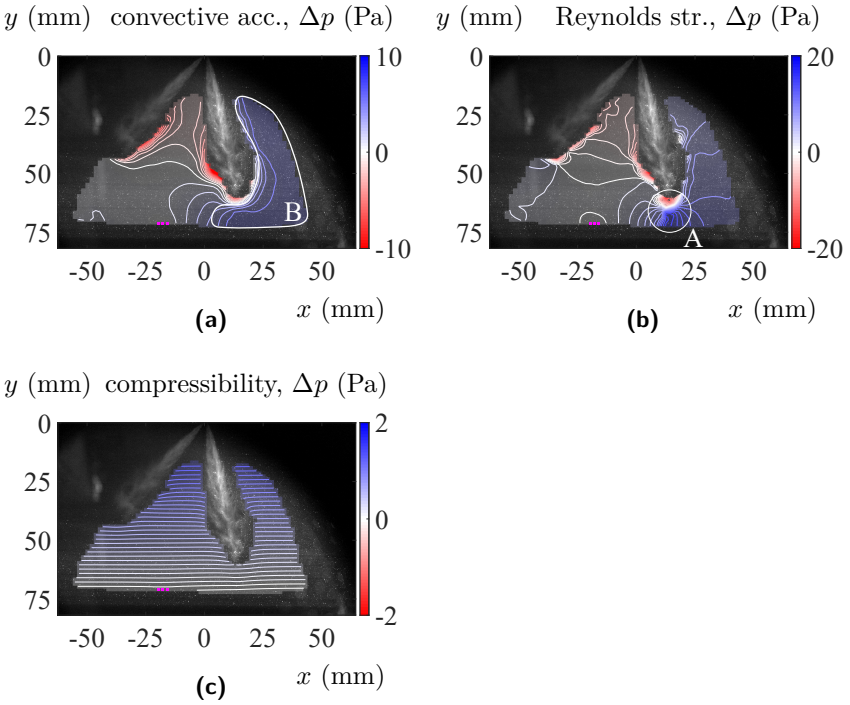

Figure 6.12: Sensitivity analysis [50] showing the influence of the convective acceleration, the Reynolds stresses and the compressibility on the pressure evaluation of the spray-induced flow. Comparison between pressure fields based on a full modelling and a modelling where corresponding terms or physics are omitted: (a) convective acceleration, (b) Reynolds stresses, (c) compressibility. Dirichlet Boundary nodes are marked with magenta color.

opens up the possibility of gaining previously hidden information about spray-induced flow, such as pressure potentials and forces. This now accessible information, in conjunction with existing quantities such as velocity, is expected to be key for the study of spray transport, momentum exchange and yet undisclosed mechanisms such as jet-to-jet interaction and spray contraction.
Considering the challenging conditions of spray-induced flow measurement, the success in pressure evaluation is attributed to a large extent to the proposed method of velocimetry-based pressure evaluation using URANS and ensemble averaging. Due to its high robustness to random errors from the PIV evaluation and other sources of error, the statistical approach demonstrated a good level of accuracy and reliability. The approach is well suited for experiments with inherent low signal-to-noise ratios such as the measurement of spray-induced flow. The uncertainty analysis has demonstrated good convergence for a reasonable number of measurement samples ($N \approx 50$). The pressure evaluation and methodology were successfully validated by the results of the comparative pressure sensor measurement. As a sequence of high and low pressures, the characteristics of displacement, entrainment and subsequent wake flow are well reproduced qualitatively and quantitatively.
Pivotal information on the quality and propagation of error were obtained by the uncertainty analysis of the pressure evaluation. While the ensemble-averaged velocity converges to the desired mean value with increasing number of measurement samples, the Reynolds stresses are subject to undesirable contributions of random errors and injection stochastics, which can be partly corrected by the knowledge of the magnitude of the random errors to achieve a more accurate estimate. The correction of the Reynolds normal stresses by the standard deviation of the instantaneous velocities was shown to be a viable measure to minimise the undesired contribution of random errors from PIV evaluation. To increase the quality of the pressure evaluation, an accurate and comprehensive quantification of the uncertainty is therefore desirable. The development and improvement of methods for the quantification of uncertainty in PIV evaluation can thus make an important contribution to this. Overall, the contributions of random errors and injection stochastics might lead to an overestimation of the Reynolds normal stresses and, in the case of correlated errors, also of the Reynolds shear stresses. In general, however, the Reynolds stresses are usually underestimated as the spatial and temporal resolution typically

does not resolve all small-scale structures and frequencies of turbulent flow, as was confirmed by the pressure sensor measurement.
The uncertainties of the ensemble-averaged pressures proved to be strongly dependent on the definition of the boundary conditions. Starting from the Dirichlet boundary nodes, the uncertainties accumulate over the domain of evaluation and reach the largest values in the most distant areas. To limit the accumulation of uncertainties and errors, the definition of several spatially distributed Dirichlet boundary conditions is advisable if reliable information are available. It should be noted that the definition of Dirichlet boundary conditions has to be chosen carefully, as inaccurate values introduce a systematic error to the pressure field.
The results of the scale and sensitivity analysis justify a simplification of the governing equations for pressure evaluation of spray-induced flow. The effect of viscosity and gravity are identified as negligible as their scales are at least three orders of magnitude smaller than the pressure gradient in the relevant areas of spray-induced flow. In case of low mass and heat transfer, the spray-surrounding gas flow can be further considered as incompressible. The pressure gradient is mainly described by the contributions of local acceleration, convective acceleration and Reynolds stresses. As such, the accordingly simplified versions of the URANS and divergence equations are as follows [50]:

Momentum equations:

$$\frac{\partial \overline{p}}{\partial x_i} = -\rho \frac{\mathrm{D}\overline{u}_i}{\mathrm{D}t} - \frac{\partial}{\partial x_j}\left(\rho \overline{u_i' u_j'}\right) \tag{6.1}$$

Divergence (general case):

$$\frac{\partial^2 \overline{p}}{\partial x_i \partial x_i} = -\rho \frac{\partial}{\partial x_i}\left(\overline{u}_j \frac{\overline{u}_i}{\partial x_j}\right) - \rho \frac{\partial^2 \left(\overline{u_i' u_j'}\right)}{\partial x_i \partial x_j} \tag{6.2}$$

Divergence (in-plane):

$$\frac{\partial^2 \overline{p}}{\partial x_1^2} + \frac{\partial^2 \overline{p}}{\partial x_2^2} = -\rho \left[\frac{\partial}{\partial x_1}\left(\frac{\partial \overline{u}_1}{\partial t} + \overline{u}_j \frac{\partial \overline{u}_2}{\partial x_j}\right) + \frac{\partial}{\partial x_2}\left(\frac{\partial \overline{u}_2}{\partial t} + \overline{u}_j \frac{\partial \overline{u}_2}{\partial x_j}\right)\right] - \frac{\partial^2 \left(\rho \overline{u_1' u_j'}\right)}{\partial x_1 \partial x_j} - \frac{\partial^2 \left(\rho \overline{u_2' u_j'}\right)}{\partial x_2 \partial x_j}. \tag{6.3}$$

The equations no longer carry mixed or third order partial derivatives. This simplifies the system of equations considerably. The need for high spatial resolution is eased to some extent. To obtain a rough estimation of the pressure field or to minimise potential errors, the omission of the Reynolds stresses and in some cases even the local acceleration is conceivable.
The excellent results of the pressure evaluation motivate a broad application of the presented methodology of velocimetry-based pressure evaluation for the analysis of spray-induced flows. Due to its particular robustness, flexibility and accuracy, the statistical approach is well-suited for the investigation of complex flows and challenging mechanism such as the phenomena of jet-to-jet interaction and spray contraction. Based on the statistical approach, extensive investigations on the spray transport of GDI sprays are carried out in the following chapters.

7 Spray-gas interaction

In the present chapter, the methodology of pressure evaluation of spray-induced flow is used to investigate the spray transport of a single-hole GDI spray for different operating conditions in order to gain valuable insights into the interrelation between spray formation, momentum exchange and macroscopic spray properties such as penetration length and spray expansion. The influence of key injection parameters are studied including injection pressure, fuel temperature, ambient gas pressure/density and flash-boiling atomisation. The study was published in Kling *et al.* [61].

7.1 Experimental procedure, parameter space and data processing

"To prevent adverse jet-to-jet influence, a spray generated by an axisymmetric single-hole injector and centrally oriented spray targeting is considered. n-Heptane as fuel is supplied under injection pressures in the range of 100 bar $\leq p_{inj} \leq$ 250 bar at various fuel temperatures 25°C $\leq T_{fuel} \leq$ 120°C into the optically accessible pressure chamber at constant gas temperature T_∞ = 25°C and 0.4 bar $\leq p_\infty \leq$ 3.0 bar chamber pressure. The corresponding gas density ρ_∞ is determined from the ideal gas equation $p_\infty/\rho_\infty = RT_\infty$, where R is the specific gas constant. This parameter space is chosen to allow particular focus on the process of flash-boiling atomisation during GDI. Flash-boiling corresponds to an isothermal depressurisation. Its occurrence and strength can be determined from positive Jakob numbers $Ja = \rho_l c_{p,l} T_{fuel} \left(p_v - p_\infty\right) / \left(\rho_v h\right)^2$ [63], where Ja describes the ratio between sensible and latent heat, with $\rho_l, c_{p,l}, h, p_v, \rho_v$ being the liquid density, liquid heat capacity, latent heat, vapour pressure and vapour density, respectively.

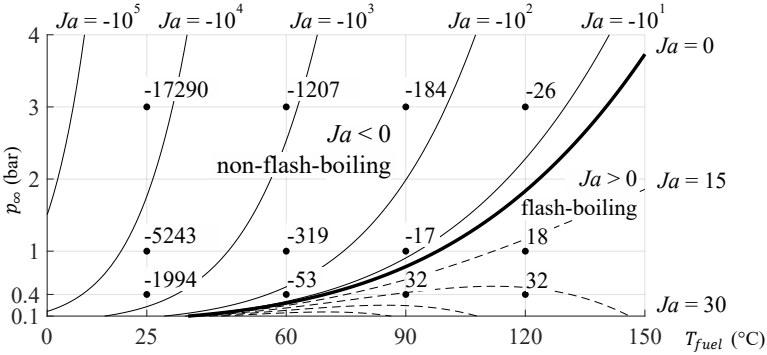

Figure 7.1: "Jakob number Ja as a function of the parameter space p_∞ and T_{fuel}. Investigated parameter combinations are added with black markers. The thick black line separates flash-boiling ($Ja > 0$, —) and non-flash-boiling ($Ja < 0$, - -) regions in the diagram. Note that the dashed and solid lines are used throughout the manuscript to indicate whether or not flash-boiling occurs." [61]

Figure 7.1 shows the Jakob number Ja as function of the ambient pressure and fuel temperature in a $T_{fuel} - p_\infty$ diagram, in which the parameter combinations of the present study are added as black markers. Both flash-boiling ($Ja > 0$) and non-flash-boiling ($Ja < 0$) operating points are considered. Since the injection pressure has only negligible influence on the Jakob number, this diagram holds true for all tested p_{inj}. The required information on the vapour pressure p_v was determined based on the experimental data obtained by Williamham *et al.* [133] for 25°C $< T_{fuel} <$ 100°C, and Ewing & Sanchez Ochoa [134] for 100°C $< T_{fuel} <$ 150°C, while the latent heat h was derived from the data of Majer [135]." [61]

"The desired unsteady gas-velocity information was recorded with time-resolved stereoscopic particle image velocimetry (stereo-PIV), where fluorescent tracers (propylene-carbonate/DCM solution $\approx 1\mu$m) were illuminated by a *Photonics DM100-532* double-cavity Nd:YAG laser. The emitted light was recorded at $f_{acq} = 8$ kHz double-frame rate (interframing time $\mathrm{d}t_{PIV} = 10$ μs) with two *Phantom V1612* high-speed cameras (1280 × 800 px, 12-bit depth) under Scheimpflug conditions both equipped with *Tokina AT-X M100 AF Pro D* lenses (100 mm focal length) and

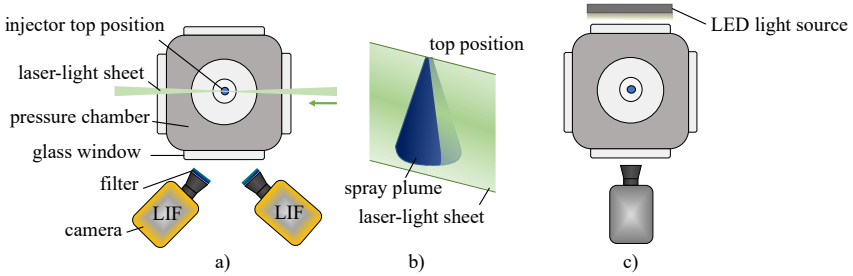

Figure 7.2: "Top (a) and side (b) view of the stereoscopic PIV setup and the orientation of the investigated single-hole spray; (c) shadowgraphy setup." [61]

OD6 long-pass filters (cut-off wavelength 600 nm). Laser-sheet and camera orientations relative to the spray plume are illustrated in Figure 7.2. The recorded field of view spans 106×80 mm^2 and was processed with a multi grid multi pass algorithm; spurious vectors were eliminated by a normalised median filter (3×3). To ensure statistical significance, 50 experiments per parameter setting were conducted and subsequently ensemble-averaged to obtain statistical velocity quantities.

Since precise knowledge of the spray-tip location is of utmost importance for the characterisation of spray transport, further time-resolved shadowgraphy experiments ($f_{acq} = 25$ kHz, FOV of 95×85 mm^2) were conducted with identical camera equipment and a *Phlox* LED light source. To minimise the effect of shot-to-shot deviations, the spray-tip penetrations were likewise determined on the grounds of 50 ensemble-averaged injection events. The spray-tip location was determined from a threshold-based localisation of the lowest bright pixel. To avoid spurious data processing, raw-image noise was removed by means of a sliding minimum filter. Remaining frame-to-frame scatter was removed with a least-square estimator for clarity.

The pressure evaluation approach for this statistically unsteady flow is based on the evaluation of the divergence of the incompressible Unsteady Reynolds-Averaged Navier-Stokes (URANS) equations [50]

$$\frac{\partial \overline{p}}{\partial x_i} = -\rho \left(\frac{\partial \overline{u}_i}{\partial t} + \overline{u}_j \frac{\partial \overline{u}_i}{\partial x_j} \right) - \frac{\partial}{\partial x_j} \left(\rho \overline{u_i' u_j'} \right) [...]. \tag{7.1}$$

According to the findings on pressure evaluation of spray-induced flow [50] [(see Chapter 6)], the spray surrounding gas flow is considered incompressible. In the area of pressure evaluation, mass and heat transfer are assumed to be minimal, as the vapour phase is confined to a small area close to the spray [136, 137], especially at the early stage of spray formation of a GDI single-hole spray. Accordingly, a constant gas composition consisting of nitrogen is assumed. Furthermore, the effects of viscosity and gravity are considered negligible, as they are of much smaller magnitude compared to local and convective acceleration. The processing approach further takes advantage of the symmetrical character of the single-hole spray event, which reduces the experimental effort to evaluate Equation 7.1 in a single measurement plane aligned with the spray axis. The resulting divergence information of Equation 7.1 is then converted to pressure fields by means of Neumann boundary conditions and a single Dirichlet boundary condition, where the ambient gas conditions is chosen for the latter to prescribe the overall pressure level of the determined distributions." [61]

7.2 Results and Discussion

"Since the momentum transfer from the spray to its gas environment can be identified from the resulting pressure distributions via momentum conservation, both measured velocities and derived pressure distributions are superimposed to the raw images of the recorded GDI events for all discussed results. Furthermore, the complementary shadowgraphs reveal the desired information on spray-tip propagation, which bridges the gap between spray transport and momentum exchange. Note that only every tenth tip-location estimate is indicated with a marker in all spray-tip diagrams of this section for clarity. The investigated parameters partly induce strongly coupled effects, mostly due to flash-boiling atomisation, which is facilitated by both low ambient pressures and high fuel pressures, but also due to material properties specified by Weber and Ohnesorge numbers. In a first step, therefore, the results are contrasted for occurrence and absence of flash-boiling atomisation. Subsequently, the influence of the individual degrees of freedom (p_{inj}, T_{fuel}, p_{∞}) on the spray properties are further elaborated separately." [61]

7.2.1 Flash-boiling and fuel temperature

"The effect of flash-boiling atomisation is studied for different levels of superheat. Since variations of injection and ambient gas pressure inherently imply modifications of the gas density and/or mass flow, the level of superheat is solely controlled by the fuel temperature, while all other parameters remain constant. To emphasise the effect of flash-boiling atomisation, both flash-boiling and non-flash-boiling operating conditions are contrasted. The examined operating points are at $p_{inj} = 200$ bar and $p_{\infty} = 0.4$ bar for $T_{fuel} = 25, 60, 90, 120°\mathrm{C}$, corresponding to the lowest line of markers in Figure 7.1.

Figure 7.3 shows the temporal evolution of the evaluated spray tip penetrations for various operating conditions. It becomes obvious from the curves that increasing fuel temperatures lead to gradually diminished spray tip velocities. Note that a considerably slower spray tip velocity is revealed under flash-boiling conditions at $T_{fuel} = 90°\mathrm{C}$ and $T_{fuel} = 120°\mathrm{C}$, since a spray deceleration occurs immediately after the start of injection (SOI) and gradually subsides over the event of spray propagation. In contrast, there is nearly no spray-tip deceleration under non-flash-boiling conditions at $T_{fuel} = 25°\mathrm{C}$ and $T_{fuel} = 60°\mathrm{C}$, which leads to near constant spray-tip velocity. The slight decrease of spray tip velocity from $T_{fuel} = 25°\mathrm{C}$ to $T_{fuel} = 60°\mathrm{C}$ is the result of an increased liquid disintegration due to lower Ohnesorge number Oh and higher Weber number We_l at $T_{fuel} = 60°\mathrm{C}$.

The corresponding pressure distributions around the spray are shown in Figure 7.4, which clearly reveal a peak pressure in front of the spray cone. Interestingly, similar to the spray tip penetration, the pressure distributions show higher differential pressures for increasing levels of superheat/fuel temperature. The differential pressures range in the order of 10 Pa at $T_{fuel} = 25°\mathrm{C}$ ($Ja = -309$) and 100 Pa at $T_{fuel} = 120°\mathrm{C}$ ($Ja = 32$). Under non-flash-boiling conditions at $T_{fuel} = 25°\mathrm{C}$ ($Ja = -1933$) and $T_{fuel} = 60°\mathrm{C}$ ($Ja = -53$), the pressure fields, furthermore, indicate a comparatively weak momentum exchange. The sprays remain rather stringy, experiencing no considerable expansion.

Under flash-boiling conditions, however, the bushy spray envelope leads to significantly higher peak pressures in front of the spray tip. Recall from Sher *et al.* [74] that – in contrast to liquid disintegration by mechanical means – flash-boiling atomisation is characterised by smaller mean and more uniformly

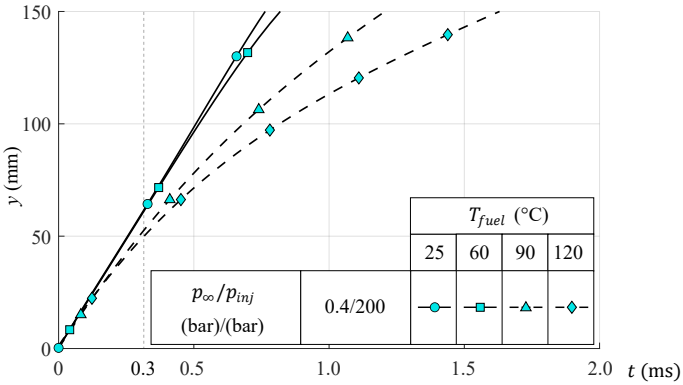

Figure 7.3: "Spray tip penetration for different levels of superheat and fuel temperatures. Dashed lines indicate flash-boiling atomisation in accordance with Figure 7.1." [61]

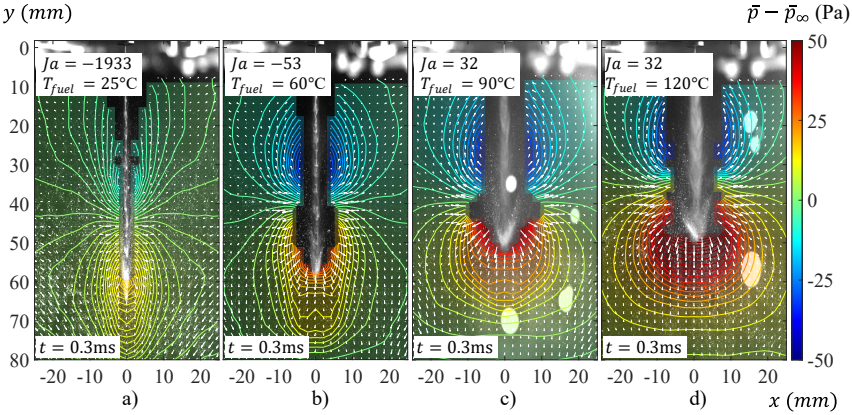

Figure 7.4: "Effect of fuel temperature and flash-boiling atomisation. The contour plot and vector field shows pressures and velocities. Time $t = 0.3$ ms after SOI. Conditions: $p_\infty = 0.4$ bar, $p_{inj} = 200$ bar. PIV raw images provided in the background for orientation purposes. Note that the exact spray location might deviate from the evaluated ensemble." [61]

distributed droplet diameters. Consequently, the momentum exchange is typically considered to intensify as a result of increased spray gas interface and area of drag as e.g. hypothesised by Ming *et al.* [27]. As such, the observed high peak pressures in Figure 7.4 retroactively prove these earlier hypotheses on an increased momentum transfer under flash-boiling conditions and furthermore explain the reduced spray tip propagation speed." [61]

7.2.2 Ambient gas pressure and corresponding density

"Major processes in spray formation, such as flash-boiling atomisation and aerodynamic forces, are also closely related to the ambient gas pressure and the corresponding density, which determines the intensity of nucleation and thus the strength of liquid disintegration. As above, the impact of gas pressure and related density on momentum transfer and spray propagation is contrasted for presence and absence of flash-boiling. In Figure 7.5, the courses of spray tip penetration are shown at $p_{inj} = 250$ bar and $T_{fuel} = 25°C$, 120°C for varying ambient gas pressures $p_{\infty} = 0.4$ bar, 1.0 bar and 3.0 bar. Under non-flash-boiling conditions the spray propagation slows down with higher ambient gas pressure, which is most obvious from the gradually decreasing slopes for $T_{fuel} = 25°C$. The elevated ambient gas pressures are furthermore found to result in higher differential pressures and, therefore, momentum exchange as shown in Figure 7.6, while spray formation and corresponding expansion is only mildly affected by the pressure variation. Since the elevated pressures in turn lead to increased density levels, this observation consequently also demonstrates the influence on the aerodynamic forces via Stokes' drag as an additional spray-tip deceleration mechanism.
For the investigated parameter range, the drag-driven tip-speed reduction over propagation time is in contrast to the near-constant yet slower propagation characteristics of flash-boiling atomisation. This difference is obvious from the direct comparison of the determined propagation curves for $T_{fuel} = 90°C$; see Figure 7.5. Further evidence of the different mechanisms on the resulting momentum exchange is provided by the pressure distribution around the respective spray plumes in Figure 7.7. The strong atomisation and immediate expansion of the spray under flash-boiling conditions leads to significant momentum exchange due to steep pressure gradients in proximity of the tip at an early stage of spray formation ($t = 0.2$ ms), which is diminished for later stages ($t = 0.4$ ms);

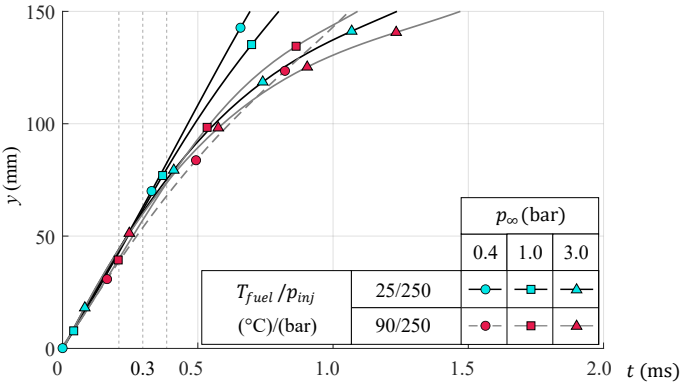

Figure 7.5: "Spray tip penetration for different ambient gas pressures. Dashed lines indicate flash-boiling atomisation in accordance with Figure 7.1." [61]

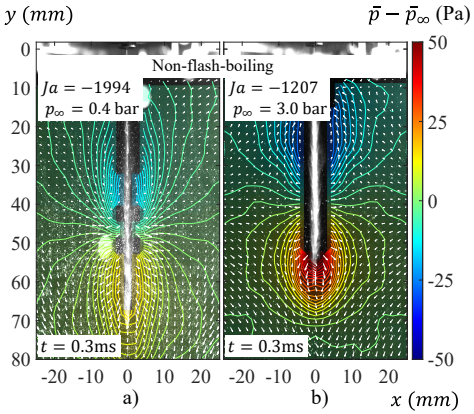

Figure 7.6: "Effect of the ambient gas pressure. Time $t = 0.3$ ms after SOI. The contour plot and vector field shows pressures and velocities. Conditions: $p_{inj} = 250$ bar, $T_{fuel} = 25°C$. PIV raw images provided in the background for orientation purposes. Note that the exact spray location might deviate from the evaluated ensemble." [61]

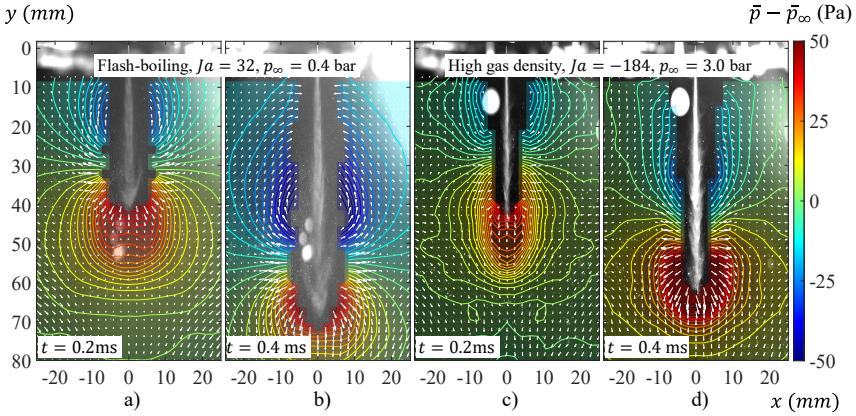

Figure 7.7: "Comparison between the effects of flash-boiling atomisation and increased ambient gas pressure. The contour plot and vector field shows pressures and velocities. Times $t = 0.2$ ms and $t = 0.4$ ms after SOI. Conditions: $p_{inj} = 250$ bar, $T_{fuel} = 90°C$. PIV raw images provided in the background for orientation purposes. Note that the exact spray location might deviate from the evaluated ensemble." [61]

cp. Figures 7.7 (a) and (b). Under non-flash-boiling conditions, in contrast, a significant increase of momentum exchange over time is observed, where the pressure gradients in tip vicinity increase from $t = 0.2$ ms to $t = 0.4$ ms; cp. Figures 7.7 (c) and (d). The later peak of momentum exchange is attributed to a less intense atomisation by mechanical means and thus a weaker and more gradual expansion of the spray. The spray is rather stringy compared to the more bushy spray in case of flash-boiling atomisation, where the larger cross-section of the latter implies increased amounts of drag, thus momentum exchange.

The varying spray tip velocities at the later stage of spray formation reveals the impact of higher ambient gas pressures/densities on the spray propagation deceleration. Here, the effect of a higher ambient gas density seems to outweigh the stronger atomisation and spray expansion by flash-boiling. However, it should be noted that the reported observation does not universally hold for all types of spray, as the result also depends on additional factors such as the quality of atomisation and ambient gas flow,

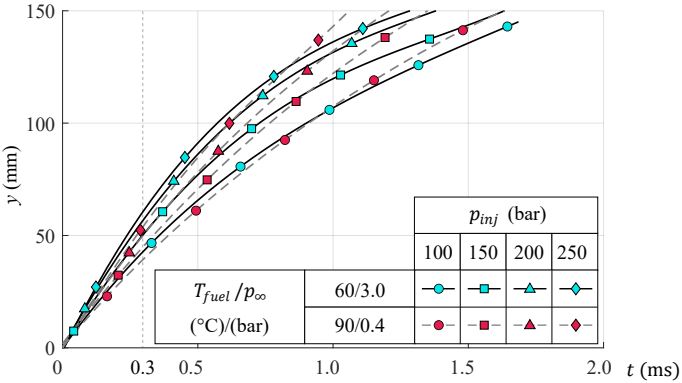

Figure 7.8: "Spray tip penetration for different injection pressures. Dashed lines indicate flash-boiling atomisation in accordance with Figure 7.1." [61]

for instance. A counterexample would be a very stringy spray with low mechanically induced atomisation and spray expansion, where the effect of a higher ambient gas density becomes less dominant as the momentum exchange is diminished." [61]

7.2.3 Injection pressure

"Even though the injection pressure p_{inj} has nearly no influence on flash-boiling effects, the precise controllability of this quantity for GDI renders p_{inj} an operating parameter of major importance to adjust mass flow and initial spray momentum, thus the processes of atomisation and spray-gas interaction. Figure 7.8 shows the temporal evolution of spray tip penetration for varying injection pressures at flash-boiling ($Ja = 32$) and non-flash-boiling conditions ($Ja = -26$). In both regimes, the spray tip velocities experience a more pronounced deceleration at higher injection pressures. As such, the propagation curves of different tip speeds (at least partly) align towards similar slopes for later propagation stages – especially for increased drag at higher ambient pressures.
Figure 7.9 shows the corresponding pressure fields and spray images for $p_{inj} = 150$ bar and $p_{inj} = 250$ bar, which indicate a larger momentum

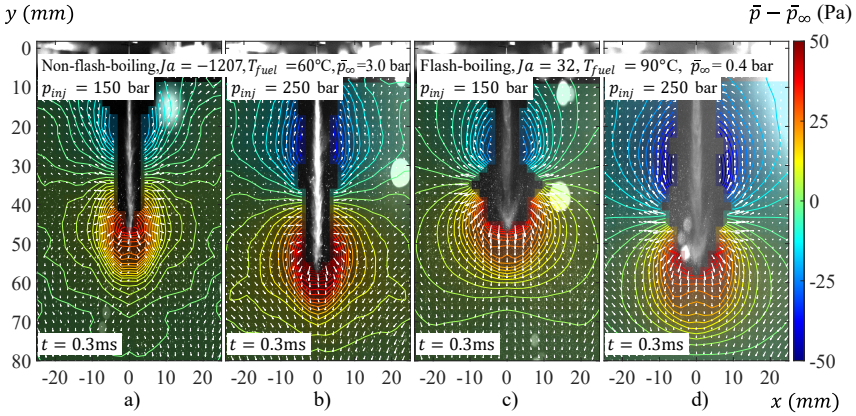

Figure 7.9: "Effect of injection pressure p_∞ on spray transport and momentum exchange for $T_{fuel} = 60°C$, $p_\infty = 3.0$ bar and $T_{fuel} = 90°C$, $p_\infty = 0.4$ bar at time $t = 0.3$ ms after SOI. The contour plot and vector field shows pressures and velocities. PIV raw images provided in the background for orientation purposes. Note that the exact spray location might deviate from the evaluated ensemble." [61]

exchange at higher injection pressures, while the spray images suggest a stronger expansion of the spray (cp. Figure 7.8). The observed increase in momentum exchange mainly results from the following two effects. First, at higher mass flow rates, the momentum exchange increases with higher relative velocities ($F_{drag} \sim v_{rel}^2$). Second, as the atomisation intensifies with larger Re_l and We_l numbers, the aerodynamic forces enhance due to increased area of drag by both smaller droplet sizes and larger spray expansion. Consequently, the influence of the injection pressure on the resulting spray transport increases with rising chamber pressure levels due to the above-discussed correspondingly increased drag effects." [61]

7.3 Concluding remarks

"The momentum exchange between spray and ambient gas flow of GDI jets is identified for different operating conditions, where various formerly

hidden insights into the complex interplay of the contributors involved in spray transport are uncovered. Most importantly, the present investigation provides a deeper insight into frequently reported observation of the direct cause-effect relation between thermodynamic operating conditions and the resulting spray-penetration properties (see e.g. [12, 14, 28, 32]). Particularly, the application of the recently introduced URANS-based pressure determination approach [50] on the unsteady flow fields reveals the spatio-temporal pressure distributions, which in turn allows the analysis of the injection event on the grounds of the distributed momentum balance for even small changes in injection pressure, fuel temperature, ambient gas density and quality of atomisation.

It is found that the momentum exchange increases with larger spray-gas interface, spray expansion, greater relative velocity, higher ambient gas density, and fuel temperature, which is known to have immediate implications for surface tension and liquid viscosity. Furthermore, the salient effect of flash-boiling atomisation on the spray-gas interplay was demonstrated to rely directly on a remarkably strong momentum exchange resulting from the expedited spray breakup into small droplets and correspondingly impulsive expansion of the spray. This result is an important insight even beyond the parameter range of the present investigation, since it quantitatively demonstrates the relevance of small droplets for the momentum transfer.

It has to be, therefore, concluded from the above insight that even mechanically induced spray disintegration with accordingly vast amounts of small droplets will lead to an enhanced level of momentum transfer to the gas environment. This conclusion in turn indicates the great potential in influencing and controlling spray transport by designing sprays with enhanced mechanical spray disintegration. It is also hypothesised in this context that similar levels of momentum-exchange augmentation might also be achievable through specific changes in internal nozzle design by enhancing the degree of turbulence and spray expansion, which is, however, beyond the scope of the present study.

As a technical note, the applied URANS-based approach for velocity-based pressure estimation turned out to be particularly applicable for the investigation of spray-induced flows, due to its statistical character, and corresponding robustness and accuracy. The derived results from this approach render the expansion of the covered parameter range to more sophisticated multi-hole sprays promising, since the applied approach is

hypothesised to contribute to a deeper insight into complex mechanisms such as jet-to-jet interaction and spray contraction.
On a final remark, both the applied processing strategies and derived conclusions of the present investigation are considered valuable contributions towards more advanced design of spray transport phenomena beyond GDI optimization only. It is rather foreseen that the robustness and universality of the outlined approach might provide a beneficial contribution to a wide range of applications, such as the injection design for alternative fuels like biofuels or e-Fuels, for instance." [61]

8 Multi-hole spray formation

In contrast to single-hole sprays, a major effect in the spray transport of multi-hole sprays is due to the interaction of individual spray plumes. Under certain conditions, the so-called jet-to-jet interaction leads to significant changes in the formation and transport of spray, starting with a rather moderate change in the spray plume trajectories up to a complete contraction to a unified jet.

In previous studies, the influence of operating conditions (fuel and ambient gas pressure/temperature/density, fuel type, injection duration), spray layout (number/arrangement of spray holes) and injector design on macroscopic spray characteristics such as spray penetration, spray cone angle and entrainment flow were widely examined [28–36]. However, the research has been largely limited to a phenomenological quantification and analysis. Certain theories have been proposed, but in many cases they have not yet been experimentally validated, nor have the underlying cause-effect relationships been fully understood.

In terms of spray contraction, a common theory proposed by experimental observations and numerical studies [39–42] is the presence of a local pressure minimum in the central area of the spray in between the spray plumes. It is hypothesised that the supposed pressure minimum is responsible for the attraction of the spray. Regarding the formation of the pressure minimum, different explanatory approaches exist. Some authors claim that the pressure minimum is due to the evaporation of spray [35]. Others assume that the pressure minimum is formed by the lack of a compensating ambient gas flow between the inner and outer spray area as a result of the spray layout (sealing effect) [39].

To assess the mechanism of jet-to-jet interaction and spray contraction, sound information on the momentum exchange between spray and ambient gas flow is required. However, apart from CFD, no experimental data is yet available on the central region and spray plume interspaces, especially close to the injector nozzle, where spray contraction largely takes place.

In the present chapter, the spray transport and jet-to-jet interaction of GDI multi-hole sprays are investigated by means of pressure evaluation of spray-induced flow. The cause-effect relationship between spray transport, momentum exchange and ambient gas flow is studied for varying operating conditions and spray layouts.

8.1 Spray transport of a contracting multi-hole spray

In this section, the spray transport of a GDI multi-hole spray is investigated for different levels of superheat, injection pressure, fuel temperature and ambient gas pressure/density. The investigation examines the transition from non-contracting to contracting spray and its effect on spray formation and spray penetration.

8.1.1 Experimental setup and evaluation

The investigation considers a GDI 6-hole spray with an axisimmetric spray layout and targeting, as shown in Figure 8.1, that is typically used for a combustion process with a central injector position. The spray transport is studied for characteristic engine conditions ranging from 150 bar $\leq p_{inj} \leq$ 250 bar injection pressure, 0.4 bar $\leq p_{\infty} \leq$ 2.0 bar ambient gas pressure and 25°C $\leq T_{fuel} \leq$ 120°C fuel temperature.
The experimental setup, measurement and evaluation correspond to the procedure in Chapter 7. While the desired velocity field information were acquired with stereo-PIV measurements ($f_{acq} = 10$ kHz, $\mathrm{d}t_{PIV} = 10\ \mu s$, $FOV = 160 \times 140$ mm^2), the spray tip penetration were evaluated with processed shadowgraphy measurements ($f_{acq} = 25$ kHz, $FOV = 116 \times 145$ mm^2). To provide statistical significance and minimise the effect of shot-to-shot variation, the computation of the statistical quantities and the processing of the shadowgraphy measurements were conducted using an ensemble average of 50 measurement samples.

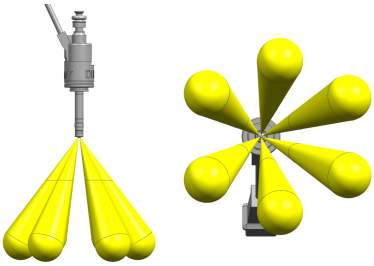

Figure 8.1: Spray layout and targeting (symmetric) of the 6-hole GDI spray under investigation.

8.1.2 Results

In Figure 8.2, the evaluated spray tip penetration of the GDI 6-hole spray is shown for varying operating conditions as a function of time. In contrast to the propagation of a single jet (see Chapter 7), the spray propagation of the multi-hole spray shows a discontinuous course with a sequence of deceleration, acceleration and deceleration at flash-boiling conditions ($p_\infty = 0.4$ bar, $T_{fuel} = 120°\text{C}$ and $p_{inj} = 150,250$ bar, $Ja = 32$), but also at non-flash-boiling conditions ($p_\infty = 2.0$ bar and $T_{fuel} = 120°\text{C}$, $Ja = -4$). As shown in Figure 8.3, the discontinuous course is related to the contraction of the spray. During the transition from non-contracting to contracting spray, the propagation changes from individual spray plumes to a unified jet. Depending on the degree of spray contraction, a distinction can be made between non-contracting, gradually contracting and instantly contracting sprays (see figures 8.3a – 8.3c). While the spray tip velocities of the non-contracting and instantly contracting sprays are characterised by a monotonous decrease similar to that one of a single jet (see Chapter 7), the discontinuous course of the gradually contracting spray is attributed to the passing of the original spray plumes by the faster propagating contracted jet, which experiences less deceleration due to a smaller area of drag, lower relative velocities (slipstream effect) and higher inertia (liquid mass per volume).
With regard to injection pressure, fuel temperature and ambient gas pressure the same observations apply for the propagation of the spray plumes

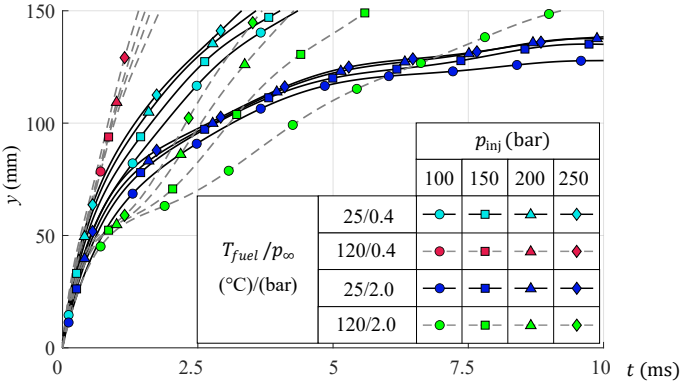

Figure 8.2: Spray tip penetration of the GDI 6-hole spray for different ambient gas pressures p_∞, fuel temperatures T_{fuel} and injection pressures p_{inj}.

and the contracted jet as for the single-hole spray in Chapter 7. While there is a faster propagation at higher injection pressures, fuel temperatures and lower ambient gas pressures/densities as shown in Figure 8.2, the extent of spray contraction intensifies with higher levels of superheat, injection pressure and fuel temperature. The results indicate a correlation between spray contraction and atomisation.

In figures 8.4 – 8.7, the pressure and velocity fields of a non-contracting, gradually contracting and two instantly contracting sprays, one at low and one at high ambient gas pressure/density, are shown for consecutive times. In the case of the non-contracting spray, the momentum exchange between spray and ambient gas takes place through locally separated spray plumes over a comparatively large spatial volume. As shown in figures 8.4a and 8.4b, there is a visible separation of the respective high pressure regions at the displacement flows near the spray plume tips. Due to the spread of the spray plumes, the momentum exchange takes place over a larger volume of space. The effective inertia of the ambient gas flow increases, as more fluid is accelerated in contrast to a more compact or contracted spray. The spread of the spray largely reduces the effect of a slipstream. With increasing spray contraction, the proportion of the individually propagating spray plumes becomes successively smaller. As a result of the reduced area of drag, the lower effective inertia of the ambient gas flow

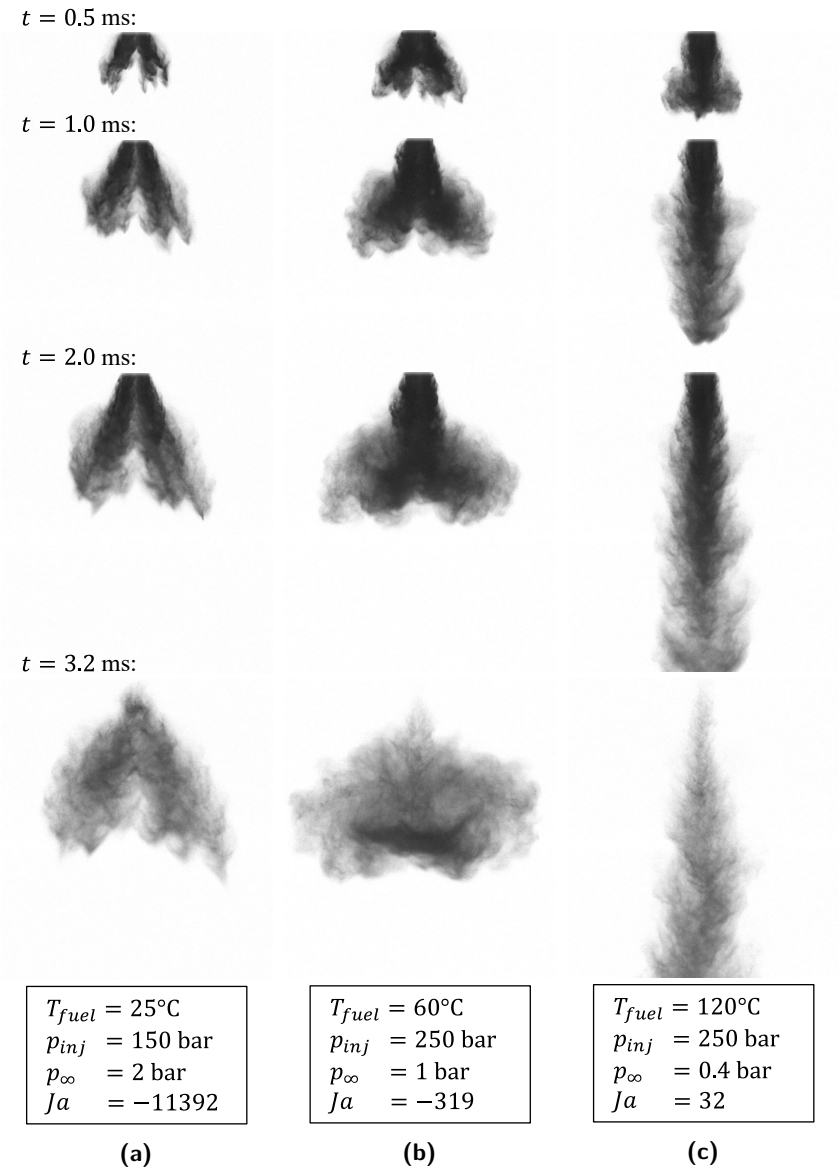

Figure 8.3: Transition from non-contracting to contracting spray. Sprays visualised by shadowgraphy images at consecutive times t after SOI.

and the increased slipstream effect, larger penetration lengths occur. Although there are significant differences in spray transport, the basic flow patterns of the spray-induced flows are similar. The pressure distributions and the spray transports indicate the formation of a vortex flow. The flow is characterised by a consistent structure of high pressures at the displacement and wake flow (after injection) and low pressures in the area of the gas entrainment and the vortex ring. The quality of spray transport and ambient gas flow largely depends on the inertias of the spray and the ambient gas flow. The inertias define whether and to what extent the spray transport converges to the ambient gas flow or vica versa. While at high gas densities, major proportions of the spray are entrapped within the vortex flow as shown in figures 8.5d and 8.6d for $p_{inj} = 250$ bar, $p_{\infty} = 1.0$ bar, $T_{fuel} = 60°C$ and $T_{fuel} = 90°C$, the spray propagates nearly unchecked with almost no alignment with the ambient gas flow at lower ambient gas densities as shown in Figure 8.7c for $p_{inj} = 250$ bar, $p_{\infty} = 0.4$ bar, $T_{fuel} = 120°C$. A comparison of both operating points is well suited to demonstrate the effect of spray and ambient gas inertias, as the level of momentum exchange is comparable. The effect of a higher ambient gas density is compensated by smaller droplet sizes due to flash-boiling atomisation at $p_{\infty} = 0.4$ bar and $T_{fuel} = 120°C$. This observation is in good agreement with the findings in Chapter 7.

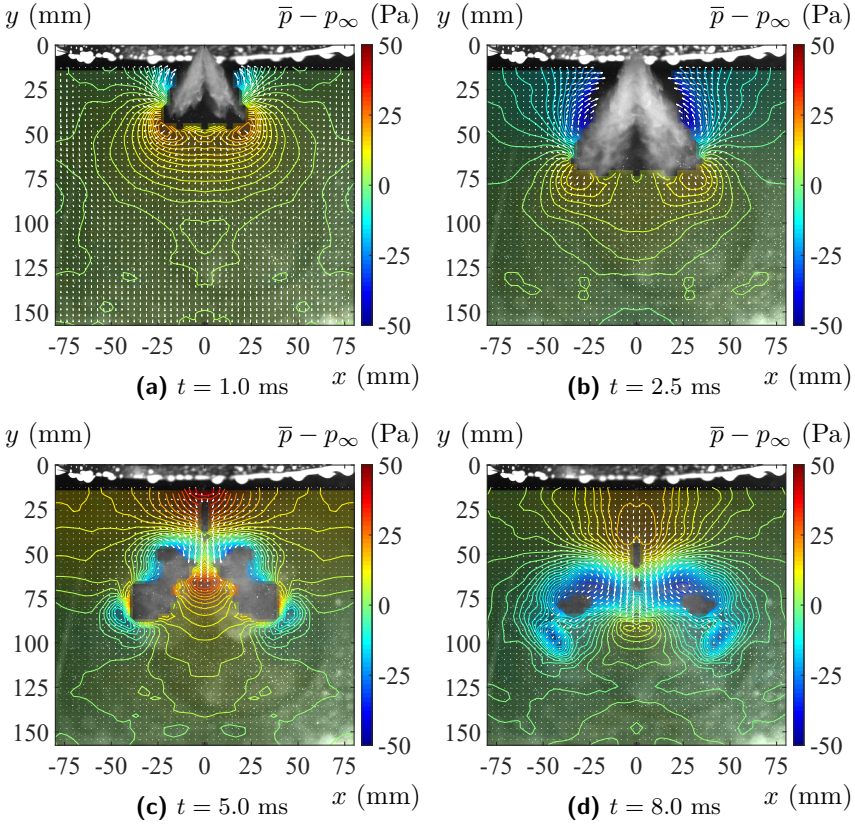

Figure 8.4: Non-contracting spray. Pressure and velocity fields at $p_{inj} = 150$ bar, $p_\infty = 2.0$ bar, $T_{fuel} = 25°\text{C}$ and $Ja = -11392$ for consecutive times t after SOI.

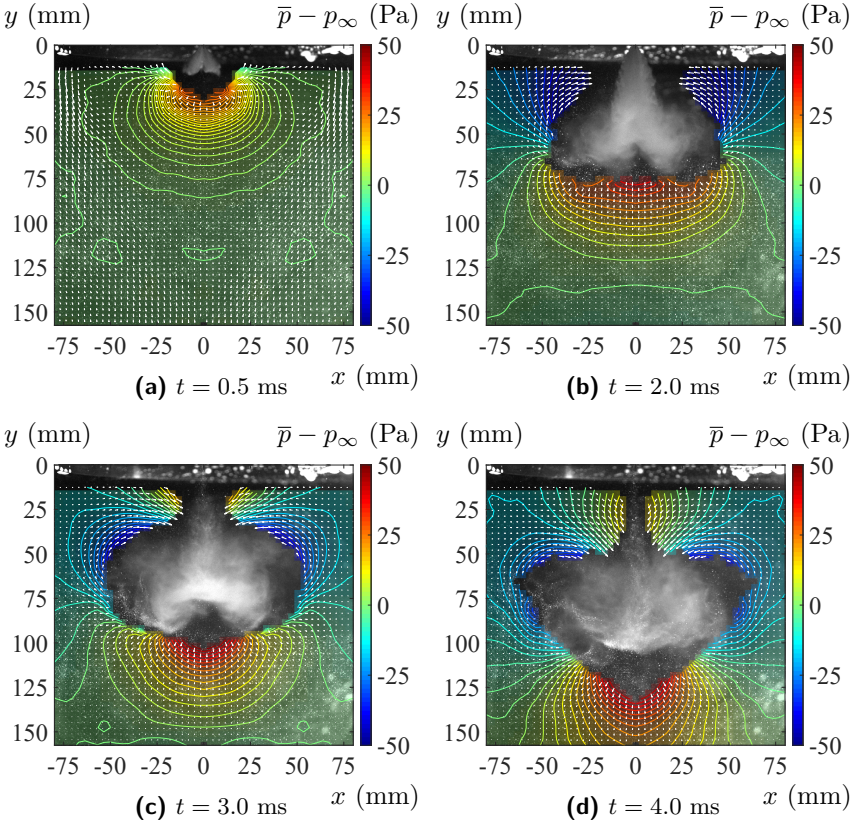

Figure 8.5: Gradually contracting spray. Pressure and velocity fields at $p_{inj} = 250$ bar, $p_\infty = 1.0$ bar, $T_{fuel} = 60°\text{C}$ and $Ja = -319$ for consecutive times t after SOI.

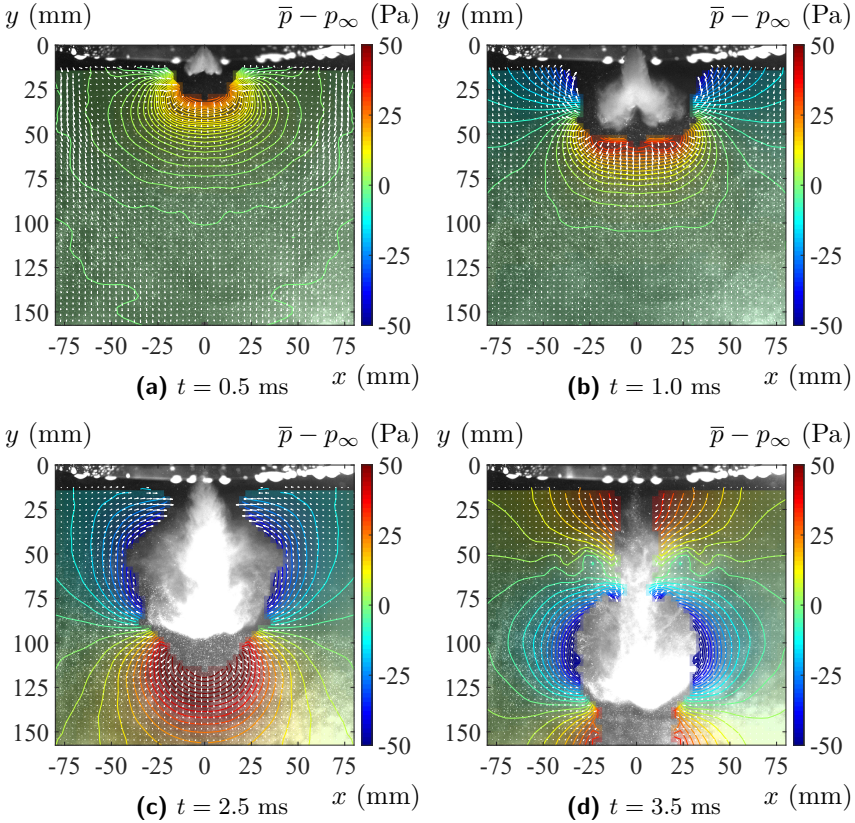

Figure 8.6: Instantly contracting spray. Pressure and velocity fields at $p_{inj} = 250$ bar, $p_\infty = 1.0$ bar, $T_{fuel} = 90°\text{C}$ and $Ja = -17$ for consecutive times t after SOI.

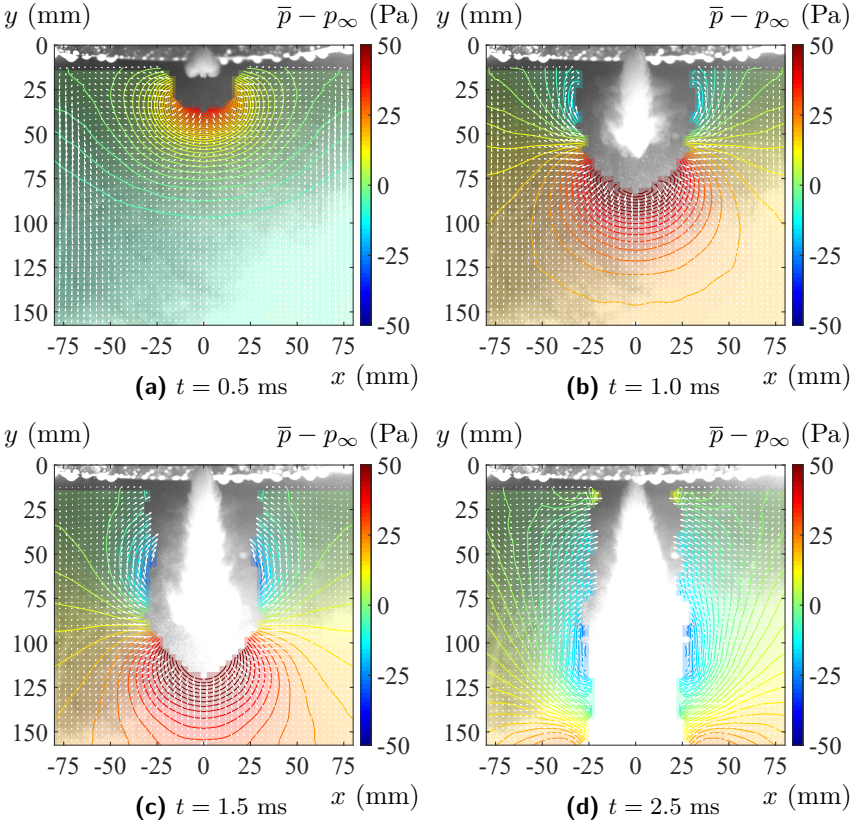

Figure 8.7: Instantly contracting spray. Pressure and velocity fields at $p_{inj} = 250$ bar, $p_\infty = 0.4$ bar, $T_{fuel} = 120°C$ and $Ja = 32$ for consecutive times t after SOI.

8.2 Spray contraction

In this section, the mechanism of jet-to-jet interaction and spray contraction is investigated by means of specially designed PIV measurements that allow for the evaluation of pivotal velocity and pressure field information in the central area of spray and spray plume interspaces of a multi-hole spray close to the injector nozzle. The information are used to analyse the effective net momentum acting on the individual spray plumes/jets and to identify the cause-effect relationships with respect to spray layout, targeting and operating conditions.

8.2.1 Experimental setup and evaluation

The spray-induced flow of three different spray layouts, including a conventional GDI 6-hole spray and two 3-hole sprays with improved optical accessibility, are investigated for flash-boiling and non-flash boiling conditions. To study the influence of targeting directions, an axisymmetric and a non-axisymmetric spray layout was chosen for the injector design of the 3-hole sprays. In Figure 8.8, the respective spray layouts and targetings are illustrated.
For the measurement of the spray-induced flow in the central area of the spray and spray plume interspaces, a bottom-up camera perspective along the spray axis towards the injector tip is used (see Figure 5.1). Such a velocimetry is particularly challenging, especially close to the injector nozzle. By the presence of spray, the optical access is markedly limited. In the course of injection, the propagation, expansion and potential contraction of the spray increasingly limits the optical access to both the centre and the spray plume interspaces. This limitation is further intensified by the oblique view of the stereoscopic setup, which requires a sufficient mutual camera angle for an accurate reconstruction of the particularly dominant out-of-plane velocity component. As a compromise between optical access and velocity reconstruction, a mutual camera angle of about $\alpha = 60°$ is chosen. The intersection of dense spray is followed by intense multi-scattering and quasi-volumetric illumination. Due to a small depth of correlation, the PIV evaluation is limited to a thin, planar domain (see Section 3.5).

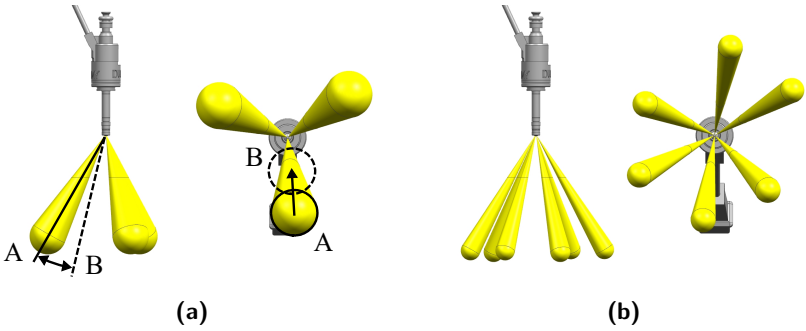

Figure 8.8: Spray layouts and targetings of the injector samples under investigation. a) 3-hole sprays: (A) axisymmetric spray, (B) non-axisymmetric spray, b) 6-hole spray.

To resolve small scale structures, such as spray plume interspaces, while covering a wide range of the flow field, the statistical approach based on URANS and ensemble averaging is fully exploited by reconstructing a detailed and large-scale velocity field based on several measurements with small FOVs at different in-plane measurement locations (variation in $x-z$-plane). For the investigation of the different spray layouts, the desired pressure fields were evaluated in planar domain at a distance of about 40 mm from the injector tip using a central differencing scheme to calculate the required out-of-plane gradients (y-direction). For this purpose, measurements were carried out at three different levels of depth including the main level at 40 mm distance and two further levels with a relative displacement of ± 5 mm. The spacing between the measurement levels corresponds to a size of about two to three interrogation windows. The statistical quantities were determined using an ensemble average of 30 measurement samples at each measurement location. Since the flow is highly transient and pressure evaluation of spray-induced flow aspires high temporal resolution (accuracy of local acceleration) [50], the PIV measurements were conducted with an acquisition frequency of $f_{acq} = 16$ kHz and an interframing time $\mathrm{d}t_{PIV} = 10\ \mu$s. As the occurring particle displacements are small with respect to the short interframing time, a PIV evaluation scheme of $(1+3,\ 2+4,\ 3+5, \ldots)$ was used. The evaluation of

the pressure fields was conducted according to the methodology presented in chapters 4 and 6.

8.2.2 Results

Figure 8.9 shows the pressure and velocity fields of the axisymmetric 3-hole spray at $p_{inj} = 250$ bar, $p_{\infty} = 1.0$ bar and $T_{fuel} = 25°C$ ($Ja = -5243$) for consecutive times. Starting with high pressures associated with the displacement flows at the spray plume tips (figures 8.9a – 8.9c), the pressure transitions to low pressures at the area of gas entrainment (figures 8.9d – 8.9e) and closes with high pressures at the wake flow (Figure 8.9f).
As major observation, the pressure fields in figures 8.9c – 8.9e confirm the presence of a lower pressure potential in the central area of the multi-hole spray. According to the pressure and velocity fields, the mechanism of spray contraction is attributed to an inwardly directed net momentum acting on the spray plumes as a result of a stronger incident flow from the outer directions than from the central area or spray plume interspaces. The jet-to-jet interaction is traced back to induced pressure forces and a resultant competing attraction of ambient gas flow by adjacent spray plumes. The extent to which a spray plume is deflected depends on the net momentum exchanged in relation to the inertia and propagation of the spray.
With increasing atomisation, whether mechanically induced or by flash-boiling, the spray contraction and jet-to-jet interaction intensifies. In Figure 8.10, the pressure and velocity fields of the axisymmetric 3-hole spray is shown for $p_{inj} = 250$ bar, $p_{\infty} = 0.4$ bar and $T_{fuel} = 90°C$ under flash-boiling conditions ($Ja = 32$). In contrast to $p_{\infty} = 1.0$ bar and $T_{fuel} = 25°C$ ($Ja = -5243$) (Figure 8.9), the net momentum is more pronounced as a result of enhanced momentum exchange but also due to a change in the pattern of spray-induced flow. The ratio of incident flow is further shifted to proportions from outer direction, while there is nearly no compensating flow from the centre or spray plume interspaces.
In Figure 8.11, the effect the spray layout is highlighted by the velocity and pressure fields of the non-axisymmetric 3-hole spray at $p_{inj} = 250$ bar, $p_{\infty} = 1.0$ bar and $T_{fuel} = 25°C$ ($Ja = -5243$). Compared to the axisymmetric 3-hole spray (Figure 8.9), the flow pattern shows a different incident flow in relation to the spray plumes under the same operating conditions.

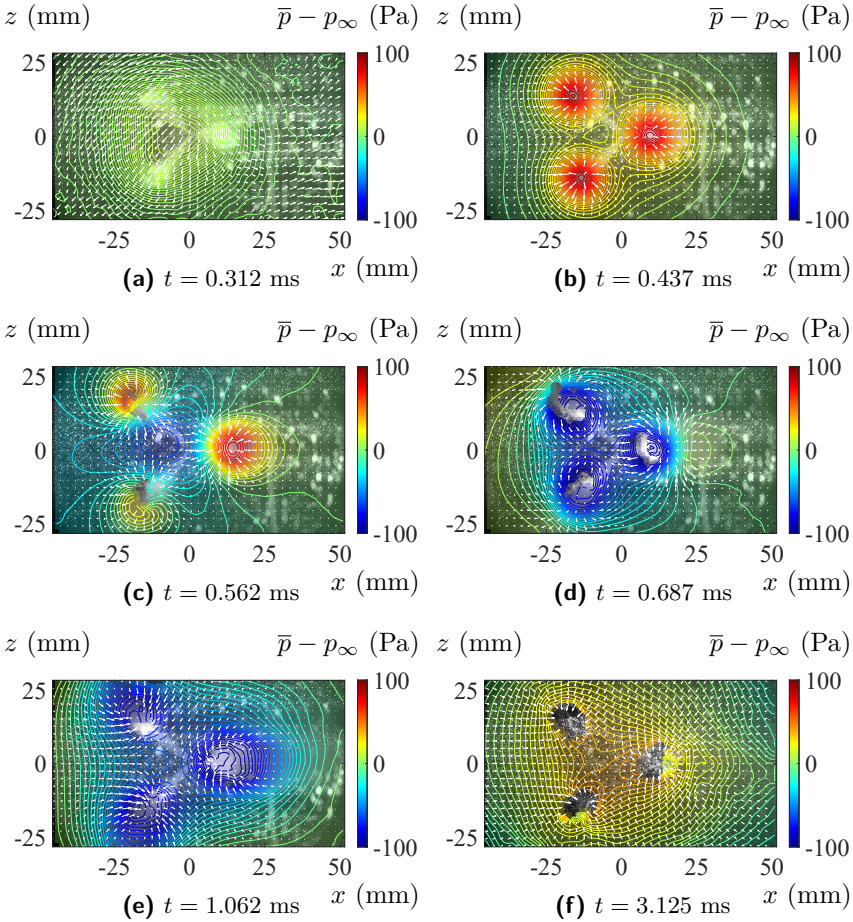

Figure 8.9: Axisymmetric 3-hole spray. Pressure and velocity fields at non-flash-boiling conditions ($Ja = -5243$) with $p_{inj} = 250$ bar, $p_\infty = 1.0$ bar, $T_{fuel} = 25°C$. Time t after SOI. For the purpose of clarity, the velocity field is represented with a quarter of the evaluated velocity vectors.

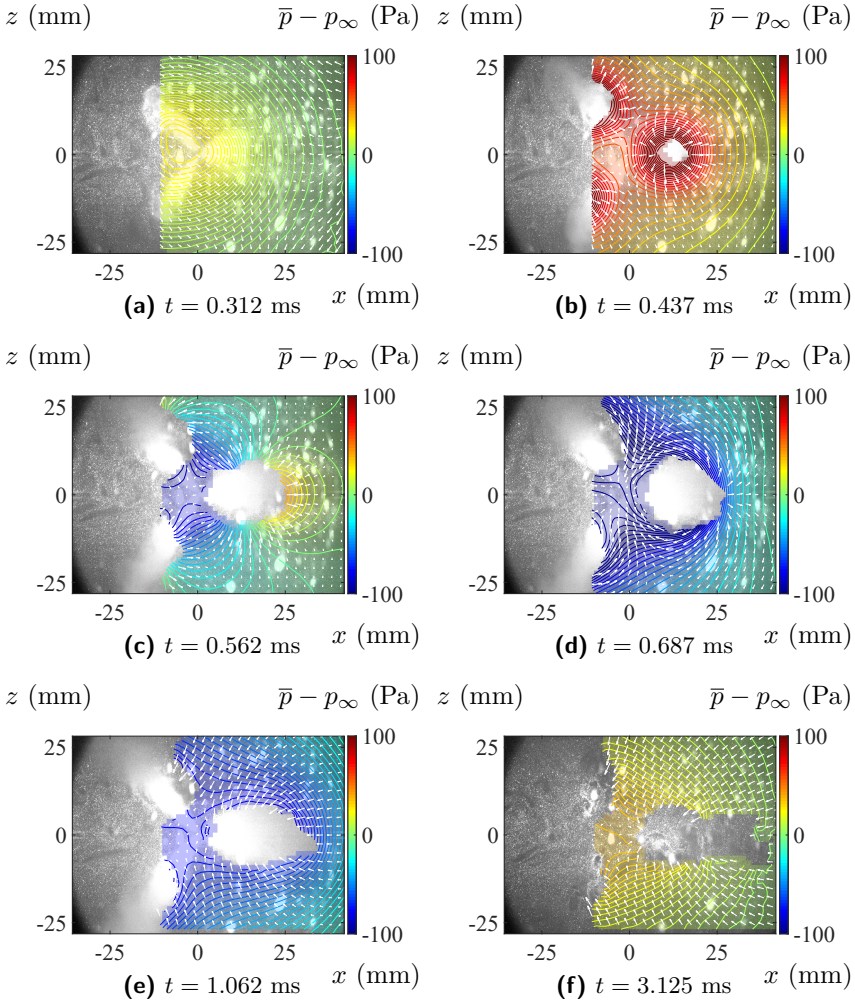

Figure 8.10: Axisymmetric 3-hole spray. Pressure and velocity fields at flash-boiling conditions ($Ja = 32$) with $p_{inj} = 250$ bar, $p_\infty = 0.4$ bar, $T_{fuel} = 90°$C. Time t after SOI. For the purpose of clarity, the velocity field is represented with a quarter of the evaluated velocity vectors.

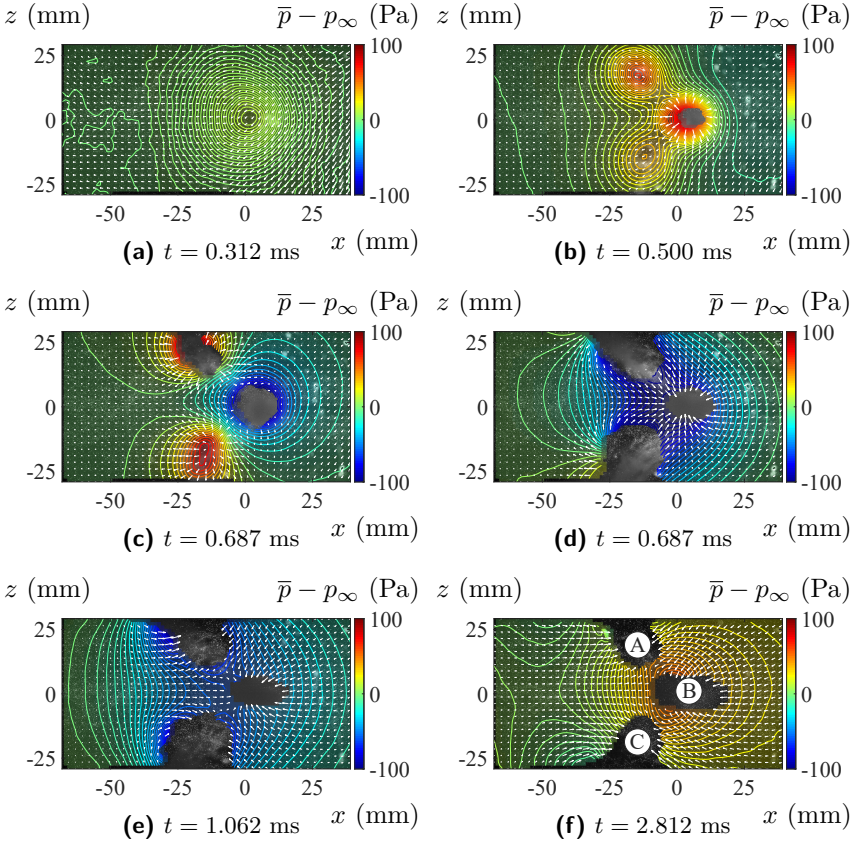

Figure 8.11: Non-axisymmetric 3-hole spray. Pressure and velocity fields at non-flash-boiling conditions ($Ja = -5243$) with $p_{inj} = 250$ bar, $p_\infty = 1.0$ bar, $T_{fuel} = 25°$C. Time t after SOI. For the purpose of differentiation, the spray plumes are marked with (A), (B) and (C). For the purpose of clarity, the velocity field is represented with a quarter of the evaluated velocity vectors.

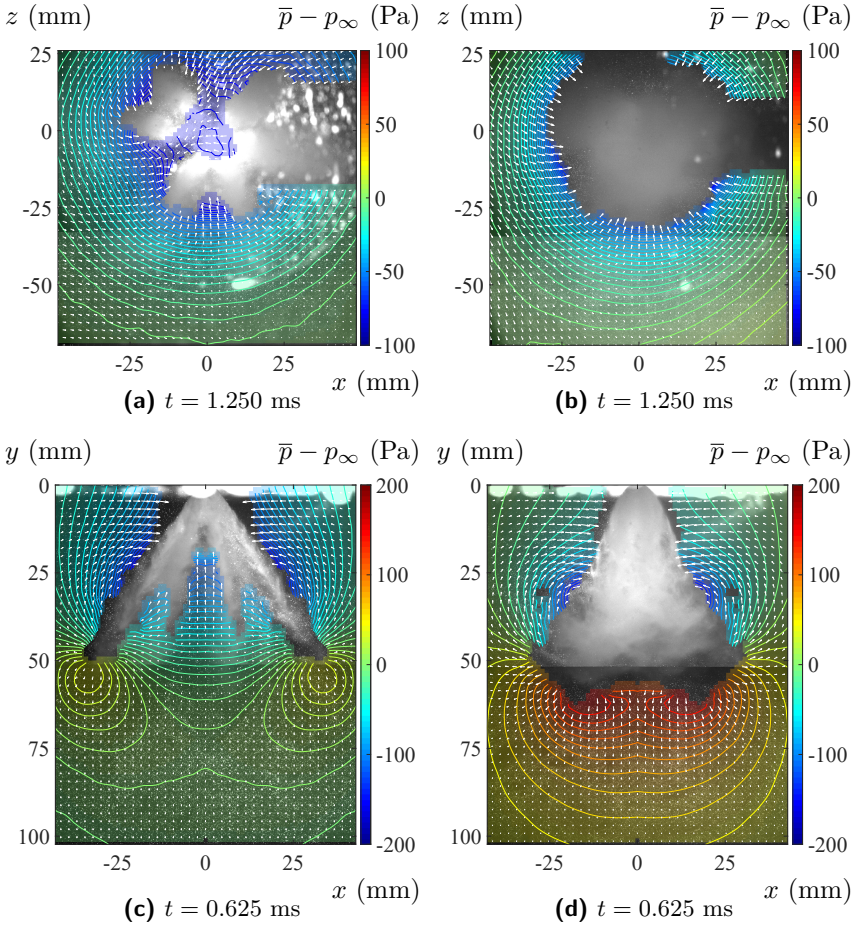

Figure 8.12: Conventional GDI 6-hole spray. Pressure and velocity fields for flash-boiling and non-flash-boiling conditions at $p_{inj} = 250$ bar and time t after SOI. (a, c) non-flash-boiling: $p_\infty = 1.0$ bar, $T_{fuel} = 25°C$, $Ja = -5243$; (b, d) flash-boiling: $p_\infty = 0.4$ bar, $T_{fuel} = 90°C$, $Ja = 32$. For the purpose of clarity, the velocity field is represented with a quarter of the evaluated velocity vectors.

While there is a substantial flow between the more distant spray plumes (A) and (C), the flows in the narrow interspaces are less pronounced. The closer the distance, the lower the respective momentum exerted from that direction and the stronger the jet-to-jet interaction. In the present case, the net momentum acting on the central spray plume (B) points in between the outer spray plumes (A) and (C). In terms of the latter ones, the respective net momentums are mainly directed towards the central spray plume (B) with a slight deviation due to mutual attraction. Essential design parameters with respect to jet-to-jet interaction are therefore the number of spray holes, their arrangement, orientation and mass flow rate. In Figure 8.12, the pressure and velocity fields of the 6-hole spray are shown for a contracting and a non-contracting spray (with and without flash-boiling atomisation). Despite the limited optical access, velocity and pressure field information of the central region and spray plume interspaces are obtained for the non-contracting spray (see figures 8.12a and 8.12c). Equivalent to the previous observation, the velocity field shows a moderate flow in the centre and spray plume interspaces, while there is a significant incident flow from the outer direction. Under flash-boiling condition (see figures 8.12b and 8.12d), the immediate expansion of the spray prevents the velocimetry of spray-induced flow in the centre area and spray plume interspaces. Nevertheless, the inward directed flow in the spray surrounding is well highlighted. The observation of a dominant incident flow as well as lower pressures in the central area of the spray and spray plume interspaces confirms the previous findings on jet-to-jet interaction also for conventional GDI spray layouts. The comparison between contracting and non-contracting spray in Figure 8.12 shows the important influence of atomisation on spray contraction. Although the pressures and velocities are at least in the same order of magnitude, the spray contracts only under flash-boiling conditions for the present example due to the resulting smaller droplet sizes and the increased tracking behaviour.

8.3 Discussion

The present investigation outlines the close interrelation between spray transport and ambient gas flow. Along with the momentum exchange, the inertia and the tracking behaviour of the spray are identified as key.

For the first time, highly-desired pressure field information of a GDI multi-hole spray was experimentally obtained in a cross-sectional plane close to the injector nozzle. The present investigation confirms the hypothesised presence [39–42] of a lower pressure region in the centre area of spray and spray plume interspaces. The pressure and velocity fields indicate that the spray-induced flow of multi-hole sprays generally features a contracting net momentum acting on the spray in the area of entrainment flow. Whether a spray contracts or not appears to be mainly due to the strength of the net momentum and the inertia and propagation of the spray. If there is a sufficient net momentum acting on the spray for a given inertia and tracking behaviour, a gradual or instant contraction sets in.
Spray contraction occurs particularly under flash-boiling conditions. Apart from enhanced momentum exchange and tracking behaviour, the intense and immediate atomisation right after the nozzle exit promotes the jet-to-jet interaction, as the spray plumes are very close to each other right after SOI. Under non-flash boiling conditions, on the other hand, the spray contraction generally sets in later, as the atomisation and spray expansion develops usually less intense and more gradually by mechanical means.
If either the momentum exchange and/or the tracking behaviour of the spray are not sufficiently pronounced, there is no significant deflection of the spray propagation. This is usually the case at lower atomisation, mostly under non-flash-boiling conditions.
In a widely referred study of Zeng *et al.* [31], it was concluded that the penetration length of contracted multi-hole sprays increases with higher levels of superheat. The interpretation, however, did not take into account that a variation in superheat due to a change in ambient gas pressure has significant implications on the spray-gas interaction, as pointed out in the present thesis. The increase in penetration length is not due to flash-boiling atomisation, but to a reduced inertia of the ambient gas flow as a result of a lower ambient gas density. Flash-boiling atomisation actually reduces the penetration length as it promotes both the momentum exchange and the tracking behaviour of the spray through small droplet sizes and an expansion of spray. Regarding operating conditions, the same principles apply to a contracted multi-hole spray as to a single jet (see Chapter 7).
According to the present investigation, the design of the injection system significantly determines the quality of spray transport and whether and to what extent jet-to-jet interaction and spray contraction occur. Essential design parameters are the injection pressure, the spray hole number and

arrangement, the spray targeting (spray hole inclination angles) and the internal nozzle design, which includes the L_{SH}/D_{SH} ratio, edge rounding, spray hole conicity and potential pre-hole steps. Conceivable options to actively control the spray transport and jet-to-jet interaction during the operation in combustion engines are the SOI, injector control timing, multiple injection strategies as well as exhaust gas recirculation, valve lift/control timing and tumble/swirl flaps.

9 Dual-Plane Stereo Astigmatism (DPSA)

In this chapter, the methodology of the Dual-Plane Stereo Astigmatism (DPSA) technique is presented. The DPSA technique is a novel approach that allows the experimental determination of the full velocity gradient tensor of a flow in planar domain. It was developed in the framework of the present thesis in order to provide a velocimetry technique that enables the evaluation of instantaneous pressure fields for the analysis of spray-induced flows of individual injection events by means of a standard high-speed stereo-PIV system, i.e. a total number of two cameras and one light source. Given the specific requirements of spray-induced flow measurement, the development of DPSA attempts to enable the investigation of shot-to-shot deviations, complex flow structures and stochastically occurring flow processes – in GDI often associated with cavitating nozzle flow [73] – , which cannot be addressed with the statistical approach based on URANS and ensemble averaging [50] (see Chapter 4) by nature.

In the following, the principles of DPSA including post-processing schemes, particle identification strategies and specific approaches for the analysis of particle displacement are outlined. A thorough evaluation and discussion of DPSA and the developed processing is given based on synthetic and first experimental investigations. "A comparison between DPSA and conventional dual-plane stereoscopic PIV (DPSPIV) is conducted by means of synthetic images, as derived from DNS results of a turbulent boundary-layer flow [138]." [51]

For proof of concept, first DPSA measurements of spray-induced flow were performed for two different configurations – a simultaneous PIV and Dual-Plane Astigmatism (DPA) measurement for the purpose of validation and a full DPSA measurement that allows the computation of the full velocity gradient tensor. The valuable findings and lessons learned from these investigations will serve as a basis for future comprehensive spray studies.

The following sections are based on the publication of Kling *et al.* [51]. For ease of reading, a nomenclature consistent with the literature [10] is used. In this chapter, the Einstein summation convention does not apply.

9.1 Principles

"The principle of DPSA is based on the spatial extension of planar stereoscopic particle image velocimetry (stereo-PIV) by means of dual-plane illumination and astigmatism-based depth codification. In contrast to existing dual-plane approaches [90] which utilise either polarisation or different wavelengths to achieve a separation of measurement planes, the DPSA technique images particles simultaneously on joint recordings and subsequently allocates them by image processing [to allow the separate evaluation of particle displacements in two planar domains, which provides the aspired information for the determination of the out-of-plane velocity gradients].
The concept [of DPSA] allows the reduction of the required measurement equipment from either four cameras using the polarisation-based approach or two colour cameras and light sources each using different wavelengths to a total of two cameras. In comparison to diffraction-based velocimetry techniques such as astigmatism particle tracking velocimetry (APTV) [93, 94] and defocusing PIV [95], which provide a spatially continuous determination of the particle depth along the optical axis of the camera, the DPSA approach is confined to a pair of planar measurement domains. In return, the concept of DPSA allows a simplified determination of particle depth by the identification (distinction) of discrete particle image shapes." [51]
"According to Olsen and Adrian [105], the particle image dimensions are described by the contributions of geometric imaging, diffraction and out-of-focus. In terms of monochromatic light, the particle image dimensions are described by

$$d_{e_{ij}} = \left(M_i^2 d_p^2 + 5.95 \left(M_i + 1\right)^2 \lambda^2 f_{\#_i}^2 + \frac{M_i^4 f_i^2}{f_{\#_i}^2} \frac{z_{ij}^2}{\left(f_i \left(M_i + 1\right) + M_i z_{ij}\right)^2} \right)^{\frac{1}{2}} \quad \text{with } i, j = 1, 2, \tag{9.1}$$

[where the indices i and j denote the respective dimensions and measurement planes as shown in Figure 9.1]. M_i are the optical magnifications, f_i are the focal lengths, d_p is the particle diameter, λ is the wavelength of

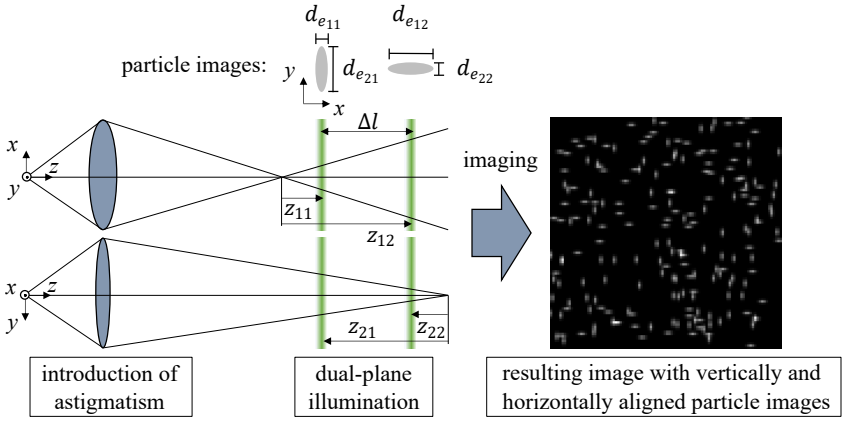

Figure 9.1: "Generation of astigmatism-based particle image deformation. Left: optical setup; different focal line positions with regard to the x- and y-directions. Right: Resulting image showing vertically and horizontally distorted particle images." [51]

light, $f_{\#_i}$ are the f-numbers and z_{ij} are the distances between the focal lines and the measurement planes.

In DPSA, the out-of-focus effect is used for the codification of particle depth. In Figure 9.1, the principle of the DPSA approach is shown schematically. The particle image dimensions are dependent on the distances between the focal lines and the measurement planes. Due to the introduction of astigmatism, the particle image dimensions are decoupled in terms of spatial dimensions. The particle image shapes range from circular to horizontally and vertically aligned ellipses. The extents of the particle image dimensions increase with growing distance between the focal lines and the corresponding measurement plane. Each measurement plane relates to a set of similar, representative particle images. The identification of particle image shapes provides the allocation of particles to respective measurement planes and hence, the assignment of particle depth.

To be able to control the particle image dimensions by the specification of the optical system and the experimental setup is a key aspect in DPSA, since it enables the application for a wide range of experimental configurations and the adjustment of optimised conditions for evaluation.

According to Equation 9.1, the particle image dimensions are dependent on the optical system, the particle diameter, the wavelength of light and the experimental setup. [...] The following geometric relation between the dual-plane spacing Δl and the distances z_{ij} applies for the optical configuration as illustrated in Figure 9.1:

$$\Delta l + z_{i1} - z_{i2} = h_i \left(M_i, f_i, f_{\#_i}, d_p, \lambda, d_{e_{i1}}, d_{e_{i2}} \right) \tag{9.2}$$

In reference to Equation 9.1, the distances between the focal lines and the measurement planes are given by [...]" [51]

$$z_{ij} = f_i \frac{1 + M_i}{M_i} \frac{d_{e_{ij}}^2 - B}{d_{e_{ij}}^2 - B - E^2} \left(-1 \pm E \sqrt{\frac{1}{d_{e_{ij}}^2 - B}} \right) \tag{9.3}$$

with

$$B = M_i^2 d_p^2 - 5.95 \left(M_i + 1 \right)^2 \lambda^2 f_{\#_i}^2 \text{ and } E = M_i f_i / f_{\#_i}.$$

"In principal, there are two solutions of z_{ij} concerning a single particle image dimension. Therefore, considering Equation 9.2, there is a total of four potential configurations for a particular set of particle image dimensions $\mathbf{d}_{e,p_1} = (d_{e11}, d_{e12})^{\mathrm{T}}$ and $\mathbf{d}_{e,p_2} = (d_{e21}, d_{e22})^{\mathrm{T}}$ with respect to the measurement planes. In Figure 9.2, the potential configurations for a specific set of particle image dimensions are shown exemplary for a pair of equally distorted particle images. For a stereoscopic setup with an incidence angle between image plane and object plane, the optical magnification varies over the image plane. Since the out-of-focus term is a function of the optical magnification, the particle image dimensions are not uniform. To reduce the effect of the particle image variation, the use of small incidence angles and the application of the Scheimpflug criterion are viable. In Figure 9.3, an optical system with parallel shifted principle planes is shown. In this case, the Scheimpflug criterion applies for one of the spatial dimensions of each object plane.
The DPSA approach does not require an uniform in-plane distribution of particle image shapes since the allocation of particles is based on the differentiation of principal particle image shapes/types." [51]

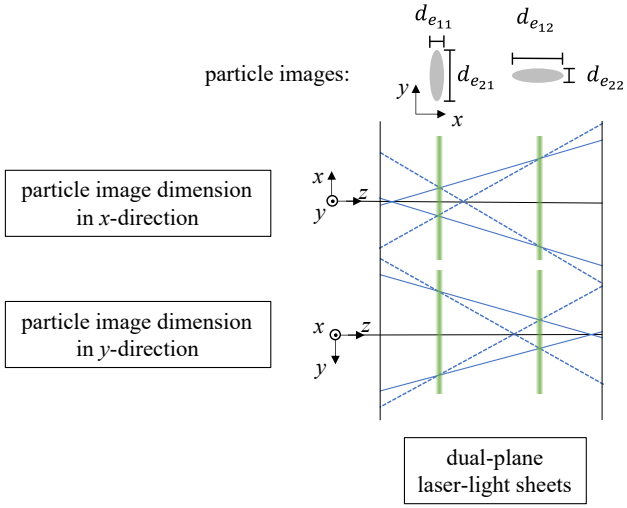

Figure 9.2: "Possible configurations for a specific set of particle image dimensions; vertically distorted particle images at the narrow plane and horizontally distorted particle images at the rear plane." [51]

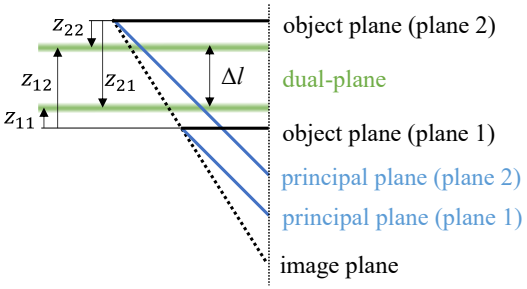

Figure 9.3: "Exemplary arrangement for the application of the Scheimpflug criterion in case of spatially decoupled principle planes." [51]

9.2 Processing

"In contrast to conventional PIV and PTV evaluation, the DPSA approach requires further processing to enable the displacement analysis of the joint image recordings. An essential aspect in DPSA image processing is the presence of particle overlapping. The DPSA method is subject to an increased probability of particle overlap due to the superposition of two measurement planes (depth levels). In comparison to planar PIV, particle overlapping occurs even at low to moderate particle densities. To guarantee an accurate and robust evaluation, particle overlapping has to be taken into account in DPSA image processing.
A viable approach for the identification of particles in the presence of particle overlapping is the image matching technique. Based on the intensity distribution, particles are identified through a best-fit approximation of particle images. In the work of Wieneke [139], a sophisticated method for the reconstruction of dense particle fields was introduced. The method uses image matching to iteratively reconstruct the intensity distribution, allowing the successive identification of overlapping particles.
To provide a robust and versatile evaluation in case of weak signal-to-noise ratios and non-uniform particle images, an alternative approach for the identification of particles was developed in the framework of DPSA. The principle of the method is based on the identification of particle image shapes via the image cross-correlation with representative particle images. In contrast to the IPR technique, the method addresses exclusively non-overlapping particles. In the following, the method is presented in detail." [51]

9.2.1 Correlation-based particle identification (CPI)

The intensity distribution of a PIV recording is described by the superposition of multiple point spread functions that characterise the image response of a lens system to the captured light from the particles. In terms of diffraction-limited and aberration-free imaging the point spread functions can be mathematically approximated by the bivariate normal distribution [10]

$$\tau\left(\mathbf{x}-\mathbf{x}_i,\mathbf{d}_{e_i}\right)=\frac{\beta^2}{2\pi d_{ex_i}d_{ey_i}}\exp\left(-\frac{\beta^2}{2}\left(\frac{\left(x-x_i\right)^2}{d_{ex_i}^2}+\frac{\left(y-y_i\right)^2}{d_{ey_i}^2}\right)\right), \tag{9.4}$$

where $\mathbf{x} = (x, y)^{\mathrm{T}}$ is the image plane vector, $\mathbf{x}_i = (x_i, y_j)^{\mathrm{T}}$ is the image plane particle position of the particle with index i, $\mathbf{d}_{e_i} = (d_{ex_i}, d_{ey_i})^{\mathrm{T}}$ is a vector that characterises the size of the particle image dimensions and $\beta = 5.4$ [140] is a factor that is employed for the approximation of the diffraction pattern. In DPSA, the aspect ratio of the particle images usually differ due to the spatial decoupling of the focal lines. The intensity distribution of a DPSA recording can be expressed by

$$I\left(\mathbf{x}, \mathbf{\Gamma}, \mathbf{\Lambda}, \mathbf{\Omega}\right) = \sum_{i=1}^{N_p} I_{p_i} \tau\left(\mathbf{x} - \mathbf{x}_i, \mathbf{d}_{e_i}\right) \tag{9.5}$$

$$\text{with } \mathbf{\Gamma} = \begin{pmatrix} \mathbf{x}_1 \\ \mathbf{x}_2 \\ \vdots \\ \mathbf{x}_{N_p} \end{pmatrix}, \ \mathbf{\Lambda} = \begin{pmatrix} I_{p_1} \\ I_{p_2} \\ \vdots \\ I_{p_{N_p}} \end{pmatrix}, \ \mathbf{\Omega} = \begin{pmatrix} \mathbf{d}_{e_1} \\ \mathbf{d}_{e_2} \\ \vdots \\ \mathbf{d}_{e_{N_p}} \end{pmatrix}, \ \mathbf{d}_{e_i} = \begin{pmatrix} d_{ex_i} \\ d_{ey_i} \end{pmatrix},$$

where I_{p_i} describes the particle image intensity of the particle with index i and N_p is the number of particles. $\mathbf{\Gamma}$, $\mathbf{\Lambda}$ and $\mathbf{\Omega}$ are sets of the particle image intensities, positions and dimensions. The notation is partly recaptured from Raffel *et al.* [10].

Particle identification and allocation

To identify the measurement plane affiliation of a particle, the CPI method utilises the image cross-correlation technique to check whether a particle is more likely to match the particle image shape associated with one or the other measurement plane. For this purpose, the image is cross-correlated with a characteristic particle image $\mathbf{d}_{e,p_j}$ for each of the two measurement planes j (e.g. horizontally and vertically aligned particle image shapes) and evaluated at the image plane particle positions $\mathbf{x}_i$. The particle affiliation is determined by the largest cross-correlation value

$$L_{p_i}\left(\mathbf{x}_i, \mathbf{\Gamma}, \mathbf{\Lambda}, \Omega\right) = \begin{cases} 1, \text{if} & R_{I,max}\left(\mathbf{x}_i, \mathbf{\Gamma}, \mathbf{\Lambda}, \Omega\right) = R_{I_1}\left(\mathbf{x}_i, \mathbf{\Gamma}, \mathbf{\Lambda}, \Omega\right) \\ 2, \text{if} & R_{I,max}\left(\mathbf{x}_i, \mathbf{\Gamma}, \mathbf{\Lambda}, \Omega\right) = R_{I_2}\left(\mathbf{x}_i, \mathbf{\Gamma}, \mathbf{\Lambda}, \Omega\right), \end{cases} \tag{9.6}$$

with

$$R_{I,max}\left(\mathbf{s},\mathbf{\Gamma},\mathbf{\Lambda},\Omega\right)=\max\left(R_{I_1}\left(\mathbf{s},\mathbf{\Gamma},\mathbf{\Lambda},\Omega\right),R_{I_2}\left(\mathbf{s},\mathbf{\Gamma},\mathbf{\Lambda},\Omega\right)\right), \tag{9.7}$$

and the plane-specific cross-correlation function

$$\begin{aligned} R_{I_j}\left(\mathbf{s},\mathbf{\Gamma},\mathbf{\Lambda},\Omega\right) &= \int_I I\left(\mathbf{x},\mathbf{\Gamma},\mathbf{\Lambda},\Omega\right)\tau\left(\mathbf{x}+\mathbf{s},\mathbf{d}_{e,p_j}\right)\mathbf{dx} \\ &= \int_I\left[\sum_{i=1}^{N_p} I_{p_i}\tau\left(\mathbf{s}+\mathbf{x}_i,\mathbf{d}_{e_i}+\mathbf{d}_{e,p_j}\right)\right]\mathbf{dx}, \end{aligned} \tag{9.8}$$

where $\mathbf{s}$ is a shift vector. "Note, that the cross-correlation of two normal distributions $f\sim\mathbb{N}\left(\mu_1,\sigma_1\right)$ and $g\sim\mathbb{N}\left(\mu_2,\sigma_2\right)$ with the means μ_1,μ_2 and standard deviations σ_1,σ_2 describes a joint normal distribution with $f\star g\sim\mathbb{N}\left(\mu_1-\mu_2,\sigma_1+\sigma_2\right)$." [51]
Figure 9.4 shows the application of the CPI method on a synthetic DPSA image with horizontally and vertically aligned particle images. Based on the cross-correlation functions R_{I_1} and R_{I_2}, the detected particles are allocated to the respective measurement planes according to Equation 9.6. The particle detection is carried out by a peak detection algorithm in conjunction with a subpixel refinement, e.g. Gaussian peak fit [141]. The principle of the peak detection algorithm is based on the comparison of neighbouring pixel values. If the pixel under investigation has a higher

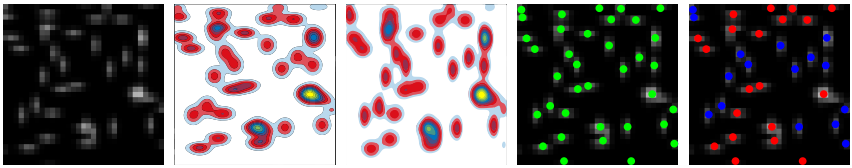

(a) raw image **(b)** R_{I_1} **(c)** R_{I_2} **(d)** detected **(e)** allocated

Figure 9.4: CPI particle identification and allocation processing. Cross-correlation of a synthetic DPSA image (a) with vertically and horizontally aligned particle images representative of the associated measurement planes $j=1,2$. Based on the cross-correlation values (b, c) at the detected particle locations (d), the particles are assigned to the respective measurement planes (e). Markers: red dots - $j=1$, blue dots - $j=2$.

value than its neighbouring pixels, the position is considered as a potential particle. The particle detection can be either applied on the raw image or on the distributions of the cross-correlation functions. Usually the application of the peak detection algorithm is performed on the raw image. However, in case of large particle images, optical aberrations or low signal-to-noise ratios, the application of the peak detection algorithm on the cross-correlation distributions yields favourable results.
The CPI method applies for non-overlapping particles. However, to some extent the CPI method is also able to operate on overlapping particles. This largely depends on the respective constellation and quality of particle overlapping. The relative positions and dimensions of the particle images are decisive. In case of strong particle overlapping, the cross-correlation criterion (Equation 9.6) becomes inaccurate.

Detection of overlapping particles

"To guarantee an exclusive evaluation of non-overlapping particles, the CPI method requires the detection of particle overlapping. In the following, different detection criteria are presented." [51]

Image matching A viable approach for the detection of particle overlapping is given by the technique of 'image matching'. As shown in Figure 9.5, the principle of the approach is based on the reconstruction of the image using synthetic particle images and the subsequent analysis of the resulting intensity residual, which serves as a measure for particle overlapping. For the reconstruction of the image, the synthetic particle images are positioned at a priori estimated subpixel positions. The synthetic particle images are fitted in shape and intensity such that each pixel intensity does not exceed the corresponding pixel intensity of the image. In case of particle overlapping, the estimated particle locations deviate from the actual particle positions. As a result, the matching process yields a residual intensity which indicates particle overlapping. In the present work, the ratio of the particle intensity I_p and the residual intensity I_{res} is used as criterion for particle overlapping. If a certain threshold ϵ_{int} is exceeded,

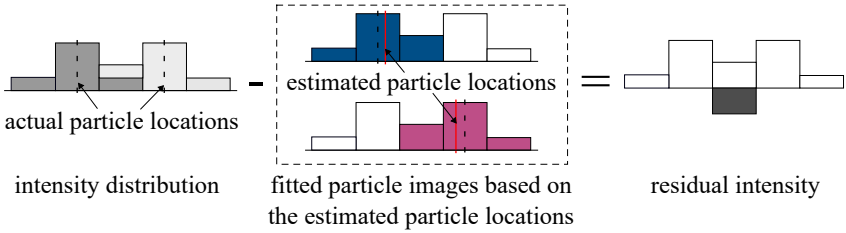

Figure 9.5: Identification of particle overlap via image matching [51].

the presence of particle overlapping is assumed. The criterion [51] is given by

$$\frac{I_{res}}{I_p} > \epsilon_{int}. \tag{9.9}$$

Geometrical intersection "The relative particle positions and their corresponding particle image sizes are used for the determination of potential particle image intersection. For each particle, the nearest adjacent particle is identified and checked for a geometric overlap of the particle images. The potential intersection of two elliptical curves can be determined analytically. However, for the reason of fast computation and simple implementation, a numerical approach is used in the present work. For the detection of particle overlapping, the normalised intensity of the particle image intersection I_{inter} is used [as criterion, which is given by]

$$\frac{I_{inter}}{I_p} > \epsilon_{geom}. \tag{9.10}$$

ϵ_{geom} represents the threshold of the geometric criterion." [51]

Ratio of the cross-correlation peaks A further criterion for the identification of particle overlapping is the ratio of the cross-correlation values. If the ratio

$$r_{peak_i}\left(\mathbf{x}_i, \mathbf{\Gamma}, \mathbf{\Lambda}, \Omega\right) = \frac{R_{I,max}\left(\mathbf{x}_i, \mathbf{\Gamma}, \mathbf{\Lambda}, \Omega\right)}{R_{I,min}\left(\mathbf{x}_i, \mathbf{\Gamma}, \mathbf{\Lambda}, \Omega\right)} \tag{9.11}$$

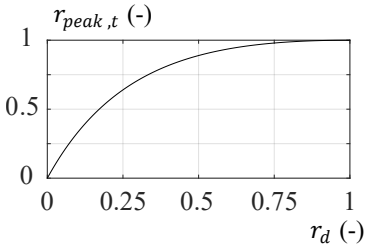

Figure 9.6: Theoretical cross-correlation ratio $r_{peak,t}$ as a function of the deformation ratio r_d [51].

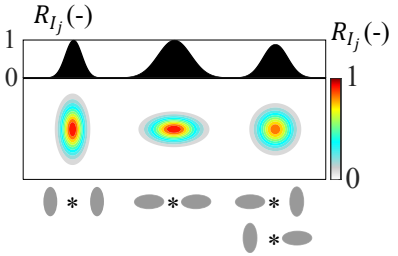

Figure 9.7: Side-by-side comparison of matching and non–matching image cross-correlations [51].

with

$$R_{I,min}\left(\mathbf{s},\mathbf{\Gamma},\mathbf{\Lambda},\Omega\right)=\min\left(R_{I_1}\left(\mathbf{s},\mathbf{\Gamma},\mathbf{\Lambda},\Omega\right),R_{I_2}\left(\mathbf{s},\mathbf{\Gamma},\mathbf{\Lambda},\Omega\right)\right)$$

of a particle with index i strongly deviates from the expected, theoretical ratio $r_{peak,t}$, the presence of particle overlapping is likely. Assuming particle images with mirrored dimensions $\mathbf{d}_{e,p_1}=\left(d_{e_1},d_{e_2}\right)^{\mathrm{T}}$ and $\mathbf{d}_{e,p_2}=\left(d_{e_2},d_{e_1}\right)^{\mathrm{T}}$, the theoretical cross-correlation ratio is given by

$$\begin{aligned} r_{peak,t} &= \frac{\tau\left(\mathbf{0},\mathbf{d}_{e,p_1}+\mathbf{d}_{e,p_2}\right)}{\tau\left(\mathbf{0},2\mathbf{d}_{e,p_{1,2}}\right)} \\ &= \frac{4d_{e_1}d_{e_2}}{\left(d_{e_1}+d_{e_2}\right)\left(d_{e_2}+d_{e_1}\right)} \\ &= 4\frac{r_d}{\left(1+r_d\right)^2} \end{aligned} \tag{9.12}$$

with the deformation ratio $r_d=d_{e_1}/d_{e_2}$ [51].
As shown in Figure 9.6, the theoretical cross-correlation ratio is close to one for a wide range of deformation ratios. For a deformation ratio of $r_d=0.8$, as shown in Figure 9.7 by a side-by-side comparison of matching and non-matching image cross-correlations of particle images, the theoretical cross-correlation ratio yields $r_{peak,t}\approx 0.98$. "Values close to one correspond to a comparatively low robustness and an increased susceptibility to noise. Inversely, by having a higher degree of particle image deformation, the signal to noise ratio declines and the uncertainty of particle localisation

increases. For the detection of particle overlapping, the difference between the theoretical and the actual correlation peak ratio

$$|r_{peak,t} - r_{peak_i}| > \epsilon_{cross} \tag{9.13}$$

is used." [51]

9.2.2 PIV evaluation

Due to the joint recording of the measurement planes, the use of conventional image cross-correlation is not applicable for PIV evaluation in DPSA. In the framework of the present thesis, an alternative approach was developed, which operates on the information of identified particle locations. In contrast to the cross-correlation of image pairs, the principle of the approach is based on the cross-correlation of bivariate normal distributions which represent the particle images mathematically. The approach is formulated by

$$\begin{aligned} R_I\left(\mathbf{s}, \mathbf{\Gamma}^{(1)}, \mathbf{\Gamma}^{(2)}, \mathbf{d}, \mathbf{d}_e\right) &= \sum_{i=1}^{N_p^{(1)}} \sum_{j=1}^{N_p^{(2)}} \int_{IA} \tau\left(\mathbf{x} - \mathbf{x}_i^{(1)}, \mathbf{d}_e\right) \tau\left(\mathbf{x} - \mathbf{x}_j^{(2)} + \mathbf{s} - \mathbf{d}, \mathbf{d}_e\right) \mathbf{dx} \\ &= \sum_{i=1}^{N_p^{(1)}} \sum_{j=1}^{N_p^{(2)}} \tau\left(\mathbf{s} - \mathbf{d} + \mathbf{x}_i^{(1)} - \mathbf{x}_j^{(2)}, 2\mathbf{d}_e\right) \end{aligned} \tag{9.14}$$

with

$$\mathbf{\Gamma}^{(1)} = \left(\mathbf{x}_1^{(1)}, \mathbf{x}_2^{(1)}, \cdots, \mathbf{x}_{N_p^{(1)}}^{(1)}\right)^{\mathrm{T}}, \mathbf{\Gamma}^{(2)} = \left(\mathbf{x}_1^{(2)}, \mathbf{x}_2^{(2)}, \cdots, \mathbf{x}_{N_p^{(2)}}^{(2)}\right)^{\mathrm{T}},$$

where $\mathbf{d}_e$ describes the dimensions of the bivariate normal distributions and $\mathbf{d}$ is a displacement vector. The superscripts $(\cdot)^{(1)}$ and $(\cdot)^{(2)}$ denote the first and second exposure. "The cross-correlation is described by the sum of the joint bivariate normal distributions of all particle combinations. In Figure 9.8, the cross-correlation of an exemplary particle displacement is shown. The mathematical description allows an arbitrarily accurate localisation of the cross-correlation peak, since the subpixel accuracy depends on the numerical discretisation of the cross-correlation. Consequently, no Gaussian peak fit is required. The PIV evaluation is free of noise. However, the evaluation

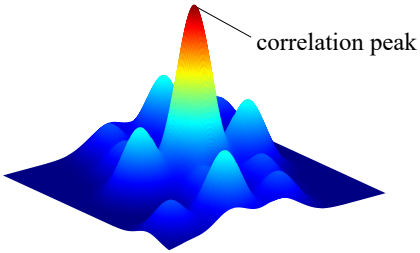

Figure 9.8: Representation of a cross-correlation map based on an evaluation that takes five particles into account [51].

is dependent on the accuracy of particle localisation, which is [generally] subject to errors due to noise and particle overlapping for example.
The approach allows the implementation of advanced digital interrogation techniques such as multiple pass interrogation schemes [109, 110], grid refining [142] and window deformation [111]." [51]

Window deformation To account for in-plane velocity gradients and improve the accuracy of displacement analysis, the window deformation technique [111] is a viable and widely used technique in PIV evaluation. The implementation within the present concept of PIV evaluation is quite straightforward. Based on the Jacobi matrix of an a priori estimated displacement field $\mathbf{J}_{IA}$, the particles are shifted accordingly as illustrated schematically in Figure 9.9. The formulation of the cross-correlation function with window deformation is given by

$$R_I\left(\mathbf{s},\mathbf{\Gamma}^{(1)},\mathbf{\Gamma}^{(2)},\mathbf{d},\mathbf{d}_e,\mathbf{J}_{IA}\right)=\sum_{i=1}^{N_p^{(1)}}\sum_{j=1}^{N_p^{(2)}}\tau\left(\mathbf{s}-\mathbf{d}+\mathbf{x}_i^{(1)}-\mathbf{x}_j^{(2)}-\mathbf{J}_{IA}\cdot\left(\mathbf{x}_i^{(1)}-\mathbf{x}_j^{(2)}\right),2\mathbf{d}_e\right) \tag{9.15}$$

with

$$\mathbf{J}_{IA}=\begin{pmatrix}\frac{\partial \mathrm{d}x_{IA}}{\partial x} & \frac{\partial \mathrm{d}x_{IA}}{\partial y}\\ \frac{\partial \mathrm{d}y_{IA}}{\partial x} & \frac{\partial \mathrm{d}y_{IA}}{\partial y}\end{pmatrix},$$

where $\mathrm{d}x_{IA}$ and $\mathrm{d}y_{IA}$ describe the displacement of the particle ensemble within the IW in x- and y-direction.

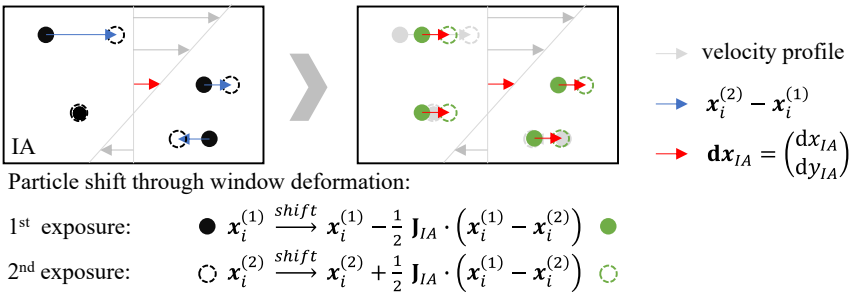

Figure 9.9: Schematic representation of the implemented window deformation approach, where particles are shifted for both exposures (1) and (2) to account for the presence of velocity gradients.

9.2.3 Iterative Particle Reconstruction (IPR)

"To address also the identification of overlapping particles, the IPR method according to Wieneke [139] is adapted. The basic idea of the IPR method is the iterative reconstruction of particles based on the intensity distributions of the raw images. After an initial estimation of particle locations, particles are fitted by displacing the particle locations ('shaking') and changing the particle image dimensions. The original IPR method [139] operates in three dimensional space and utilises multiple perspectives to reduce ambiguity. Typically, three or more cameras are used for volumetric particle reconstruction. Considering the present DPSA approach, an application of the IPR method requires a minimum number of two perspectives due to the additional information by astigmatism." [51]

In the present work, an adaptation of the IPR method is proposed, which is based on a single perspective. "The intention of a single perspective IPR is due to simplicity, [reduced] computational expense and the potential application on single-camera dual-plane PIV. However, the particle identification is much more susceptible to ambiguity, strong particle overlapping (merge without distinct peaks) and initialisation. Similar to [Wieneke] [139], the proposed single-perspective IPR approach operates with external and internal iterations. For particle fitting, incremental steps of particle displacements and different sets of particle image dimensions are used." [51]

9.2.4 Calibration

For the computation of the planar displacement fields, a separate calibration of the measurement planes is required [51]. As the measurement planes are usually not in focus in DPSA, a tailored calibration process consisting of a base calibration and a subsequent refined calibration for each of the measurement planes is proposed.
The base calibration is performed according to the procedure of stereoscopic viewing calibration [10] (see Chapter 3). For the mapping of the image space to the object space, a two-level calibration target with circular dot pattern is used. The calibration target is positioned so that one of the spatial dimensions is in focus, which allows for a more accurate characterisation of the target pattern through image recognition.
Based on the initial calibration, a separate and refined calibration is performed for each of the measurement planes using the 'disparity correction' method [10]. For the application of the method, a separate evaluation of the measurement planes is required. In the framework of the present work two different strategies are proposed. Firstly, an one-by-one evaluation of the measurement planes by using a single-plane illumination for the calibration and secondly, an evaluation that is based on the allocation of the particles to the measurement planes via CPI or IPR image processing. The latter approach is considered more handy and flexible, while the first one is more accurate since no additional uncertainty due to particle overlapping is included.

9.3 Performance assessment

"The IPR and CPI methods are assessed by synthetic images. The assessment addresses the influence of particle density, particle image size and noise. For the generation of synthetic images, a random generator with uniform probability distribution is used for the definition of particle locations. Note that a minimum image-plane particle distance of 1.5 pixels is enforced, such that particle overlapping exclusively stems from the superposition of the measurement planes. The particle intensity is assumed as uniform. The synthetic images have an image resolution of 100×100 px. For image processing, the IPR method is carried out with eight external

and six internal iterations. The CPI method uses a numerical discretisation of 0.05 px for cross-correlation and $\epsilon_{geom} = 0.1$, $\epsilon_{corr} = 0.1$, $\epsilon_{int} = 0.15$ as thresholds.
In Figure 9.10, the results of the particle identification are shown for different particle densities. Both methods show a comparatively high identification rate for a particle density of 0.01 ppp. However, the CPI technique is subject to a certain degree of miss allocation. Due to its ability to reconstruct overlapping particles, the IPR method allows the identification of particles, even for dense particle fields with 0.05 and 0.1 ppp. In contrast, the CPI method, which addresses exclusively non-overlapping particles, shows a significantly lower identification rate for higher particle densities. However, the results indicate that even for dense particles fields a certain number of particles are retrieved, in particular for 0.05 ppp.
In Figure 9.11, the rate of particle identification and allocation are shown for different particle image sizes and signal-to-noise ratios as a function of particle density. In accordance to the previous observation, the particle identification rate of the IPR method is higher than the identification rate of the CPI method. In general, it is observed that higher noise levels lower the rate of particle identification as well as the validity of particle allocation. With regard to particle image size, larger values lead to a significantly lower identification rate, which is caused by an increased occurrence of particle overlapping. In terms of particle allocation, the CPI approach shows a constant level, whereas for the IPR method, the level decreases for higher particle image sizes. This is due to the fact that for higher particle image sizes the reconstruction is more likely to converge to a different solution than to the actual particle locations." [51]

9.4 Assessment of DPSA by means of synthetic particle images

"In order to assess the applicability and robustness of the DPSA method for general three-dimensional (3D) turbulent flow scenarios, the DNS data of a transitional/turbulent boundary-layer flow [138] is considered. Originally, the data was simulated with the purpose to provide a reference for comparison with various active flow control efforts. In the present context,

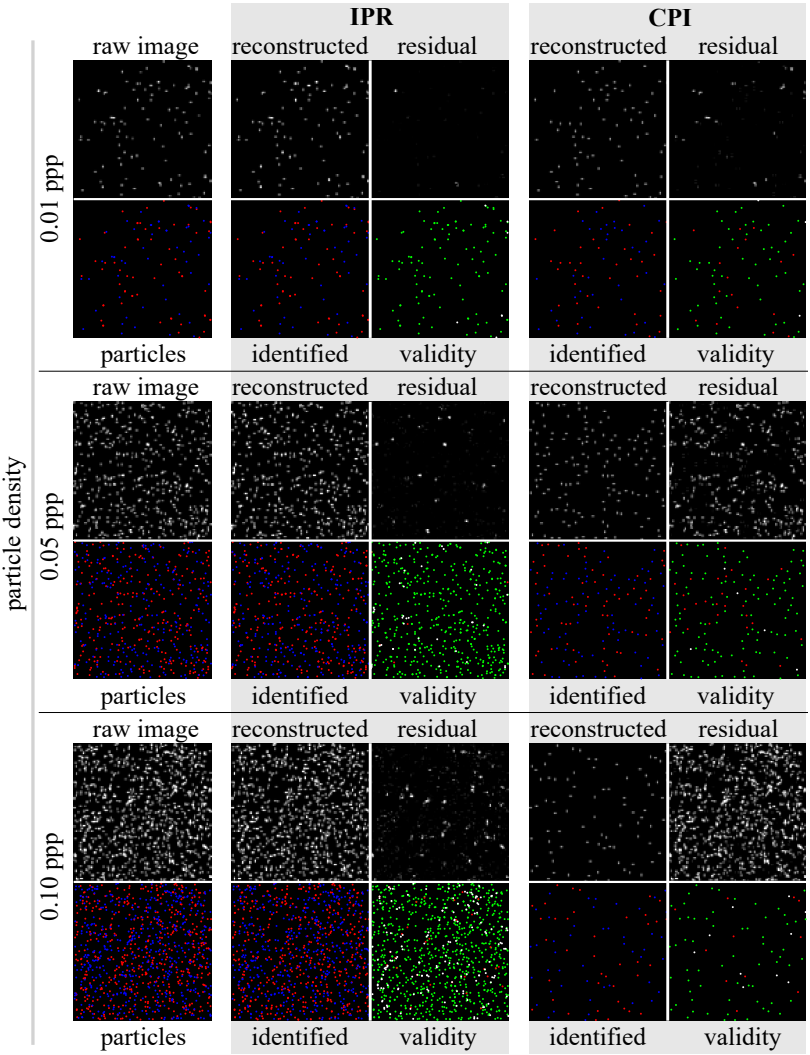

Figure 9.10: Particle identification and allocation for different particle densities [51]. Comparison of IPR and CPI results. Particle image dimensions: $d_{e_{11}} = d_{e_{22}} = 2.5$ px, $d_{e_{21}} = d_{e_{12}} = 3.5$ px; no noise; particle locations: *red* – front plane, *blue* – rear plane; validity: *green* – correct, white – incorrect particle location, *red* – incorrect assignment.

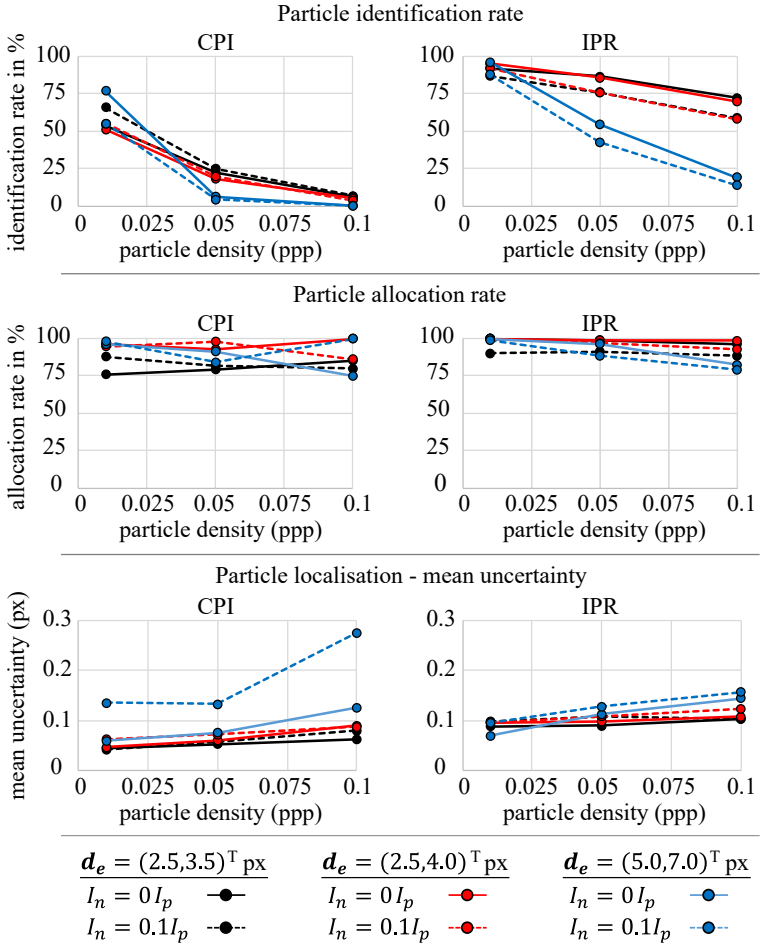

Figure 9.11: "Performance assessment of the CPI [...] and IPR method. Particle identification rate - correct particle localisation (<0.5 px) and particle allocation; particle allocation rate; mean uncertainty of particle localisation. Thresholds: $\epsilon_{geom} = 0.1$, $\epsilon_{corr} = 0.1$, $\epsilon_{int} = 0.15$." [51]

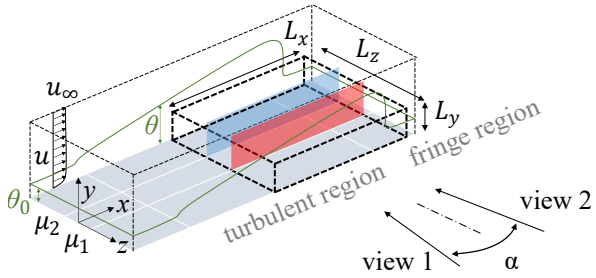

Figure 9.12: "Flow configuration [138] and dual-plane stereoscopic setup. Measurement planes: *red* – front, *blue* – rear." [51]

a random 3D snapshot was considered to prove the DPSA approach for a known velocity field. Figure 9.12 shows the configuration of the turbulent boundary-layer flow in conjunction with the virtual stereoscopic setup and dual-plane illumination. The inflow thickness θ_0 and the free stream velocity u_∞ are used for the normalisation of the quantities. The spatial range of the DNS data spans $30 \times 2.1 \times 3.1$ ($L_x \times L_y \times L_z$), which corresponds to $34 \times 57 \times 41$ data points.

For the virtual image acquisition, a mutual camera angle of 20° is used, where the optical systems of the virtual cameras are identical and satisfy the Scheimpflug-criterion according to Section 9.1. The illumination describes two parallel-aligned light sheets with [index $i = 1, 2$ and] Gaussian intensity profiles $I_i = 1/\sqrt{2\pi\sigma^2}\,\exp\left(-\left(z-\mu_i\right)^2 / \left(2\sigma^2\right)\right)$, where $\mu_i = \pm 1.55\theta_0$ are the spanwise light-sheet coordinates and $4\sigma = 0.078\theta_0 = \delta_l$ specifies the light-sheet widths.

The simulations are carried out with an image resolution of 6400×400 px. The particle densities are selected individually. In accordance with the findings of Section 9.3, particle densities of ≈ 0.02 ppp for CPI and ≈ 0.05 ppp for IPR are used. With regards to DPSPIV, a particle density of 0.05 ppp is specified. It should be noted that the particle density per measurement plane is twice as high for DPSPIV than for DPSA due to the joint image recording in terms of DPSA. For the initiation of the particles, a random generator with uniform distribution is used. As particle image sizes, for DPSA $\mathbf{d}_e = (2.0, 4.0)^{\mathrm{T}}$ px and for DPSPIV $\mathbf{d}_e = (2.3, 2.3)^{\mathrm{T}}$ px are employed. To assess the undisturbed performance

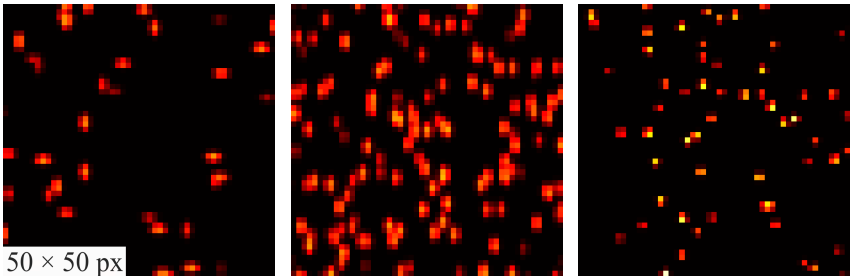

(a) DPSA-CPI (0.02 ppp) $\mathbf{d}_e = (2.0, 4.0)^{\mathrm{T}}$ px

(b) DPSA-IPR (0.05 ppp) $\mathbf{d}_e = (2.0, 4.0)^{\mathrm{T}}$ px

(c) DPSPIV (0.05 ppp) $\mathbf{d}_e = (2.3, 2.3)^{\mathrm{T}}$ px

Figure 9.13: Illustration of the respective particle densities and particle image shapes for the DPSA-CPI, DPSA-IPR and DPSPIV configurations showing sections of the raw images with colour-coded intensities.

of the methods, no additional noise is incorporated. An inter-framing time of $\mathrm{d}t_{PIV} = 7.7 \cdot 10^{-5}\theta_0/u_\infty$ is used. In reference to the light sheet widths, the maximum out-of-plane [...] displacement contributes to quasi no out-of-plane loss." [51] Sections of the "[...] calculated raw images are shown in Figure 9.13 for all tested approaches. The configuration of the experimental setup and imaging are summarised in Table 9.1.

For particle identification, the IPR method is conducted with eight external and six internal iterations. With regard to CPI, the detection of overlapping particles is exclusively based on the geometrical criterion. As threshold, a value of $\epsilon_{geom} = 0.05$ is used, which represents a strict removal of overlapping particles. The selected threshold promotes a more accurate identification of the particles at the cost of the particle identification rate. The identification process is indicated for both methods in Figure 9.14.

For displacement analysis, the PIV evaluation according to Section 9.2.2 is applied. The PIV evaluation is operated with a multi-grid, multi-pass scheme [109, 110, 141] and further window deformation [142]. The final interrogation area size is set based on the number of identified particles, so that the interrogation areas contain an average of about 10 particles each. An overlapping factor of 50% is used. The displacement analysis of the DPSPIV configuration is done by means of a commercial image cross-correlation code from LaVision's DaVis 8.4 software. The respective values

Illumination		
dual-plane distance	Δl	3.11 θ_0
light-sheet width	δ_l	0.078 θ_0
Camera		
image resolution		6400×400 px
interframing time	$\mathrm{d}t_{PIV}$	$7.7 \times 10^{-5}\theta_0/u_\infty$
Imaging		
particle image dimensions		
DPSA	$\mathbf{d}_e$	$(4.0, 2.0)^{\mathrm{T}}$ px
DPSPIV	$\mathbf{d}_e$	$(2.3, 2.3)^{\mathrm{T}}$ px
Optical setup		
mutual camera angle	α	20°

Table 9.1: Specified setup for the assessment of DPSA [51].

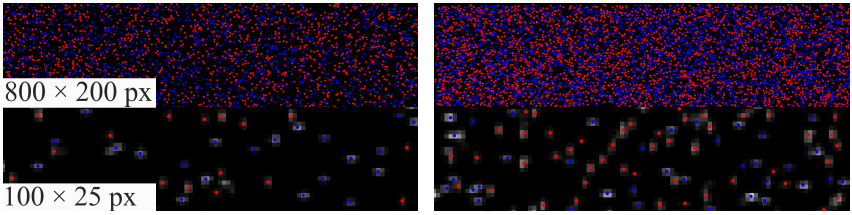

(a) CPI (0.02 ppp) **(b)** IPR (0.05 ppp)

Figure 9.14: Identified particles of the CPI and IPR evaluation [51]: (a) CPI: 72.71% particle identification rate, 0.072 px mean uncertainty of particle localisation ($\epsilon_{geom} = 0.05$, particle density of 0.02 ppp, $\mathbf{d}_e = (2.0, 4.0)^{\mathrm{T}}$ px); (b) IPR: 83.32% particle identification rate, 0.114 px mean uncertainty of particle localisation (particle density of 0.05 ppp, eight external and six internal iterations). *red* dots – front, *blue* dots – rear.

Particle identification	CPI	IPR	
identified particles	36428	104516	
particle identification rate	72.71%	83.32%	
mean uncertainty of particle localisation	0.072 px	0.114 px	
Displacement analysis	DPSA		DPSPIV
	CPI	IPR	
particle density (ppp)	0.02	0.049	0.052
interrogation area grid			
frontal plane	340 × 20	622 × 38	800 × 50
rear plane	340 × 20	622 × 38	800 × 50
interrogation area size (px)			
frontal plane	38 × 40	21 × 21	16 × 16
rear plane	38 × 40	21 × 21	16 × 16
average particles per interrogation area and measurement plane	∼ 10	∼ 10	∼ 13
overlap factor	0.5	0.5	0.5

Table 9.2: Results of the particle identification process and displacement analysis via CPI and IPR [51].

of the used interrogation area sizes and grid sizes are listed in Table 9.2. The reconstruction of the velocity components are calculated based on the stereo-PIV velocity reconstruction [10]. For the transformation from image-plane to object-plane coordinates, the Pinhole-model is used.
The determined velocities for all tested methods (DPSA-CPI, DPSA-IPR, DPSPIV) are shown in Figure 9.15 in comparison to the original DNS data. At first glance, all approaches show good agreement with the DNS data. Both CPI and IPR successfully reconstruct the individual measurement planes, whereby IPR is more accurate. In view of the present case, the results of DPSA is comparable to that of DPSPIV. To evaluate the accuracy of the methods more rigorously, the normalised differences to the DNS results are shown in Figure 9.16. Finally, the desired velocity-gradient information and corresponding uncertainties are given in Figure 9.17, which

in addition to the free stream velocity also uses the boundary layer thickness to normalise the results.
The comparison of the different components as shown in figures 9.15 – 9.17 clearly demonstrate two different levels of accuracy for all methods, while the in-plane velocities and gradients show good agreement, the spanwise (out of plane) components are comprised of considerably higher uncertainties. This comes with no surprise, since the choice of only 20° for the mutual angle between the cameras inherently leads to larger displacement errors for the out-of-plane components.
In accordance with Section 9.3, the IPR method is able to reconstruct particles for high particle densities (cp. Figure 9.14). Despite the fact that the CPI is limited to small particle densities, the flow field shows good agreement, which is also resembled in the comparable uncertainty fields of Figure 9.16. Note, however, that the CPI technique shows a very low mean uncertainty of particle localisation (Table 9.2), which is due to the strong removal of overlapping particles." [51]

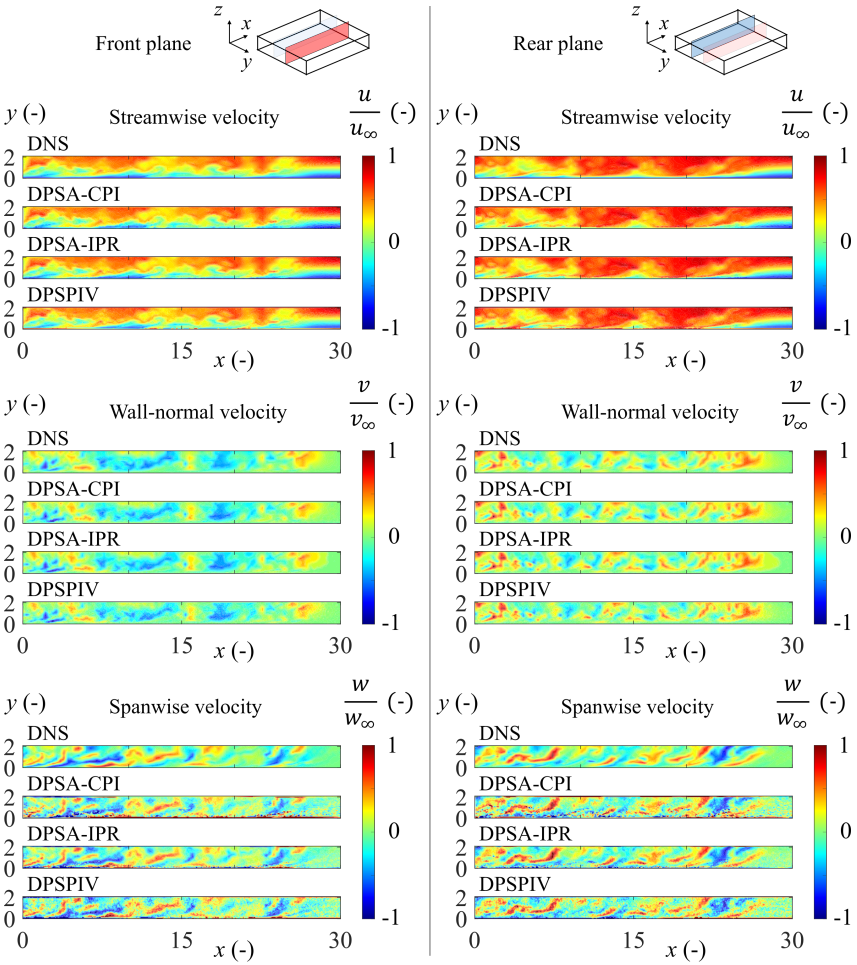

Figure 9.15: "Normalised velocity components of the frontal (left) and rear (right) measurement planes – DNS, DPSA (CPI), DPSA (IPR), DPSPIV (top to bottom)." [51]

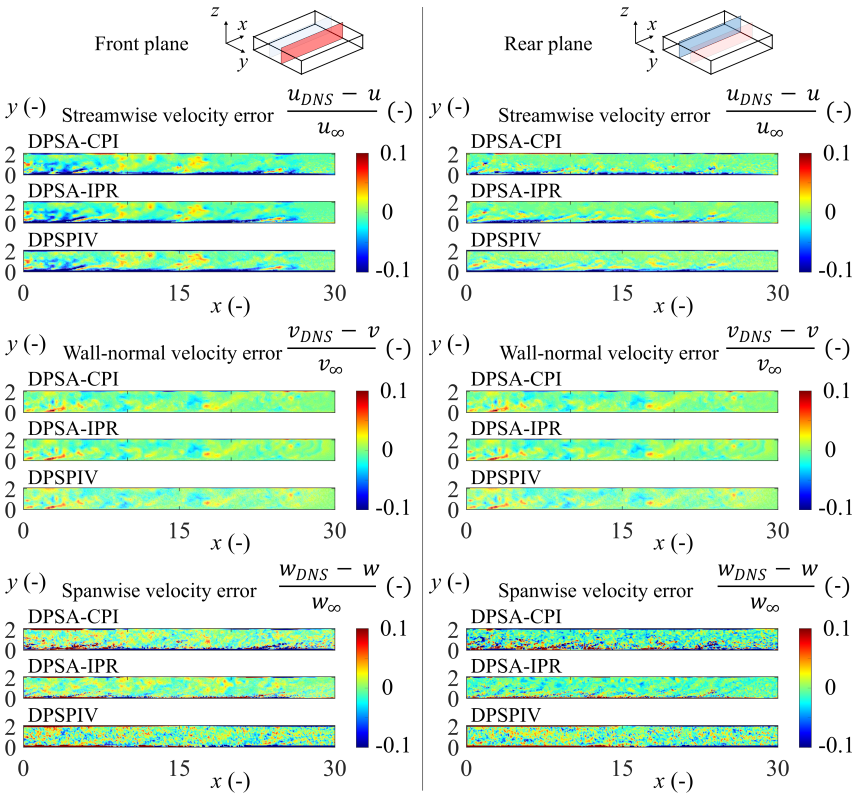

Figure 9.16: "Normalised uncertainties of all velocity components of the frontal (left) and rear (right) measurement planes – DNS, DPSA (CPI), DPSA (IPR), DPSPIV (top to bottom)." [51]

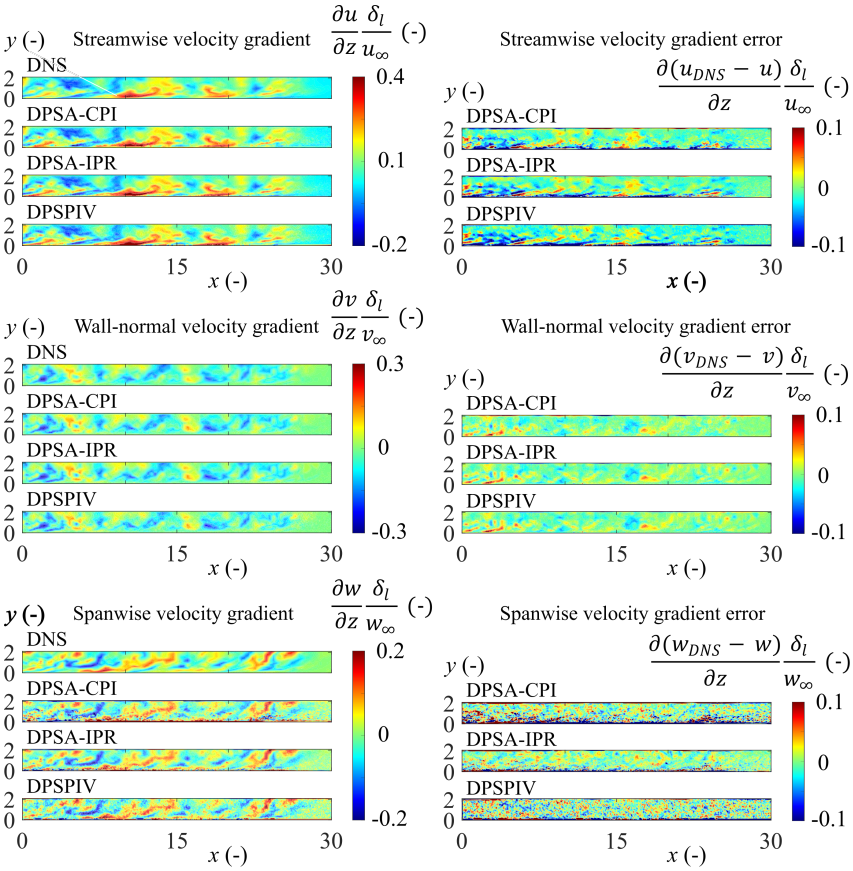

Figure 9.17: "Normalised velocity gradients (left) and corresponding uncertainties (right) of the determined velocities – DNS, DPSA (CPI), DPSA (IPR), DPSPIV (top to bottom)." [51]

9.5 Experimental application of DPSA on spray-induced flow

"As one of the first experimental applications of DPSA, two different experimental configurations are used to illustrate the DPSA approach based on a non-synthetic case. Both experiments are designed to pursue different objectives. The first experiment is a comparison of the Dual-Plane Astigmatism approach with conventional planar PIV. Here, the primary objective is to investigate congruence between both velocimetry techniques in order to validate DPSA experimentally based on a well-known and highly accurate technique. The second experiment is a fully performed DPSA measurement enabling the characterisation of the complete velocity gradient tensor. The experiments are conducted on spray-induced flow." [51] Since the velocimetry of spray-induced flow is subject to low signal-to-noise levels due to background noise, multi-scattering and the use of fluorescent tracer particles and optical filtering, the application is well-suited to investigate the robustness of the DPSA approach.

"For the experiments, the spray-induced flow of a two-hole gasoline direct injection (GDI) research sample is investigated. The experimental setup comprises a stereoscopic setup with dual-plane illumination. The experiments are carried out in an optically accessible chamber [according to Chapter 5]. The cameras are arranged with a mutual angle of about $\alpha = 45°$. As light source, a double cavity Nd:YAG laser with a wavelength of 532 nm is used. [...] The generation of the dual-plane light-sheets is realised by the use of beam splitters, mirrors and a lambda-half plate for beam guidance as shown in Figure 9.18. The lambda-half plate is utilised to adjust the intensity of the individual light sheets. The spacing between the light sheets is specified by the relative position of the traversable mirror and the unifying beam splitter." [51] To achieve a similar grid spacing between the out-of-plane and in-plane directions, a spacing of about $\Delta l = 10$ mm is chosen. In order to introduce astigmatism, a series connection of cylindrical lenses with focal lengths of 300 mm and -300 mm is used. The magnitude of astigmatism is controlled by the lenses' spacing. "The experiments are carried out at an injection pressure of $p_{inj} = 100$ bar, an ambient gas pressure of $p_\infty = 1$ bar, and a fuel and gas temperature of $T_{fuel} = 25°\text{C}$ and $T_\infty = 25°\text{C}$. Gasoline is used as fuel. The specifications of the illumination and image acquisition are summarised in Table 9.3." [51]

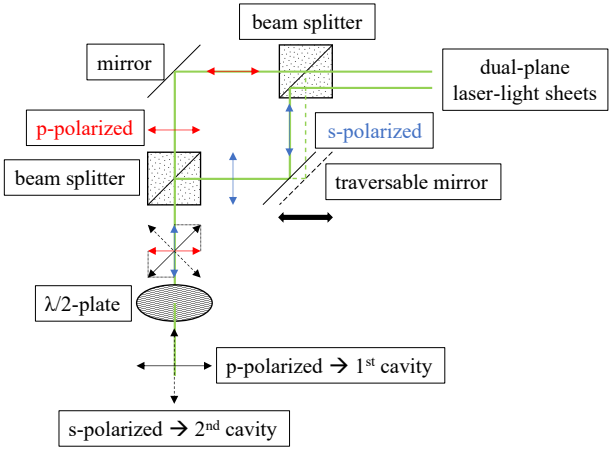

Figure 9.18: "Schematic illustration of the optical system used for the generation and control of the dual-plane laser-light sheets." [51]

Illumination		
wavelength	λ	$532 \cdot 10^{-9} m$
dual-plane spacing	Δl	10 mm
light-sheet width	δ_l	0.2 mm
Image acquisition		
pixel size		28 μm
resolution		1280 × 860 px
acquisition frequency	f_{acq}	5 kHz
interframing time	$\mathrm{d}t_{PIV}$	80 μs

Table 9.3: Configuration of the illumination and image acquisition [51].

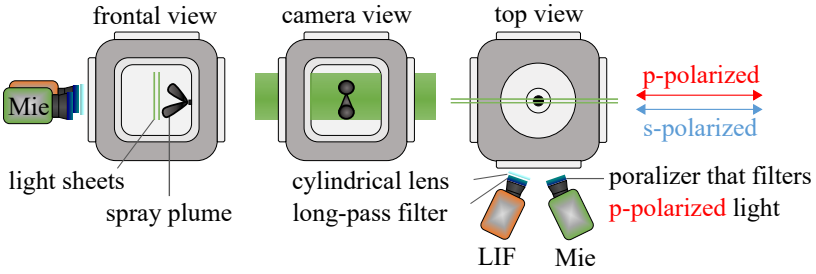

Figure 9.19: Experimental setup used for the comparison between Dual-Plane Astigmatism (DPA) and conventional PIV [51].

9.5.1 Comparison of Dual-Plane Astigmatism (DPA) and standard 2D2C PIV

"For the comparison of the Dual-Plane Astigmatism (DPA) approach and conventional PIV, two cameras are supplied with different optics. The camera used for DPA is equipped with cylindrical lenses whereas the other camera operates with a polariser (see Figure 9.19). The function of the polariser is to provide an exclusive contemplation of a single measurement plane while filtering out the particle signal of the second measurement plane. Regarding different requirements on particle density, the introduction of fluorescent tracer particles and the presence of polydisperse particle seeding is utilised to reduce the number of effectively contributing particles in case of DPA by exploiting the approximately quadratic dependence of fluorescent emission with regard to droplet diameter. As tracer medium, a solution of propylene carbonate and fluorescent DCM dye [19] is used. For optical filtering, the objective is equipped with an OD4 long-pass filter with a cut-off wavelength of 600 nm. In contrast to the DPA configuration, the second camera, which is used for conventional PIV, is operated with Mie scattering. Due to the higher signal-to-noise ratio of Mie scattering, the image plane particle density is higher for the PIV case than for the DPA case. In view of the signal-to-noise ratio, which is interfered by light scattering at the spray, the velocimetry of spray-induced flow using Mie scattering is limited to diluted spray areas.
To provide the examination of typical flow structures such as displacement

and entrainment flow [50, 121], the injector is mounted on the opposite side of the chamber [...] so that the spray propagation is directed towards the measurement planes [(see Figure 5.1, side position)]. The present examination addresses the displacement flow of a single spray plume.
The displacement analysis is conducted according to Section 9.2.2. A multi-grid, multi-pass [109, 110, 141] evaluation scheme with window deformation [142] is used. For the specification of the interrogation area size, an average particle number of 15 particles per interrogation area is considered. For particle identification, the CPI method is applied since it provides a high flexibility with regards to changing particle image sizes and dimensions as well as optical aberrations. For the image cross-correlation, horizontally and vertically aligned synthetic particle images with particle image dimensions of $\mathbf{d}_e = (8, 4)^{\mathrm{T}}$ px are used. For the detection of overlapping particles, the geometric criterion is used. To enhance the rate of particle identification, a partial particle overlapping is considered by using a threshold of $\epsilon_{geom} = 0.2$. The conventional PIV evaluation is performed by means of LaVision's DaVis 8.4. For both DPA and PIV evaluation, spurious vectors are identified and removed by a normalised median filter (3×3 neighbourhood) [108] in order to promote data validity. In Table 9.4, the specifics of the optical setup and displacement analysis are listed. In Figure 9.20, the resulting velocity fields of the DPA and PIV displacement analysis are shown for an image section. For both techniques, the displacement flow next to the penetrating spray is clearly visible. Despite certain differences, the structure of the flow fields shows good agreement. Potential reasons for deviations are due to differences in particle densities, perspective, particle image size and processing. In comparison, the particle image size regarding DPA is substantially larger than that of the PIV imaging. Recall that the fundamental need for particle identification generally makes DPA more susceptible to optical aberrations and particle image characteristics, as elaborated in Section 9.3." [51]

9.5.2 Velocimetry of spray-induced flow by means of DPSA

"For the application of DPSA on spray-induced flow, a central top mounted injector position is used (see Figure 9.21). The orientation of the injector

PIV	DPA	PIV
interrogation area grid	19×14	19×14
overlap factor	0.5	0.5
particle image dimensions	$\mathbf{d}_e = (8, 4)^{\mathrm{T}}$ px	$\mathbf{d}_e = (2.5, 2.5)^{\mathrm{T}}$ px
Particle seeding		
seeding particle		DCM and propylene carbonate
particle diameter	d_p	$\approx 1\ \mu$m
Optical configuration		
focal lengths	f_i	100 mm
magnification	M_i	0.34
f-numbers	$f_\#$	11 (DPA), 4 (PIV)
field of view		102×68 mm^2
mutual camera angle	α	$\sim 45°$

Table 9.4: Setup and evaluation of the DPA and PIV experiment [51].

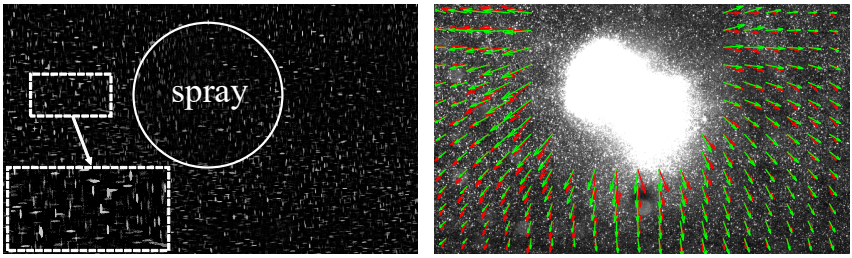

(a) **(b)**

Figure 9.20: "Simultaneous DPA and planar PIV measurement. Left: sliding average (8×8 px) of the DPA image with a zoomed in section showing the horizontally and vertically aligned particle images, right: vector fields of the s-polarised (frontal) plane superimposed to a spray plume; *red* – frontal DPA plane, *green* – standard PIV." [51]

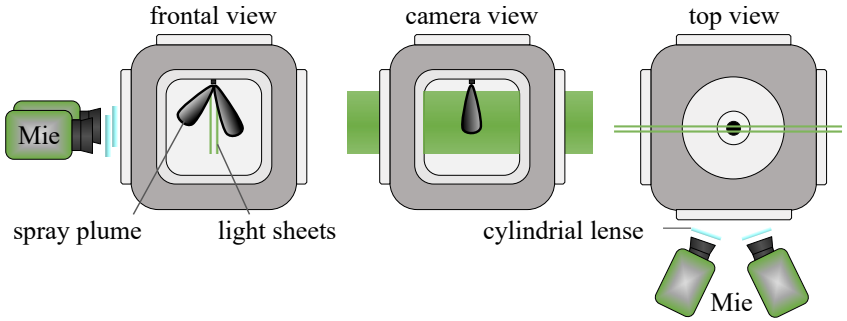

Figure 9.21: "Experimental setup: stereoscopic arrangement with DPSA configuration; dual-plane illumination and cylindrical lenses for astigmatism-based depth codification." [51]

allows the transmission of the light sheets between the spray plumes without spray-light-sheet intersection, thus allowing the exploitation of Mie scattering. The setup is primarily reasoned by the necessity to avoid strong beam deformation since the concept of DPSA relies on discrete planar measurement domains. Furthermore, the use of Mie scattering generally promotes higher signal-to-noise ratios, while avoiding spray-light-sheet intersection.

The processing of the images comprises a separation of the measurement planes, displacement analysis and a determination of the out-of-plane gradients. For the separation of measurement planes, CPI is used due to its robustness and flexibility with respect to background noise, optical aberrations and inconsistent particle images. For the displacement analysis, particle tracking (PTV) in combination with PIV evaluation is carried out. The PIV result serves as an initial estimation for a nearest neighbour PTV approach. The use of PTV is mainly justified by an increased vector field resolution, which is generally aspired for detailed flow characterisation. For the calculation of the out-of-plane gradients, the PTV result is mapped on a regular grid for a simplified calculation. In Table 9.5, details about the optical setup and the DPSA processing are listed. Figure 9.22 illustrates the injection process for three consecutive time steps. Although the spray does not intersect with the dual-plane light-sheets, the spray is clearly visible due to the multiple scattering, especially in the area of dense

PIV		
interrogation area grid		50×42
overlap factor		0.5
particle per pixel		~ 0.01 ppp
particle image dimensions	$\mathbf{d}_e$	$(8, 4)^{\mathrm{T}}$ px
Particle seeding		
seeding particle		DEHS
particle diameter	d_p	$\sim 1\ \mu m$
Optical setup		
focal lengths	f_i	100 mm
magnification	M_i	0.34
f-number	$f_\#$	16
field of view		102×68 mm^2
mutual camera angle	α	$\sim 45°$
light-sheet thickness	δ_l	~ 0.2 mm
dual-plane spacing	Δl	5 mm

Table 9.5: Setup and evaluation of the DPSA experiment [51].

spray. In addition, multiple scattering and reflections on the glass windows illuminate the interior of the chamber. Overall, a low signal-to-noise ratio is observed. Only a certain fraction of particles is clearly visible." [51] A DPSA evaluation is carried out at a time $t_3 = 6$ ms after SOI (right-hand side of Figure 9.22). "Despite the low signal-to-noise ratio, the CPI method identifies a particle number that corresponds to an approximate particle density of 0.01 ppp on average. The ratio of particle allocation regarding the measurement planes ranges between $50 \pm 5\%$. Figures 9.23 – 9.25 show the results of the particle identification and displacement analysis for the indicated image section." [51]

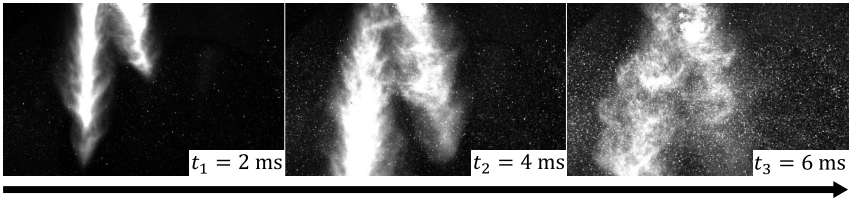

Figure 9.22: Course of the injection event under investigation [51].

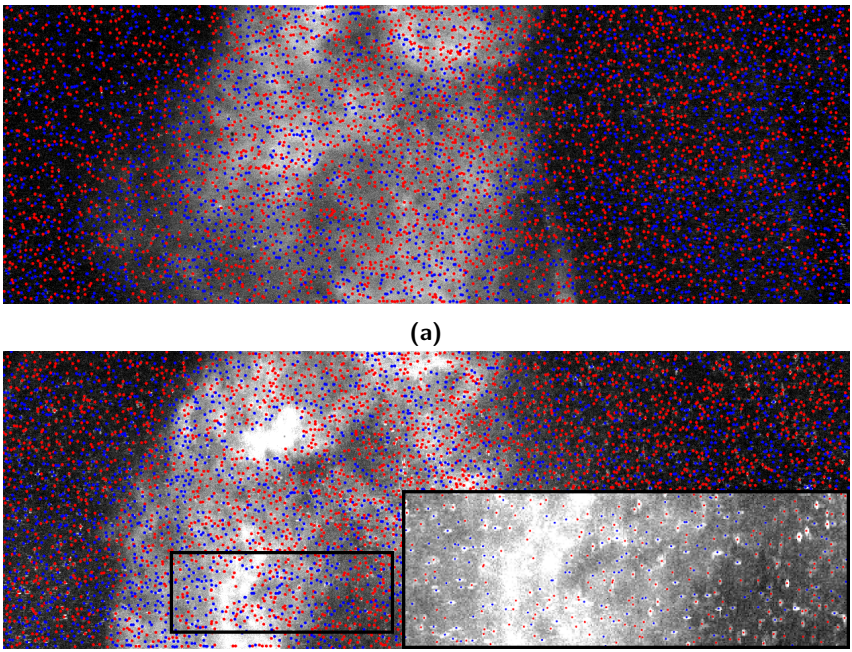

Figure 9.23: "Identified particles at the second time frame. (a) Left-hand-side camera, b) right-hand-side camera; red dots – frontal measurement plane, blue dots – rear measurement plane. Background: visible spray plumes and chamber interior; oversaturation at some spray plume areas. The indicated rectangle is used to support the following discussion on the data-processing steps." [51]

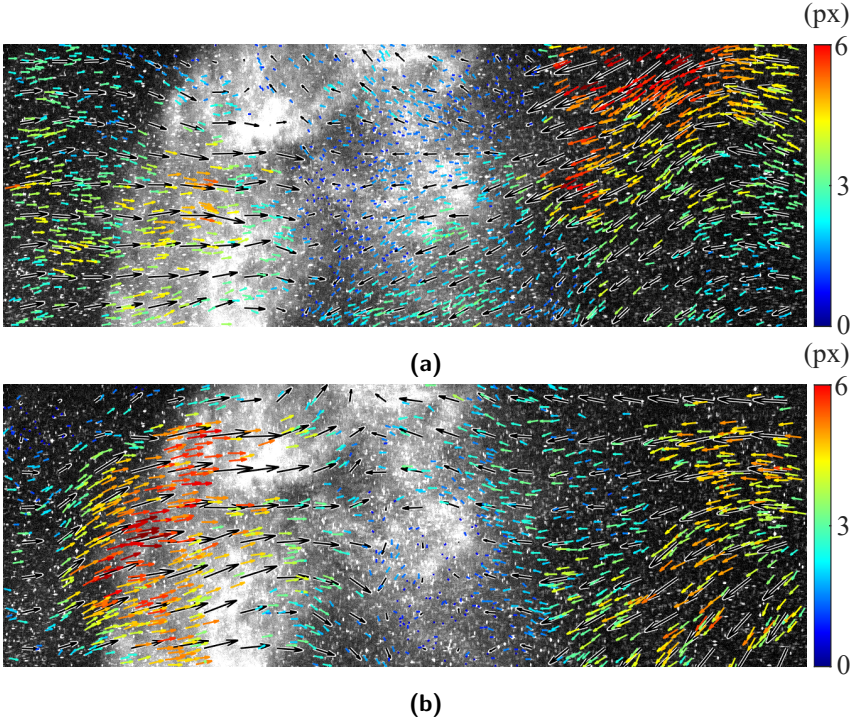

Figure 9.24: "Image-plane displacement analysis concerning the right-hand-side camera. Displacements in pixels. (a) frontal plane, (b) rear plane; black vectors – PIV, coloured vectors – PTV (PIV result as estimation for nearest neighbour PTV approach). For better differentiation, the PIV vectors are double-length compared to the PTV vectors; background – raw image." [51]

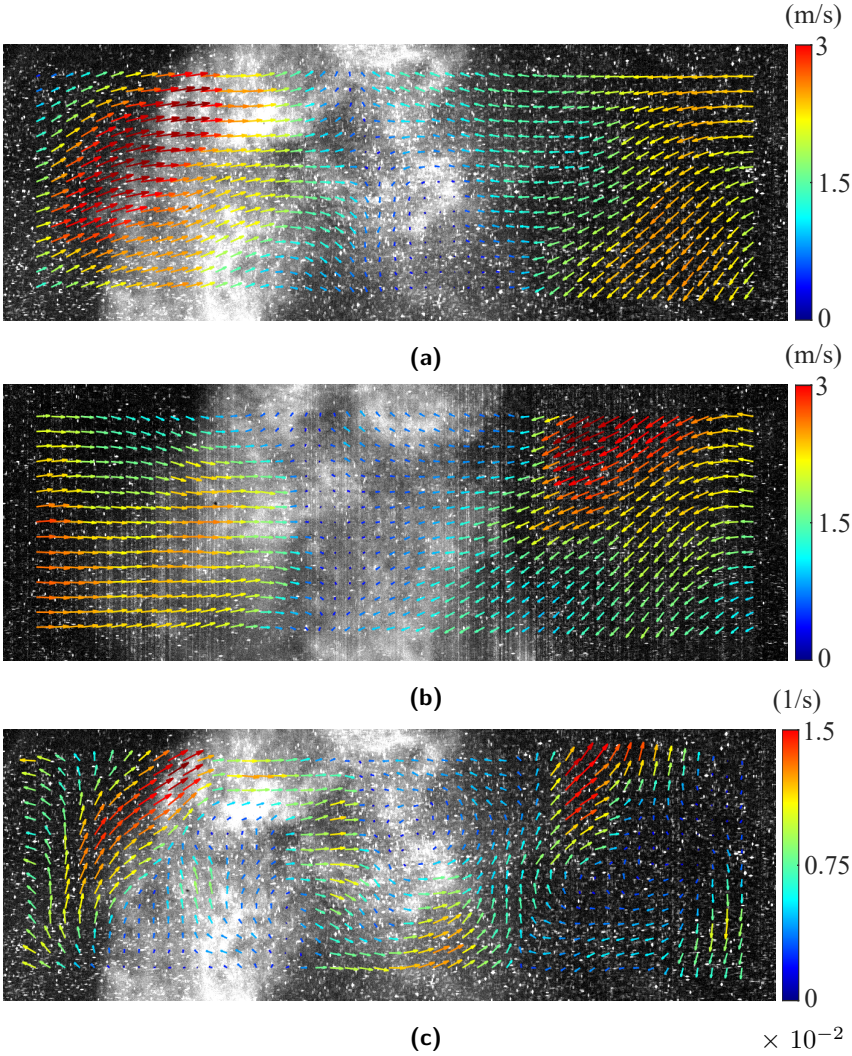

Figure 9.25: "Obtained velocity fields and out-of-plane gradients. (a) $(u_1, u_2)^{\mathrm{T}}|_{front}$ – front plane, (b) $(u_1, u_2)^{\mathrm{T}}|_{rear}$ – rear plane, (c) out-of-plane gradient $(\partial u/\partial x_3, \partial u_2/\partial x_3)^{\mathrm{T}}$. Colour coding – magnitude. Background: raw image of the right-hand-side camera." [51]

9.6 Discussion

"An essential aspect in DPSA is the accurate identification of particles in the presence of particle overlapping. Particle overlapping is regarded as limiting factor for the application on dense particle fields. However, even for low to moderate particle densities, particle overlapping intrinsically occurs due to the joint imaging of consecutive measurement planes. Representing a simple method, the cross-correlation-based approach (CPI) allows [for] the accurate identification of particle image shapes for non-overlapping particles. Due to its ability of differentiating principal particle image shapes, the approach is robust against varying particle image shapes and optical aberrations. The allocation of particles does not require an elaborate calibration. Note, however, that with regards to accuracy of particle identification and allocation, the detection of particle overlapping is crucial. Three different criteria [...]" [51] are proposed. "A rather simple but powerful one is the criterion based on geometric particle image intersection while considering particle location and orientation. To account for the corresponding particle image shapes and orientations, the criterion uses a priori information, which stem from the particle allocation process. The approach is principally prone to misallocation. However, for low to moderate particle densities and sufficiently differentiating particle image shapes, the criterion operates robust. The intensity-based criterion equivalently requires information about the particle image shape and orientation. The particular strength of the approach in contrast to the other criteria is the ability to address highly merging particles. A simple criterion for the detection of particle overlapping is the ratio of the cross-correlation peaks. However, the determination of the actual peak ratio suffers from the discretisation of the particle images, in particular for small particle images. Furthermore, the criterion is prone to neighbouring particles, which may interfere with the cross-correlation of the non-matching particle image. The criterion is specifically viable for low particle densities, moderate to high particle image sizes and markedly differentiating particle image shapes.

In the present work, an adapted version of the IPR algorithm was implemented using a single perspective. Despite of imperfect information and potential ambiguity, reasonable results are obtained for even highly dense particle fields. For non-uniform particle images, in contrast, the IPR

technique becomes increasingly complex. Likewise, significant amounts of background noise or similar signal-to-noise ratios would require further image pre-processing steps for the IPR, which is not mandatory for CPI. Since such optimisation efforts are beyond the purpose of the present work, the IPR was only evaluated for synthetic images, which however indicates that the IPR method appears generally promising for the processing of DPSA images.

Due to its restriction to non-overlapping particles, the CPI approach is limited to low to moderate particle densities. High deformation rates, big particle image sizes and high particle densities reduce the achievable particle identification rate. However, the analysis shows a quite stable performance of particle allocation in concern of noise and particle image size. In contrast, the particle identification rate of the IPR method decreases. Since the IPR method is an intensity-based approach, the technique intrinsically suffers from weak signal-to-noise ratio. However, the capability of the IPR method in terms of particle identification and allocation is significantly stronger than the performance of the CPI approach, especially for higher particle densities, which are generally aspired for the investigation of detailed flow fields and velocimetry-based pressure evaluation.

To increase the performance of the implemented IPR method and the CPI technique, an utilisation of the different camera perspectives is conceivable. Traditionally, the IPR uses multiple perspectives for the particle reconstruction in a volumetric domain. Since the light-sheets feature a certain thickness, an adaptation in DPSA would require the use of voxels instead of pixels. In terms of the CPI method, the use of multiple perspectives allows a mutual particle cross-check for the reconstruction of overlapping particles. In general, the use of time-resolved particle tracking is considered as a viable approach to improve the capability of particle identification and enhance the range of applicable particle densities. Existing and highly-performant techniques such as 3D-PTV [92], tomo-PIV [49] and "Shake-The-Box" STB [97, 143] are generally conceivable for the processing of DPSA images and are believed to improve the overall performance of the DPSA approach substantially.

The location-based PIV evaluation [(see Section 9.2.2)] shows an accurate analysis of particle displacement as well as a fast and simple computation, which stems from the summation of bivariate normal distributions of particle pairs. The approach intrinsically weights the contributions of

the particles equally. Hence, no additional particle weighting is required. Further, the standard deviation of the bivariate normal distributions acts as a filter concerning the in-plane gradients. Displacements, which exceed the ensemble-averaged displacement by more than six times the standard deviation, are filtered out and do not contribute. Generally, the use of smaller distributions tends to have less overlap than wider distributions. For the formation of a global peak, a certain overlap is required. If no overlap is present, no unique solution is obtained. On the other hand, wider distributions principally lead to an attenuation of the convolution peak and thus to a higher uncertainty concerning noise, particle overlapping and particle localisation. The combination of window deformation and the use of relatively small standard deviations is sought to minimise uncertainty. To ensure further robustness, it is recommended to use adaptive standard deviations beginning with higher values that trend to smaller values. Techniques such as multi-grid, multi-pass [109, 110, 141] and window deformation [142] were adapted to the location-based PIV evaluation. The implementation of window deformation is straightforward, simple and easy to extend to higher order approximation.

As an alternative to location-based PIV, conventional image cross-correlation can also be adapted for DPSA processing. Hereby, synthetic images have to be generated according to the identified particles. The approach enables the use of existing PIV algorithms and routines. However, the particle detection and assignment process, which is considered as the major part of DPSA processing, is still required. As drawback, the generation of synthetic particle images and the subsequent image cross-correlation feature additional uncertainty. In the context of DPSA, the location-based PIV evaluation is more accurate than the image cross-correlation of synthetic images.

The capability of the DPSA approach was demonstrated by the investigation of a synthetic flow field and the comparison with a dual-plane stereoscopic PIV approach. The results show a good agreement with respect to the out-of-plane gradient determination. In accordance to the performance assessment, the IPR method was able to identify a high number of particles, whereas the CPI is limited to non-overlapping particles. However, the CPI results are highly accurate and furthermore, the computational effort is considerably lower than for the IPR technique. In general, a high particle identification rate is aspired for the displacement analysis and particularly for a PTV evaluation, since the detection of

particle pairs requires the identification of the particles for both time steps. For illustration, an identification rate of 80% leads to a mean detection rate of 64%. Despite the joint recording of multiple measurement planes, the DPSA approach provides a high in-plane resolution in comparison to techniques such as APTV [93, 94], defocusing PIV [95] and XPIV [91]. This is mainly due to the concept of discrete depth levels, which allows the use of compact particle images.

The investigation of spray-induced flow demonstrates the applicability of CPI on data with a significantly low signal-to-noise ratio. The CPI method is able to identify a substantial number of particles. The peak detection based on the image cross-correlation proves to be a viable strategy to enhance the robustness of particle identification and allocation. However, regarding particle localisation the approach suffers from low particle image discretisation. In accordance to the performance assessment, the combination of attained particle image size, particle image deformation and effective particle density shows a low tendency of particle overlapping. Despite varying particle image dimensions, the adjusted particle deformation ratio of about $r_d = 0.5$ provides a sufficient differentiation of particle image shapes. Apart from the low signal-to-noise ratio, the configuration of the optical setup is considered appropriate with regard to the CPI evaluation.

The PIV evaluation shows a marked difference between the displacement fields of the individual measurement planes. The reconstructed velocity fields characterise an entrainment flow, which is typical for spray-induced flow and indicates reasonable results. Due to its statistical approach, the PIV evaluation features a certain robustness with respect to uncertainty, false detection and misallocation. The use of an average particle count of 15 particles per interrogation area shows reliable results. With regard to general recommendations [106], the relative increase in particle numbers is comparatively moderate. Contrarily, the increase in robustness and accuracy is accompanied by a reduction in vector field resolution. The PTV analysis confirms the applicability of PIV evaluation. However, only a small proportion of particle pairs are identified. The uncertainty of particle identification and particle allocation is regarded as major aspect for the low detection rate. In addition, the resolution of the PIV displacement fields may be too coarse to resolve small-scale structures and serve as feasible estimates for the PTV analysis. An adjustment of the search radius increased the number of identified particle pairs, however, the results become more and more noisy.

The particle image shapes are generally not restricted to horizontally and vertically aligned particle images since the identification and assignment of particles relies on the principal difference of the particle image shapes. Consequently, the use of a combination of circular and elliptical particle image shapes is also feasible to further increase the compactness of particle images and therefore the range of applicable particle densities. For the codification of depth, the DPSA approach generally requires only a single optical system that incorporates astigmatism.
As a general note on possible extensions of the introduced method, the DPSA approach can be extended by further measurement planes in principal. Theoretically, an extension would provide a finer and more accurate out-of-plane gradient determination. In addition, it enables the application of a central differencing scheme and the determination of the second order partial derivative. However, there are some drawbacks, which may limit the scope of application. Since the corresponding particle image shapes of the measurement planes have to be unique, the incorporation of additional measurement planes leads to a broader spectrum of particle image sizes and deformations. This effort is inherently accompanied by a higher tendency of particle overlapping, which relates to a smaller range of applicable particle densities and lower in-plane resolutions." [51]
Generally, "[...] the measurement planes do not require a parallel orientation in principle. However, the out-of-focus effect in conjunction with the optical system limits the range of applicable configurations. An unambiguous allocation of particles is constrained to non-crossing measurement plane domains." [51]

9.7 Concluding remarks

With the introduction of DPSA, a novel approach for the simultaneous velocimetry in two successive planar measurement domains was developed that allows the characterisation of the full velocity gradient tensor using a stereoscopic PIV setup. "The DPSA approach is a hybrid technique, which combines the concepts of APTV [94] and dual-plane stereo-PIV (DPSPIV) [90]. It represents an attractive alternative to existing measurement techniques due to its particular balance between low measurement expense and utility. In contrast to other (quasi-) volumetric velocimetry

techniques, the DPSA approach requires a low amount of measurement equipment consisting of two cameras, one light source and few supplementary optical components. The DPSA approach features a comparatively high in-plane resolution and robustness due to its measurement in planar domains. [...] The DPSA approach is particularly attractive for applications with limited optical accessibility, low signal-to-noise ratio and limited access to cost-intensive measurement equipment. It extends the scope of applications especially for rough measurement conditions and provides quasi-volumetric velocimetry (2.5D3C) for a comparatively low budget. The characterisation of the full velocity gradient tensor enables the evaluation of [...] instantaneous pressure fields [...]." [51] The DPSA technique was successfully demonstrated on synthetic and experimental data showing good and promising results. The developed methods as well as the findings from the investigations serve as an excellent basis for future spray investigations, especially for the study of singular spray phenomena and shot-to-shot variations, which so far required the use of more measurement equipment.

The DPSA approach is well-suited for the analysis of spray transport. However, it shall be noted, that the experimental application of DPSA requires a particular precise design of the optical setup, particle seeding and illumination, as the attainable accuracy, robustness and velocity field resolution largely depends on the quality of the particle imaging (particle overlapping, particle identification, particle allocation).

10 Pressure evaluation by means of Physics-Informed Neural Networks (PINNs)

As current velocimetry/technology is not able to capture the gas flow in dense spray regions of GDI sprays, the use of conventional pressure from PIV is so far limited to the area of the surrounding gas flow and dilute spray regions. To date, a velocimetry in dense spray regions is only conceivable for converged/aligned spray gas flows by utilising the signal of the liquid spray for displacement analysis. This, however, usually refers to the later stage of spray transport. During the period of intense spray-gas interaction and momentum exchange, the velocimetry and pressure evaluation is yet not feasible, thus limiting the analysis of spray transport and spray-induced flow to a certain degree.

In the field of deep learning, recently a promising approach, referred to as physics-informed neural networks (PINNs) [52, 53], was introduced, which combines the strengths of neural networks and data-driven modelling. Neural networks are known as universal approximators of highly non-linear functions, which are able to generalise tasks beyond the limits of trained data. While conventional artificial neural networks (ANNs) usually rely on a rather large amount of training data, PINNs drastically reduce the required data by considering additional a priori information such as laws of physics, given models or empirical correlations. In the pioneering works of Raissi *et al.* [52, 53] and more recently in Raissi *et al.* [144, 145], Karniadakis *et al.* [146] and Cai *et al.* [147], the capabilities of PINNs were impressively demonstrated for various engineering tasks including fluid mechanical problems, where pressure and velocity fields as well as model parameters such as dynamic viscosity are accurately obtained, even in hidden flow regimes, where no or sparse velocity data is available.

Given its great potential in terms of accuracy, generalisation and modelling, in the framework of the present thesis, the concept of physics-informed neural networks was transferred to velocimetry-based pressure evaluation of spray-induced flow. In this chapter, the developed architecture and methodology for PINN-based pressure evaluation is presented and applied to experimental data of a contracting GDI multi-hole spray to demonstrate its performance and capabilities and to gain further insight into the nature of spray transport and spray-gas interaction. For validation and assessment, the results of PINN-based pressure evaluation are compared with conventional pressure from PIV evaluation.
For the description of neural networks, a nomenclature based on the course of Amini & Soleimany [148] was adopted. In this chapter, no Einstein summation convention is used except for the equations of fluid mechanics (modelling equations in Section 10.2.1).

10.1 Artificial Neural Networks (ANNs)

Artificial neural networks (ANNs) [149] are computational models that consist of several connected elements ,referred to as neurons, that receive, process and transmit information based on their predefined weights and activation functions as illustrated in Figure 10.1. As fundamental building block, the neuron is described by a set of mathematical operations. The output of a neuron is given by

$$\hat{y} = a\left(w_0 + \sum_{j=1}^{N_0} x_j w_j\right) \tag{10.1}$$

where w_j are weighting factors (w_0 represents a bias), x_j are inputs, N_0 is the number of inputs and a is an activation function.
In the field of deep learning, several different types, architectures and structures of ANNs exist. In Figure 10.2, a deep neural network consisting of multiple, successive layers of input, output and hidden nodes/neurons is shown. The information is passed from layer to layer in one direction (feedforward), whereby in the present example each node of a layer is connected to each node of the preceding and following layer. Such a structure is referred to as dense neural network.

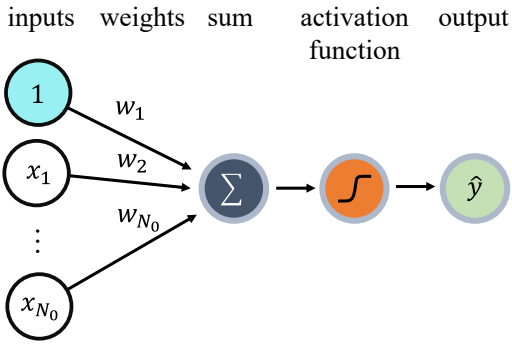

Figure 10.1: Schematic representation of a single artificial neuron.

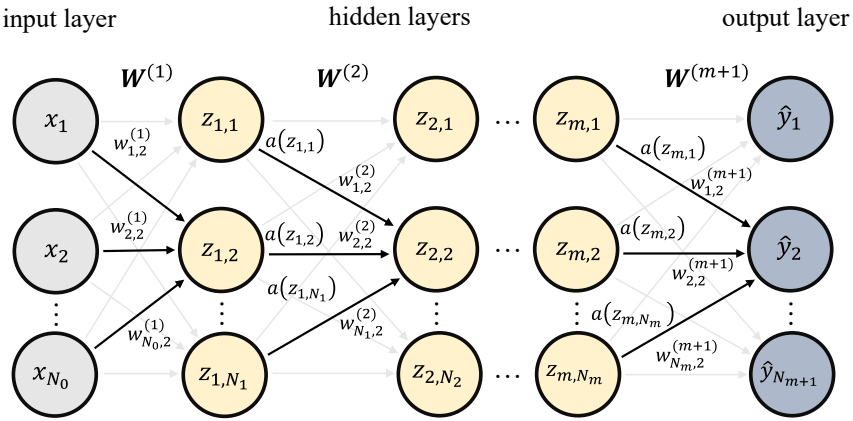

Figure 10.2: Structure of a dense deep neural network composed of multiple, successive layers of input, output and hidden layers.

The output of the neural network is determined by its structure and definition of the activation functions and weights. It is given by

$$\hat{y}_i = a\left(w_{0,i}^{(m+1)} + \sum_{j=1}^{N_m} a\left(z_{m,j}\right) w_{j,i}^{(m+1)}\right) \tag{10.2}$$

with

$$\begin{aligned} i &= 1, 2, \cdots, N_{m+1}, \\ z_{k,i} &= w_{0,i}^{(k)} + \sum_{j=1}^{N_{k-1}} a\left(z_{k-1,j}\right) w_{j,i}^{(k)}, \\ z_{1,i} &= w_{0,i}^{(1)} + \sum_{j=1}^{N_0} a\left(x_j\right) w_{j,i}^{(1)}, \end{aligned}$$

where m is the number of hidden layers, N_0 is the number of inputs, N_k is the number of neurons in layer k and N_{m+1} is the number of outputs. The training of ANNs describes the process of adapting the weighting factors based on available information/data to optimise the performance of the model. This is generally done by minimising or maximising an objective function

$$L\left(\mathbf{W}\right) = L\left(\hat{\mathbf{y}}\left(\mathbf{x}, \mathbf{W}\right), \mathbf{y}\right) \tag{10.3}$$

with

$$\mathbf{x} = \left(x_1, \cdots, x_{N_0}\right)^{\mathbf{T}},\ \mathbf{y} = \left(y_1, \cdots, y_{N_{m+1}}\right)^{\mathbf{T}}\ \hat{\mathbf{y}} = \left(\hat{y}_1, \cdots, \hat{y}_{N_{m+1}},\right)^{\mathbf{T}},$$

$$\mathbf{W} = \left(\mathbf{W}^{(1)}, \cdots, \mathbf{W}^{(m+1)}\right),\ \mathbf{W}^{(k)} = \begin{pmatrix} w_{1,1}^{(k)} & \cdots & w_{1,N_k}^{(k)} \\ \vdots & \ddots & \vdots \\ w_{N_{k-1},1}^{(k)} & \cdots & w_{N_{k-1},N_k}^{(k)} \end{pmatrix},$$

that characterises the quality of a prediction $\hat{\mathbf{y}}\left(\mathbf{x}, \mathbf{W}\right)$ with respect to a known solution $\mathbf{y}\left(\mathbf{x}\right)$. In order to minimise or maximise the objective function, gradient-based methods are generally used. Their principle is based on the iterative approximation of a global minimum or maximum by using the local gradient $\operatorname{grad}\left(L\left(\mathbf{W}\right)\right)$ for the adaptation of the weights

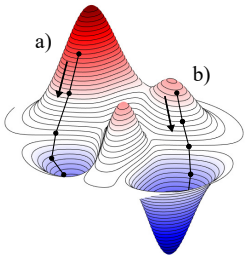

Figure 10.3: Optimisation process using a gradient descent method [149]. The algorithm advances iteratively based on the steepest local descent.

given by $\mathbf{W}_{i+1} = \mathbf{W}_i \pm \zeta \operatorname{grad}(L(\mathbf{W}_i))$, where ζ is a factor that describes the learning rate. For the computation of the gradient, the concept of neural networks allows the use of automatic differentiation [150]. Automatic differentiation is a set of techniques which provides numerical evaluation of derivatives at machine precision by utilising symbolic rules for differentiation. In Figure 10.3, the optimisation process of an objective function is schematically shown using a gradient descent method [149]. Starting from a point of initialisation, the weights are gradually adapted such that the objective function minimises. So far, several strategies were introduced to enhance the performance, robustness and computation expense of the optimisation process. For more detailed information, the reader is referred to the literature [148, 149].

10.2 Methodology of velocimetry-based pressure evaluation by means of PINN

Physics-informed neural networks (PINNs) [52, 53] are data-driven models that provide the solution to partial differential equations (PDEs) by the guidance of data and modelling. The principle is based on the definition of specific objective functions that encode any prior information of PDEs, modelling equations and data.
In the following, a physics-informed neural network architecture is presented that is designed to approximate the solutions of the velocity and pressure fields

of spray-induced flow. It shall be noted that the introduced PINN-architecture and methodology is also applicable to other types of flows.

10.2.1 Architecture for PINN-based pressure evaluation

In continuation to previous spray-induced flow modelling the statistical approach based on URANS and ensemble averaging is adopted to PINN-based pressure evaluation. The incompressible Reynolds-averaged equations for mass and momentum conservation are used as regularising model information. The equations are formulated in two-dimensional space, since the flow under investigation describes a statistically symmetric problem with virtually no out-of-plane velocities $\overline{u}_3 = 0$ and gradients $\partial\overline{(\cdot)}/\partial x_3 = 0$. Due to small Mach numbers ($Ma < 0.2$), density fluctuations are assumed to be negligible $\rho' = 0$. According to the scale and sensitivity analysis of the given problem in Section 6.4, the effect of the Reynolds stresses is regarded as rather moderate with respect to the present case of spray-induced flow evaluation as a late stage spray transport with reduced momentum exchange between spray and ambient gas is examined. Consequently, the Reynolds stresses are not considered in the present evaluation to avoid superfluous computational effort. Note however, that inclusion of the Reynolds stresses is principally conceivable if the given problem at hand requires consideration of turbulent fluctuations. The modelling equations used are given by

$$e_1 \quad : \quad \frac{\partial \overline{u}_i}{\partial x_i} = 0 \tag{10.4}$$

$$e_{2,i} \quad : \quad \rho\left(\frac{\partial \overline{u}_i}{\partial t} + \overline{u}_j \frac{\partial \overline{u}_i}{\partial x_j}\right) + \frac{\partial \overline{p}}{\partial x_i} - \frac{\partial}{\partial x_j}\left[\mu\left(\frac{\partial \overline{u}_i}{\partial x_j} + \frac{\partial \overline{u}_j}{\partial x_i}\right)\right] - \rho\overline{f}_i = 0 \tag{10.5}$$

with $i, j = 1, 2$, where $(x_1, x_2, t)^{\mathrm{T}} \in \Psi \in \mathbb{R}^3$ and Ψ is the domain of evaluation/training. Note that for equations 10.4 and 10.5, the Einstein summation convention applies.

Accordingly, for PINN-based pressure evaluation, a specific objective function L was designed and used to train a dense neural network (see Figure 10.4) consisting of three input (x_1, x_2, t) and three output nodes

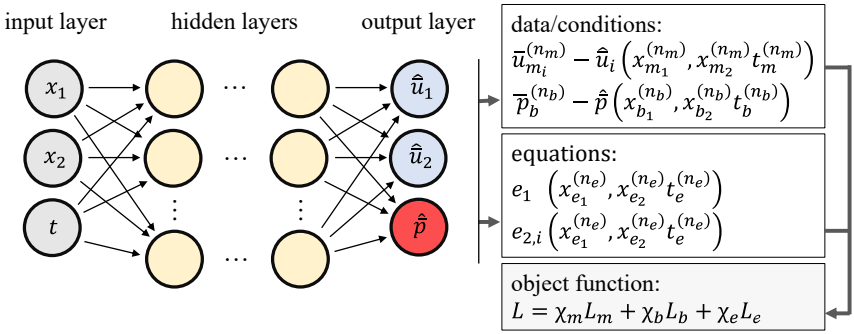

Figure 10.4: Architecture of the physics-informed neural network used for the evaluation of ensemble-averaged velocity and pressure fields of spray-induced flow.

($\hat{\overline{u}}_1(x_1, x_2, t)$, $\hat{\overline{u}}_2(x_1, x_2, t)$, $\hat{\overline{p}}(x_1, x_2, t)$) under the guidance of measured velocity data, known boundary/initial conditions and modelling equations 10.4 – 10.5. The objective function L is defined by

$$L = \chi_m L_m + \chi_b L_b + \chi_e L_e \tag{10.6}$$

with

$$L_m = \frac{1}{N_m} \sum_{n_m=1}^{N_m} \sum_{i=1}^{2} |\overline{u}_{m_i}^{(n_m)} - \hat{\overline{u}}_i(x_{m_1}^{(n_m)}, x_{m_2}^{(n_m)}, t_m^{(n_m)})|^2,$$

$$L_b = \frac{1}{N_b} \sum_{n_b=1}^{N_b} |\overline{p}_b^{(n_b)} - \hat{\overline{p}}(x_{b_1}^{(n_b)}, x_{b_2}^{(n_b)}, t_b^{(n_b)})|^2,$$

$$L_e = \frac{1}{N_e} \sum_{n_e=1}^{N_e} \left[|e_1(x_{e_1}^{(n_e)}, x_{e_2}^{(n_e)}, t_e^{(n_e)})|^2 + \sum_{i=1}^{2} |e_{2,i}(x_{e_1}^{(n_e)}, x_{e_2}^{(n_e)}, t_e^{(n_e)})|^2 \right],$$

where χ_m, χ_b and χ_e are weighting factors for the respective mean squared errors L_m, L_b and L_e of the measured velocity data, pressure boundary conditions and modelling equations. Note that the model outputs/predictions are denoted by $\hat{(\cdot)}$. The measured velocity data $\overline{u}_{m_i}^{(n_m)}$ with index $i = 1, 2$ and pressure boundary conditions $\overline{p}_b^{(n_b)}$ are trained

at a number of N_m and N_b data points $(x_{m_1}^{(n_m)}, x_{m_2}^{(n_m)}, t_m^{(n_m)})^{\mathrm{T}} \in \Psi_m \subset \Psi$ and $(x_{b_1}^{(n_b)}, x_{b_2}^{(n_b)}, t_b^{(n_b)})^{\mathrm{T}} \in \Psi_b \subset \Psi$, respectively, with $n_m = 1, 2, \cdots, N_m$ and $n_b = 1, 2, \cdots, N_b$. The modelling equations 10.4 – 10.5, on the other hand, are trained over the full range of interest at a finite number of N_e randomly generated and alternating points $(x_{e_1}^{(n_e)}, x_{e_2}^{(n_e)}, t_e^{(n_e)})^{\mathrm{T}} \in \Psi$ with $n_e = 1, 2, \cdots, N_e$

10.2.2 Implementation and training

The PINN architecture was implemented in Python using the open source artificial intelligence library *Tensorflow* (version 2.1.0). The training and calculation was conducted on a *NVIDIA Geforce RTX 2080 Super* graphics processing unit (GPU) and an *AMD Ryzen 9 3950X* processor.
A number of 10 hidden layers with 60 neurons each is used. The weights and biases are initialised according to 'Xavier initialisation' [151]. For training and validation, the velocimetry data is partitioned in training and validation sets with a ratio of 4:1 (training to validation). To minimise the loss/objective function, the Adam algorithm [152] is used as optimiser. In order to improve the convergence [153] of the training, the initial and boundary conditions are are weighted stronger than the regularising equations, i.e. $\chi_m, \chi_b > \chi_e$.

10.3 Experimental configuration and evaluation

The study considers a conventional gasoline direct injection (GDI) multi-hole spray with axisymmetric injector design and centrally oriented spray targeting. The experimental data on spray-induced flow was obtained by means of time-resolved stereoscopic Particle Image Velocimetry (SPIV). The PIV measurement and evaluation was performed according to Chapter 5. To measure the spray-induced flow along the spray-axis, an experimental setup with a top-mounted injector position (see Figure 5.1) was used. Images were recorded at $f_{acq} = 10$ kHz double-frame rate with an interframing time $\mathrm{d}t_{PIV} = 10$ μs. The recorded field of view spans 160×140 mm. To ensure statistical significance, the desired velocity quantities are determined by the ensemble-average of 50 separately performed measurements.

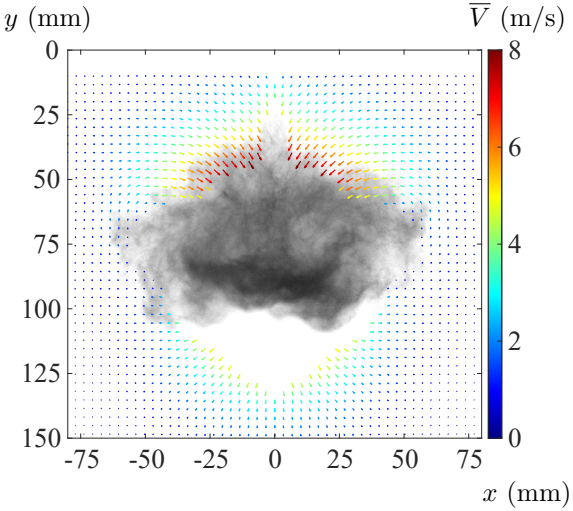

Figure 10.5: Snapshot of the ensemble-averaged velocity data used for the evaluation by means of PINN and conventional pressure from PIV [50] at time $t = 4.2$ ms after SOI. Absolute ensemble-averaged velocity $\overline{V} = \sqrt{\overline{u_1}^2 + \overline{u_2}^2}$.

The measurements were carried out under non-flash-boiling conditions at $p_\infty = 1$ bar, $T_\infty = 25°\text{C}$, $T_{fuel} = 60°\text{C}$ and $p_{inj} = 250$ bar with $Ja = -319$. The flow is modelled with a dynamic viscosity of $\mu = 11.43 \cdot 10^{-6}$ Pa/s, density of $\rho_\infty = 1.25$ kg/m^3 (nitrogen environment) and $\overline{f}_1 = 0$, $\overline{f}_2 = 9.81\ m/s^2$ as body forces.

Figure 10.5 shows a snapshot of the resultant ensemble-averaged velocity field at $t = 4.2$ ms after start of injection (SOI) superimposed on the shadowgram of the underlying spray formation. As illustrated, the velocity data is confined to the spray surrounding and dilute spray regions, while at the area of dense spray there is no data available due to the lack of observable tracer signals. The hidden flow regime accounts for about 25% of the total range of interest. A data resolution of $52 \times 45 \times 60$ ($N_{x_1} \times N_{x_2} \times N_t$) data points was obtained on a regular grid. The measured data was used for the training and validation of the PINN-based pressure evaluation as well as for a comparative state-of-the-art pressure evaluation according to Kling *et al.* [50].

10.4 Results, error discussion and best practices

Figure 10.6 shows the resulting velocity and pressure fields for conventional and PINN-based pressure evaluation. The results are presented on an equivalent grid. Note that PINN provides a continuous description of the latent variables and derivatives. The results show a high level of agreement between both methods. The topology of the pressure distribution is met qualitatively and quantitatively.
Remarkably, the physics-informed neural network is capable of predicting the velocity and pressure field even in the area where no velocimetry data is available by utilizing the conservation of mass and momentum. Furthermore, the PINN-based pressure evaluation confirms the presence of a vortex flow during the event of spray contraction. The data-driven modelling enables the extension of flow evaluation both in space and time. There are no restrictions regarding a fixed grid or range of evaluation. Particularly, the definition of boundary conditions is largely simplified, as e.g. location and temporal incident can be chosen independent from the recorded data.
Sources of potential deviations from the ground truth are incomplete convergence, insufficient (oversimplified) modelling and/or erroneous measurement data. In terms of the present modelling this includes the assumptions of negligible fluctuations, constant gas mixture, material properties, negligible Reynolds stresses. Furthermore, mass, heat and momentum exchange between spray and ambient gas and additional phase-change phenomena have not been considered. The error propagation is largely determined by the definition of the objective function and corresponding weighting factors – λ_m, λ_b, λ_e – , which specify whether the measured data, boundary and initial conditions or the given PDEs are prioritized during optimization.
The experiences made during the course of training is that if the measured velocity data and boundary conditions are prioritized, the mass and momentum conservation are not fully met. As a consequence, both the hidden flow regime and the latent variables of velocity and pressure deviate accordingly. Vice versa, in case of prominent model equations the obtained velocity field overrules the originally measured velocity data to some degree. This can either be advantageous in case of accurate modelling, so that the laws of physics regularize erroneous experimental data, or hindering if the

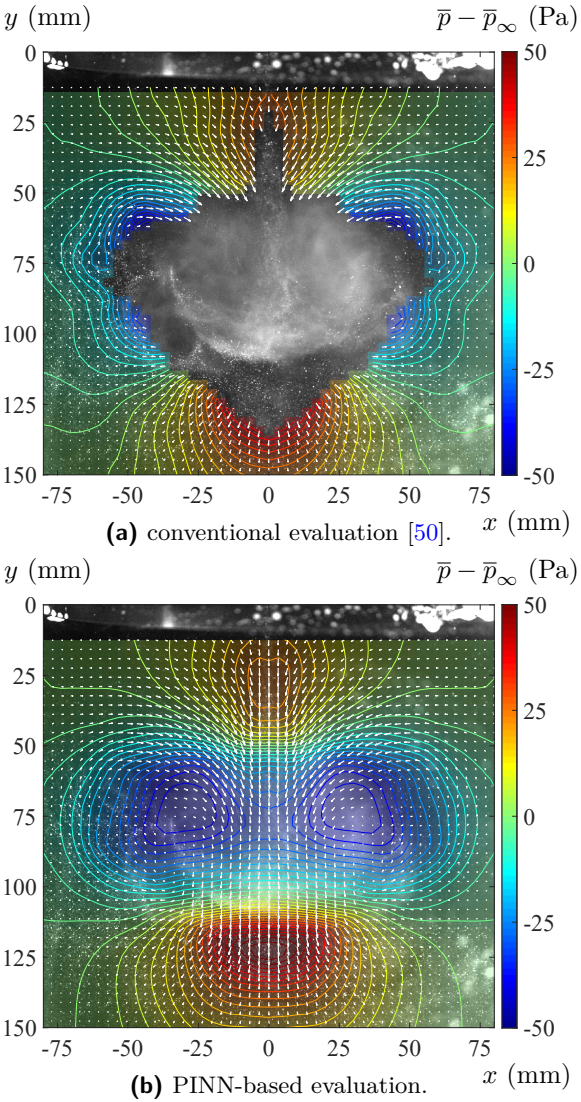

(a) conventional evaluation [50].

(b) PINN-based evaluation.

Figure 10.6: Ensemble-averaged pressure and velocity fields of the spray-induced flow of a GDI 6-hole nozzle at $t = 4.2$ ms after SOI for conventional and PINN-based evaluation.

modelling is inadequate, so that the velocity field is unfavorable modified. The present study confirms the observation of an increased convergence [153] in case of predominant weighting of the measured data and boundary/initial conditions compared to the weighting of the model equations. As best practice, the present study recommends a strong weighting of the measured velocity data and boundary/initial conditions at the early stage of the training until a reasonable state of learning has been achieved, such that the neural networks predicts reasonable velocities, pressures and derivatives, which justify an increasing adjustment in favor of the model equations in order to regularize the intrinsically flawed measurement data. This recommendation mainly applies for sufficiently valid modelling.
In contrast to conventional pressure evaluation, PINN-based pressure evaluation (training) is rather computationally expensive and time consuming. In addition, the configuration of the hyperparameters including the structure, number/type of layers/neurons, activation functions, complementary regularization strategies (weighting, dropout layers), data preconditioning and/or partitioning, training scheme, learning rate, weighting factors etc. is crucial [154] and particularly experience-driven. However, the opportunities of the PINN-based pressure evaluation advances beyond the limitation of conventional algorithms as demonstrated in the presented proof-of-concept study.

10.5 Discussion

With the transfer of physics-informed neural networks to velocimetry-based pressure evaluation, the scope of spray-induced flow analysis and flow evaluation in general changes markedly. The fusion of neural networks and a priori information of laws of physics, models and empirical correlations is able to overcome existing limitations. The data-driven modelling allows for the evaluation of yet hidden flow regimes both in space and time, even for sparse data. PINN opens up the possibility to investigate spray-induced flows and corresponding phenomena beyond conventional analysis approaches, where the vortex flow of a contracting, dense multi-hole spray becomes accessible by means of PINN, as highlighted by the present investigation.

With the ability of neural networks to approximate highly non-linear functions, the technique overcomes the inherent shortcomings of numerical approximation by providing more accurate information on highly desirable derivatives at the level of machine precision through the concept of automatic differentiation. The current restrictive need for high-resolution measurement data is thus significantly reduced. As a result, future spray measurements can be performed with a much lower data resolution, allowing for the use of either higher FOVs, higher frame rates or less sophisticated measurement technology.
The utility of automatic differentiation is of great significance, as it allows a much more accurate characterisation of intrinsically noise-susceptible quantities/terms such as vorticity or viscosity. Due to the very precise function approximation and derivative computation, it is conceivable to use additional laws of physics and modelling equations, such as mass and energy conservation, which are usually not applicable for standard flow evaluation with discrete numerical approximation. The inclusion of mass and energy conservation would, however, extend the scope of current modelling, for instance compressible flows with heat transfer. Such a modelling is considered particularly attractive for the investigation of spray gas interaction at high fuel and/or gas temperatures, respectively flash-boiling conditions, which is foreseen for future investigations.
Finally, some general remarks are placed on the capabilities of PINN. Since the methodology allows the implementation of sophisticated models, it is conceivable to address more complex flows and physics such as flows with chemical reactions or multiphase flows. Moreover, PINN is well suited to exploit the data of different measurement techniques (e.g. velocimetry, temperature/concentration measurement) or any other sources of information. Apart from that, the automatic differentiation and continuous description of variables is very attractive for post-processing and derivative-based tasks such as the computation of Lagrangian particle tracks or finite-time Lyapunov exponents (FTLE) [155–157], for instance. Due to its ability to generalise and cope with sparse data, PINNs have a great potential to be well suited for the prediction of particle tracks. A combination of 4D-PTV algorithms and PINN-based prediction may pose an attractive instrument to increase the accuracy and resolution of current velocimetry techniques.
Accordingly, the author considers the concept of physics-informed neural networks (data-driven modelling) to be a cutting-edge technique with the potential for a fundamental paradigm shift in experimental fluid mechanics.

11 Conclusions and Outlook

In the present work, velocimetry-based pressure evaluation was successfully applied to spray-induced flow of complex gasoline direct injection (GDI) sprays. For the first time, highly-desired pressure field information were experimentally obtained, revealing novel and formerly hidden insights into the nature of sprays. The ability to evaluate pressure fields of spray-induced flow closes an important and much desired gap in research and development, as the cause-effect relationship between induced pressure forces, momentum exchange and material acceleration is now accessible, enabling the study of yet undisclosed mechanisms such as the interplay between spray and ambient gas flow, jet-to-jet interaction and spray contraction.

In order to qualify pressure evaluation of spray-induced flow, a statistical approach based on the Unsteady Reynolds-Averaged Navier-Stokes (URANS) equations and ensemble averaging was introduced in the present work, which enables the pressure evaluation of transient, statistically stationary flows by means of conventional planar PIV. A major advantage of the statistical approach is an advanced accuracy and robustness that can be achieved through the use of multiple measurement samples for the characterisation of the velocity field. It was shown that for a rather moderate number of measurement samples, the contribution of random errors can be reduced significantly. The statistical approach was validated by a comparative pressure sensor measurement, which showed remarkably good agreement both qualitatively and quantitatively. It was further verified in the work of Kaiser *et al.* [158], where a net transient force acting on an impulsively accelerated body in a water flow was quantified based on derived pressure fields. Importantly, the statistical approach offers large degrees of freedom, which allows to overcome some of the current limitations. Thus, the velocity data used for evaluation can be expanded and refined as desired, both spatially and temporally. The data of multiple separate measurements can be merged freely. The statistical

approach proved to be indispensable for the study of sprays, especially spray contraction, due to its advanced robustness and versatility. It is particularly suitable for experiments that suffer from low signal-to-noise ratio, limited optical access and limited measurement technology, such as the PIV of spray-induced flow. Accordingly, the statistical approach enables previously infeasible investigations and spray analysis to be carried out.

As such, the developed methodology of velocimetry-based pressure evaluation was used to investigate the spray transport of multiple GDI sprays for varying operating conditions and spray layouts, and to gain fundamental insights into the interrelation between spray formation, momentum exchange and macroscopic spray properties such as the penetration of spray, as well as into the mechanisms of spray contraction and jet-to-jet interaction. From the study of single jets and multi-hole sprays, it was found that the momentum exchange between spray and ambient gas flow increases with higher injection pressure, gas density, fuel temperature, greater relative velocity, larger spray-gas interface and spray expansion. Furthermore, it was revealed that the salient effect of flash-boiling initiates a particularly high momentum exchange resulting from the strong and immediate disintegration into small droplets and marked expansion of the spray. This result is an important finding, as it quantitatively demonstrates the relevance of small droplets for momentum exchange. Following these insights, it can be concluded that an intensive momentum exchange between spray and ambient gas flow can also be initiated by means of mechanically induced atomisation. This conclusion highlights the great potential that is available in influencing and controlling spray transport by designing sprays with improved mechanical spray disintegration.

Based on the statistical approach and specially designed experiments, so far limited and highly desired experimental data on the velocity and pressure field of a complex GDI multi-hole spray in a cross-sectional plane close to the injector nozzle were obtained for the first time, revealing formerly hidden insights into the mechanisms of jet-to-jet interaction and spray contraction. It was found that the deflection of spray is traced back to a net momentum exerted by the surrounding gas flow on individual spray plumes as a result of pressure forces that are induced by the interplay and momentum exchange between spray and ambient gas flow. As a major finding, the investigation confirms the hypothesised [39–42] presence of lower pressures in the centre area of spray and spray plume interspaces of

multi-hole sprays. This finding supports the theory that spray contraction is caused by spray-induced pressure forces that are reinforced by certain spray designs and operating conditions. It was shown that the effect of jet-to-jet interaction and spray contraction is facilitated by a narrow spray layout and targeting (high spray hole numbers, close mutual jet orientations), strong atomisation (e.g. through flash-boiling) and enhanced droplet tracking behaviour (small droplet sizes, high ambient gas density). From the above findings, it is concluded that in addition to the injection system and engine design, there are viable options in GDI to actively influence and control spray transport during engine operation, e.g. through the SOI, injection timing, multiple injection strategies, exhaust gas recirculation, valve lift/control and tumble/swirl flaps.

While most technical tasks in GDI can be tackled by the use of the statistical approach, there are certain issues that are related to singular injection events/phenomena or shot-to-shot variations which require the evaluation of instantaneous pressure fields and, moreover, the use of sophisticated, usually cost-intensive measurement technology. To enable the evaluation of instantaneous pressure fields by means of an experimental setup with a reduced number of measurement equipment, consisting of two cameras and a single, ordinary light source, a novel quasi-volumetric velocimetry technique (2.5D3C), referred to as Dual-Plane Stereo Astigmatism (DPSA) [51], was developed and successfully demonstrated in the framework of the present thesis. In contrast to existing dual-plane techniques [90], the DPSA approach utilises astigmatism-based depth codification and a discrete planar illumination to enable a simultaneous measurement in two planar measurement domains through the use of particle image identification algorithms. As part of the development of DPSA, new processing and evaluation techniques were introduced, which includes two different strategies for particle identification – a correlation-based method (CPI) and an adapted version of the iterative particle identification (IPR) approach [139] – and a new approach for PIV evaluation. The performance of DPSA was evaluated using synthetic images generated from DNS data of a turbulent boundary layer flow, showing good results for both the in-plane and out-of-plane velocities and velocity gradients. Furthermore, first experimental applications to spray-induced flow yielded feasible and promising data suggesting the use of DPSA for spray analysis and velocimetry-based pressure evaluation. For a comparatively low budget, the DPSA approach allows for the full characterisation of the velocity gradient tensor and thus

the evaluation of instantaneous pressure fields. The DPSA approach is particularly attractive for applications with limited optical accessibility (no use of multiple cameras feasible) and low signal-to-noise ratios.
As a further step to overcome current limitations of data evaluation, the recently introduced deep learning technique of physics-informed neural networks (PINN) was successfully transferred to velocimetry-based pressure evaluation. The capabilities of neural networks as freely trainable, powerful approximators of highly non-linear functions allow for a more advanced evaluation of flows by combining both measurement data and a priori information such as laws of physics and empirical correlations. As was demonstrated by the evaluation of a contracting GDI multi-hole spray, PINN is able to evaluate the pressure field in the much desired area of dense, liquid spray, where velocimetry data of spray-induced flow have not been accessible so far. The data-driven modelling enables the evaluation of formerly hidden flow regimes, both in space and time, and reduces the amount of required data resolution, thus extending the limits of applicable flows, measurement techniques and setup configurations significantly. Due to its ability to provide particularly accurate function approximation, especially the description of derivatives, PINN is hypothesised to justify the use of additional equations for flow modelling, which may allow the treatment of further physics such as compressibility, heat transfer, mixing, turbulence or chemical reactions. In conjunction with its great freedom in data processing, PINN is believed to be well-suited to combine different data sources and measurement methods, e.g. velocity data from PIV [10], LDV, PDV, or hot-wire anemometry [159], pressure data from pressure sensors [159] or pressure sensitive paint [160], species concentrations from Ramann imaging [161, 162] or temperature data from LIF [159], particle image thermography [163–165], temperature sensitive paint [160, 166] or coherent anti-Stokes Raman scattering [159, 167], to fully exploit the available data and knowledge. From the author's point of view, PINN is considered a highly disruptive technique capable of significantly extending the current limits of velocimetry-based pressure evaluation and, moreover, of data evaluation in experimental fluid mechanics.
The present work has led to a number of important findings in the field of spray transport of GDI sprays and, moreover, to the introduction and development of new, powerful approaches and methods that are able to provide even deeper insights into sprays. As such, the present work forms the basis for further research and development, e.g. the investigation of

further sprays, design parameters, multiple injection strategies or, very interestingly, the influence of superimposed ambient gas flows to study spray transport for engine-type flow conditions. As an outlook, attention should be drawn to possible megatrends within the automotive industry. Due to the increasingly strict legislation on CO_2 fleet emissions and possible legislative changes, alternative/synthetic fuels as well as hydrogen combustion engines [168, 169] may represent future options for reducing CO_2 emissions. The procedures and methods developed in the present work are powerful tools for gaining valuable insights and knowledge for the design and development of such systems.

Bibliography

[1] John B Heywood. *Internal Combustion Engine Fundamentals*. McGraw Hill, New York, 1988. ISBN 978-0071004992.

[2] Andreas Kufferath, Wolfram Wiese, Wolfgang Samenfink, Helge Dageförde, Tobias Knorsch, and Paul Jochman. Assessment of feasible system solutions for future particle emission requirements. *In: IMechE Combustion Engines & Fuels Group Conference, London, UK*, 2015.

[3] Xu He, Yankai Li, Cong Liu, Magnus Sjöberg, David Vuilleumier, Fushui Liu, and Qing Yang. Characteristics of spray and wall wetting under flash-boiling and non-flashing conditions at varying ambient pressures. *Fuel*, 264:116683, 2020. doi:10.1016/j.fuel.2019.116683.

[4] Helmut Eichlseder, Manfred Klüting, and Walter Piock. *Grundlagen und Technologien des Ottomotors*. Springer, Vienna, 2008. ISBN 978-3-211-47104-3. doi:10.1007/978-3-211-47104-3.

[5] Philip Price. Direct injection gasoline engine particulate emissions. PhD thesis, University of Oxford, Oxford 2009. URL https://ora.ox.ac.uk/objects/uuid:35c0d6bf-bde3-4ef0-a87e-4af89a94b16f.

[6] Xin He, Matthew A Ratcliff, and Bradley T Zigler. Effects of Gasoline Direct Injection Engine Operating Parameters on Particle Number Emissions. *Energy Fuels*, 26(4):2014–2027, 2012. doi:10.1021/ef201917p.

[7] Mohsin Raza, Longfei Chen, Felix Leach, and Shiting Ding. A Review of Particulate Number (PN) Emissions from Gasoline Direct Injection (GDI) Engines and Their Control Techniques. *Energies*, 11 (6), 2018. doi:10.3390/en11061417.

[8] Commission Regulation (EU). 2016/646 of 20 April 2016 amending Regulation (EC) No 692/2008 as regards emissions from light passenger and commercial vehicles (Euro 6) (Text with EEA relevance). Available at: http://data.europa.eu/eli/reg/2016/646/oj (Accessed: 6. September 2021), 2016.

[9] Todd D Fansler and Scott E Parrish. Spray measurement technology: a review. *Meas. Sci. Technol.*, 26(1):012002, 2014. doi:10.1088/0957-0233/26/1/012002.

[10] Markus Raffel, Christian E Willert, Fulvio Scarano, Christian J Kähler, Steven Wereley, and Jürgen Kompenhans. *Particle Image Velocimetry*. Springer, Cham, 2018. ISBN 978-3-319-68851-0. doi:10.1007/978-3-319-68852-7.

[11] Cameron Tropea. Optical Particle Characterization in Flows. *Annu. Rev. Fluid Mech.*, 43(1):399–426, 2011. doi:10.1146/annurev-fluid-122109-160721.

[12] Lyle M Pickett, Caroline L Genzale, Julien Manin, Loius-Marie Malbec, and Laurent Hermant. Measurement Uncertainty of Liquid Penetration in Evaporating Diesel Sprays. *In: ILASS Americas, 23rd Annual Conf. on Liquid Atomization and Spray Systems, Ventura, USA*, 2011.

[13] Alessandro Montanaro and Luigi Alloca. Flash Boiling Evidences of a Multi-Hole GDI Spray under Engine Conditions by Mie-Scattering Measurements. *SAE Tech. Pap.*, 2015-01-1945, 2015. doi:10.4271/2015-01-1945.

[14] Nicholas Mitroglou, Jamshid M Nouri, Youyou Yan, Manolis Gavaises, and Constantine Arcoumanis. Spray Structure Generated by Multi-Hole Injectors for Gasoline Direct-Injection Engines. *SAE Tech. Pap.*, 2007-01-1417, 2007. doi:10.4271/2007-01-1417.

[15] Jeekuen Lee, Masahisa Yamakawa, Seiji Isshiki, and Keiya Nishida. An Analysis of Droplets and Ambient Air Interaction in a D.I. Gasoline Spray Using LIF-PIV Technique. *SAE Tech. Pap.*, 2002-01-0743, 2002. doi:10.4271/2002-01-0743.

[16] Jeekuen Lee, Keiya Nishida, and Masahisa Yamakawa. An Analysis of Ambient Air Entrainment into Split Injection D.I. Gasoline Spray by LIF-PIV Technique. *SAE Tech. Pap.*, 2002-01-2662, 2002. doi:10.4271/2002-01-2662.

[17] Thomas Boëdec and Serge Simoëns. Instantaneous and simultaneous planar velocity field measurements of two phases for turbulent mixing of high pressure sprays. *Exp. Fluids*, 31(7):506–518, 2001. doi:10.1007/s003480100311.

[18] Virginia R Palero and Ikeda Yuji. Droplet-size-classified stereoscopic PIV for spray characterization. *Meas. Sci. Technol.*, 13(7), 2002. doi:10.1088/0957-0233/13/7/312.

[19] Gregor Rottenkolber, Jörg Gindele, Jorge Raposo, Klaus Dullenkopf, Wolfgang Hentschel, Sigmar Wittig, Ulrich Spicher, and Wolfgang Merzkirch. Spray analysis of a gasoline direct injector by means of two-phase PIV. *Exp. Fluids*, 32:710–721, 2002. doi:10.1007/s00348-002-0441-8.

[20] Kristina D Driscoll, Volker Sick, and C Gray. Simultaneous air/fuel-phase PIV measurements in a dense fuel spray. *Exp. Fluids*, 35: 112–115, 2003. doi:10.1007/s00348-003-0647-4.

[21] Luis Le Moyne, Pierre Guibert, Raghunath Roy, and Benoit Jeanne. Fluorescent-PIV Spray/Air interaction analysis of high-pressure gasoline injector. *SAE Tech. Pap.*, 2007-01-1825, 2007. doi:10.4271/2007-01-1825.

[22] Brice Prosperi, Guillaume Delay, Rudi Bazile, Jerome Helie, and Hans J Nuglish. FPIV study of gas entrainment by a hollow cone spray submitted to variable density. *Exp. Fluids*, 43:315–327, 2007. doi:10.1007/s00348-007-0304-4.

[23] Virginie Sepret, Rudi Bazile, Moise Marchal, and Gerard Couteau. Effect of ambient density and orifice diameter on gas entrainment by a single-hole diesel spray. *Exp. Fluids*, 49:1293–1305, 2010. doi:10.1007/s00348-010-0869-1.

[24] Seoksu Moon, Yuhei Matsumoto, Keiya Nishida, and Jian Gao. Gas entrainment characteristics of diesel spray injected by a group-hole nozzle. *Fuel*, 89:3287–3299, 2010. doi:10.1016/j.fuel.2010.05.011.

[25] Diego Angarita-Jaimes, Catherine E Towers, and David P Towers. Three-component multi-phase velocimetry measurements on a GDI spray using optically efficient fluorescent tracers. *Exp. Fluids*, 52: 949–962, 2012. doi:10.1007/s00348-011-1174-3.

[26] Jingyu Zhu, Olawole A Kuti, and Keiya Nishida. An investigation of the effects of fuel injection pressure, ambient gas density and nozzle hole diameter on surrounding gas flow of a single diesel spray by the laser-induced fluorescence–particle image velocimetry technique. *Int. J. Engine Res.*, 14(6), 2013. doi:10.1177/1468087412458778.

[27] Ming Zhang, Min Xu, and David L S Hung. Simultaneous two-phase flow measurement of spray mixing process by means of high-speed two-color PIV. *Meas. Sci. Technol.*, 25(9), 2014. doi:10.1088/0957-0233/25/9/095204.

[28] Mehdi Mojtabi, Graham Wigley, and Jerome Helie. The Effect of Flash Boiling on the Atomization Performance of GDI Multi-Stream Injectors. *At. Sprays*, 24(6):467–493, 2014. doi:10.1615/AtomizSpr.2014008296.

[29] Brad A VanDerWege and Simone Hochgreb. Effects of fuel volatility and operating conditions on fuel sprays in disi engines: (1) imaging investigation. *SAE Tech. Pap.*, 2000-01-0535, 2000. doi:10.4271/2000-01-0535.

[30] Ming Zhang, Min Xu, Yuyin Zhang, and Wei Zeng. Flow-field Evaluation of Superheated Fuel Sprays using High-Speed PIV. *SAE Tech. Pap.*, 2011-01-1880, 2011. doi:10.4271/2011-01-1880.

[31] Wei Zeng, Min Xu, Ming Zhang, Yuyin Zhang, and David J Cleary. Macroscopic characteristics for direct-injection multi-hole sprays using dimensionless analysis. *Exp. Fluids*, 40(81-92), 2012. doi:10.1016/j.expthermflusci.2012.02.003.

[32] Martin Krämer, Eberhard Kull, and Michael Wensing. Flashboiling-induced targeting changes in gasoline direct injection sprays. *Int. J. Engine Res.*, 17(1):97–107, 2015. doi:10.1177/1468087415604763.

[33] Florian Schulz and Frank Beyrau. The influence of flash-boiling on spray-targeting and fuel film formation. *Fuel*, 208:587–594, 2017. doi:10.1016/j.fuel.2017.07.047.

[34] Hengjie Guo, Xiao Ma, Yanfei Li, Shuai Liang, Zhi Wang, Hongming Xu, and Jianxin Wang. Effect of flash boiling on microscopic and macroscopic spray characteristics in optical GDI engine . *Exp. Fluids*, 190:79–89, 2017. doi:10.1016/j.fuel.2016.11.043.

[35] Xuesong Li, Tianyun Li, and Min Xu. Effect of ambient temperature on flash-boiling spray characteristics for a multi-hole gasoline injector. *Exp. Fluids*, 60(109), 2019. doi:10.1007/s00348-019-2754-x.

[36] Shengqi Wu, Shangze Yang, and Margaret Wooldridge. Experimental study of the spray collapse process of multi-hole gasoline fuel injection at flash boiling conditions. *Fuel*, 242:109–123, 2019. doi:10.1016/j.fuel.2019.01.027.

[37] Philippe Leick. Quantitative Untersuchungen zum Einfluss von Düsengeometrie und Gasdichte auf den Primärzerfallsbereich von Dieselsprays (in German). Dissertation, Technische Universität Darmstadt, Darmstadt, September 2008. URL http://tuprints.ulb.tu-darmstadt.de/1159/.

[38] Raul Payri, Francisco J Salvador, Pedro Martí-Aldaraví, and Daniel Vaquerizo. ECN Spray G external spray visualization and spray collapse description through penetration and morphology analysis. *Appl. Therm. Eng.*, 112:304–316, 2017. ISSN 1359-4311. doi:10.1016/j.applthermaleng.2016.10.023.

[39] Daniel Weber. Flash Boiling bei Ottomotoren mit Benzindirekteinspritzung: Experimentelle Untersuchungen, Modellierung und numerische Simulation (in German). Dissertation, Technische Universität Darmstadt, Darmstadt, June 2016. URL https://tuprints.ulb.tu-darmstadt.de/id/eprint/57430.

[40] Hengjie Guo, Yanfei Li, Hongming Xu, Shijin Shuai, and Huiqiang Zhang. Interaction between under-expanded flashing jets: A numerical study. *Int. J. Heat Mass Transf.*, 137:990–1000, 2019. ISSN 0017-9310. doi:10.1016/j.ijheatmasstransfer.2019.04.010.

[41] Sampath K Rachakonda, Arman Paydarfar, and David P Schmidt. Prediction of spray collapse in multi-hole gasoline direct-injection fuel injectors. *Int. J. Engine Res.*, 20(1):18–33, 2019. doi:10.1177/1468087418819527.

[42] Jan Wilhelm Gärtner, Ye Feng, Andreas Kronenburg, and Oliver T Stein. Numerical Investigation of Spray Collapse in GDI with OpenFOAM. *Fluids*, 6(3), 2021. ISSN 2311-5521. doi:10.3390/fluids6030104.

[43] Roi Gurka, Alex Liberzon, D Hefetz, Dror Rubinstein, and Uri Shavit. Computation of Pressure Distribution Using PIV Velocity Data. *In: 3rd International workshop on PIV, Santa Barbara, USA*, 1999.

[44] Bas W van Oudheusden. Principles and application of velocimetry-based planar pressure imaging in compressible flows with shocks. *Exp. Fluids*, 45:657–674, 2008. doi:10.1007/s00348-008-0546-9.

[45] Daniele Ragni, Anand Ashok, Bas V van Oudheusden, and Fulvio Scarano. Surface pressure and aerodynamic loads determination of a transonic airfoil based on particle image velocimetry. *Meas. Sci. Technol.*, 20(7):074005, 2009. doi:10.1088/0957-0233/20/7/074005.

[46] Xiaofeng Liu and Joseph Katz. Vortex-corner interactions in a cavity shear layer elucidated by time-resolved measurements of the pressure field. *J. Fluid Mech.*, 728:417–457, 2013. doi:10.1017/jfm.2013.275.

[47] Wouter Terra, Andrea Sciacchitano, and Fulvio Scarano. Aerodynamic drag of a transiting sphere by large-scale tomographic-PIV. *Exp. Fluids*, 58(83), 2017. doi:10.1017/jfm.2013.275.

[48] Bas W van Oudheusden. PIV-based pressure measurement. *Meas. Sci. Technol.*, 24(3), 2013. doi:10.1088/0957-0233/24/3/032001.

[49] Gerrit E Elsinga, Fulvio Scarano, Bernhard Wieneke, and Bas W van Oudheusden. Tomographic particle image velocimetry. *Exp. Fluids*, 41:933–947, 2006. doi:10.1007/s00348-006-0212-z.

[50] Nils H Kling, Jochen Kriegseis, Lars Opfer, and Philipp Rogler. Pressure evaluation of spray-induced flow in the framework of a statistical approach based on URANS and ensemble averaging. *Meas. Sci. Technol.*, 30(8), 2019. doi:10.1088/1361-6501/ab12b7.

[51] Nils H Kling, Jochen Kriegseis, Lars Opfer, and Philipp Rogler. Dual-plane stereo-astigmatism – a novel method to determine the

full velocity gradient tensor in planar domain. *Meas. Sci. Technol.*, 31(8), 2020. doi:10.1088/1361-6501/ab7283.

[52] Maziar Raissi, Paris Perdikaris, and George Em Karniadakis. Physics Informed Deep Learning (Part I): Data-driven Solutions of Nonlinear Partial Differential Equations, 2017. URL https://arxiv.org/abs/1711.10561.

[53] Maziar Raissi, Paris Perdikaris, and George Em Karniadakis. Physics Informed Deep Learning (Part II): Data-driven Discovery of Nonlinear Partial Differential Equations, 2017. URL https://arxiv.org/abs/1711.10566.

[54] Arthur H Lefebvre and Vincent G McDonell. *Atomization and Sprays*. CRC Press, Boca Raton, 2017. ISBN 9781315120911. doi:10.1201/9781315120911.

[55] Wolfgang von Ohnesorge. Die Bildung von Tropfen an Düsen und die Auflösung flüssiger Strahlen. *Zeitschrift für Angewandte Mathematik und Mechanik*, 16(6):355–358, 1936. doi:10.1002/zamm.19360160611.

[56] Rolf D Reitz and Frediano V Bracco. Mechanisms of breakup of round liquid jets. *Encyclopedia of fluid mechanics*, 3:233–249, 1986.

[57] Francisco Payri, Vicente Bermúdez, Raul Payri, and Javier F Salvador. The influence of cavitation on the internal flow and the spray characteristics in diesel injection nozzles. *Fuel*, 83(4-5):419–431, 2004. doi:10.1016/j.fuel.2003.09.010.

[58] Raul Payri, Jose M Garcia, Javier F Salvador, and Jaime Gimeno. Using spray momentum flux measurements to understand the influence of diesel nozzle geometry on spray characteristics. *Fuel*, 84(5): 551–561, 2005. doi:10.1016/j.fuel.2004.10.009.

[59] Jochen Walther. Quantitative Untersuchung der Innenströmung in kavitierenden Dieseleinspritzdüsen (in German). Dissertation, Technische Universität Darmstadt, Darmstadt, April 2002. URL https://tuprints.ulb.tu-darmstadt.de/id/eprint/241.

[60] Lars Zigan, Jun-Mei Shi, Ivan Krotow, Ingo Schmitz, Michael Wensing, and Alfred Leipertz. Fuel property and fuel temperature effects on internal nozzle flow, atomization and cyclic spray fluctuations of

a direct injection spark ignition–injector. *Int. J. Engine Res.*, 14(6): 543–556, 2013. doi:10.1177/1468087413482320.

[61] Nils H Kling, Lars Opfer, Bettina Frohnapfel, Philipp Rogler, and Jochen Kriegseis. Analysis of the spray-gas interaction of a single GDI jet by means of velocimetry-based pressure evaluation. *At. Sprays*, 32(7):23–33, 2022. doi:10.1615/AtomizSpr.2022042103.

[62] Nasser Ashgriz. *Handbook of Atomization and Sprays: Theory and Applications*. Springer New York, NY, 2011. ISBN 978-1-4419-7263-7. doi:10.1007/978-1-4419-7264-4.

[63] Christopher E Brennen. *Cavitation and Bubble Dynamics*. Cambridge University Press, Cambridge, 1995. ISBN 9781107338760. doi:10.1017/CBO9781107338760.

[64] David P Schmidt and Michael L Corradini. The internal flow of diesel fuel injector nozzles: A review. *Int. J. Engine Res.*, 2(1):1–22, 2001. doi:10.1243/1468087011545316.

[65] Hiroyuki Hiroyasu. Spray breakup mechanism from the hole-type nozzle and its applications. *At. Sprays*, 10(3):511–527, 2000. doi:10.1615/AtomizSpr.v10.i3-5.130.

[66] Lionel C Ganippa, Göran Bark, Sven Andersson, and Jerzy Chomiak. The Structure of Cavitation and Its Effect on the Spray Pattern in a Single-Hole Diesel Nozzle. *SAE Tech. Pap.*, 2001-01-2008, 2001. doi:10.4271/2001-01-2008.

[67] Ricard Miranda, Humberto Chaves, Uwe Martin, and Frank Obermeier. Cavitation in a transparent real size VCO injecction nozzle. *In: ICLASS 2003 9th Int. Conf. on Liquid Atomization & Spray Systems, Sorrento, Italy*, 2003.

[68] Franc Jean-Pierre and Michel Jean-Marie. *Fundamentals of cavitation*. Springer, Dordrecht, 2005. ISBN 978-1-4020-2232-6. doi:10.1007/1-4020-2233-6.

[69] Miltion Blander and Joseph L Katz. Bubble nucleation in liquids. *Am. Inst. Chem. Eng. J.*, 21:833–848, 1975. doi:10.1002/aic.690210502.

[70] Joseph Spurk and Nuri Aksel. *Fluid Mechanics*. Springer Berlin, Heidelberg, 2008. ISBN 978-3-540-73537-3. doi:10.1007/978-3-540-73537-3.

[71] Adamantios Andriotis, Manolis Gavaises, and Constantine Arcoumanis. Vortex flow and cavitation in diesel injector nozzles. *J. Fluid Mech.*, 610:195–215, 2008. doi:10.1017/S0022112008002668.

[72] Manolis Gavaises, Antonis N Andriotis, Dimitrios Papoulias, Nicholas Mitroglou, and Andreas Theodorakakos. Characterization of string cavitation in large-scale diesel nozzles with tapered holes. *Phys. Fluids*, 21:052107:195–215, 2009. doi:10.1063/1.3140940.

[73] Manolis Gavaises, Benjamin A Reid, Nicholas Mitroglou, Graham Hargrave, Colin P Garner, Edward J Long, and Robert M McDavid. On the formation of string cavitation inside fuel injectors. *Exp. Fluids*, 55(1662), 2014. doi:10.1007/s00348-013-1662-8.

[74] Eran Sher, Tali Bar-Kohany, and Alexander Rashkovan. Flash-boiling atomization. *Progress in Energy and Combustion Science*, 34(4):417–439, 2008. doi:10.1016/j.pecs.2007.05.001.

[75] Manolis Gavaises and Adamantios Andriotis. Cavitation Inside Multi-hole Injectors for Large Diesel Engines and Its Effect on the Near-nozzle Spray Structure. *SAE Tech. Pap.*, 2006-01-1114, 2006. doi:10.4271/2006-01-1114.

[76] Dmitrii Mamaikin. Experimental Investigation of Internal Flow and Jet Breakup for Gasoline Direct Injection Systems. Dissertation, Friedrich-Alexander Universität Erlangen-Nürnberg, Erlangen-Nürnberg, June 2021. URL `http://www.shaker.de/shop/978-3-8440-8037-7`.

[77] Jose Serras-Pereira, Zane van Romunde, Pavlos G Aleiferis, David Richardson, Stan Wallace, and Roger F Cracknell. Cavitation, primary break-up and flash boiling of gasoline, iso-octane and n-pentane with a real-size optical direct-injection nozzle. *Fuel*, 89(9): 2592–2607, 2010. doi:10.1016/j.fuel.2010.03.030.

[78] Tali Bar-Kohany and Moti Levy. State of the art review of flash-boiling atomization. *At. Sprays*, 26(12):1259–1305, 2016. ISSN 1044-5110. doi:10.1615/AtomizSpr.2016015626.

[79] Shiquan Shen, Ming Jia, Tianyou Wang, Qieni Lü, and Kai Sun. Measurement of the droplets sizes of a flash boiling spray using an improved extended glare point velocimetry and sizing. *Exp. Fluids*, 57(56), 2016. doi:10.1007/s00348-016-2147-3.

[80] Fulvio Scarano, Sina Ghaemi, Guiseppe C A Caridi, Johannes Bosbach, Uwe Dierksheide, and Andrea Sciacchitano. On the use of helium-filled soap bubbles for large-scale tomographic PIV in wind tunnel experiments. *Exp. Fluids*, 56(42), 2015. doi:10.1007/s00348-015-1909-7.

[81] David Engler Faleiros, Marthijn Tuinstra, Andrea Sciacchitano, and Fulvio Scarano. Generation and control of helium-filled soap bubbles for PIV. *Exp. Fluids*, 60(40), 2019. doi:10.1007/s00348-019-2687-4.

[82] Merouane Hamdi, Michel Havet, Olivier Rouaud, and Dominic Tarlet. Comparison of different tracers for PIV measurements in EHD airflow. *Exp. Fluids*, 55(1702), 2014. doi:10.1007/s00348-014-1702-z.

[83] Jiarong Hong, Mostafa Toloui, Leonardo P Chamorro, Michele Guala, Kevin Howard, Sean Riley, James Tucker, and Fotis Sotiropoulos. Natural snowfall reveals large-scale flow structures in the wake of a 2.5-MW wind turbine. *Nat. Commun.*, 5(4216), 2014. doi:10.1038/ncomms5216.

[84] Hugo Wioland, Enkeleida Lushi, and Raymond E Goldstein. Directed collective motion of bacteria under channel confinement. *New J. Phys.*, 18, 2014. doi:10.1088/1367-2630/18/7/075002.

[85] Christian Cierpka and Christian J Kähler. Particle imaging techniques for volumetric three-component (3D3C) velocity measurements in microfluidics. *J. Vis.*, 15:1–31, 2012. doi:10.1007/s12650-011-0107-9.

[86] Elias Baum, Brian Peterson, Caroline Surmann, Dirk Michaelis, Benjamin Böhm, and Andreas Dreizler. Investigation of the 3D flow field in an IC engine using tomographic PIV. *Proc. Combust. Inst.*, 34(2):2903–2910, 2013. doi:10.1016/j.proci.2012.06.123.

[87] Christian Disch, Heiko Kubach, Ulrich Spicher, Jürgen Pfeil, Frank Altenschmidt, and Uwe Schaupp. Investigations of Spray-Induced Vortex Structures during Multiple Injections of a DISI Engine in

Stratified Operation Using High-Speed-PIV. *SAE Tech. Pap.*, 2, 2013. doi:10.4271/2013-01-0563.

[88] Jürgen Kompenhans, Markus Raffel, Lutz Dieterle, Tim Dewhirst, Heinrich Vollmers, Klaus Ehrenfried, Olaf Ronneberger, Christian Willert, Kurt Pengel, Christian J Kähler, Andreas Schröder, and Olaf Ronneberger. Particle image velocimetry in aerodynamics: Technology and applications in wind tunnels. *J. Vis.*, 2:229–244, 2000. doi:10.1007/BF03181440.

[89] Maria del Pilar Arroyo and Clive Greated. Stereoscopic particle image velocimetry. *Meas. Sci. Technol.*, 2(12):1181–1186, 1991. doi:10.1088/0957-0233/2/12/012.

[90] Christian J Kähler and Jürgen Kompenhans. Fundamentals of multiple plane stereo particle image velocimetry. *Exp. Fluids*, 29: 70–77, 2000. doi:10.1007/s003480070009.

[91] Alex Liberzon, Roi Gurka, and Gad Hetsroni. XPIV–Multi-plane stereoscopic particle image velocimetry. *Exp. Fluids*, 36(2):355–362, 2004. doi:10.1007/s00348-003-0731-9.

[92] Hans-Gerd Maas, Armin Gruen, and Dimitrios Papantoniou. Particle tracking velocimetry in three-dimensional flows. *Exp. Fluids*, 15: 133–146, 1993. doi:10.1007/BF00190953.

[93] Rainer Hain and Christian J Kähler. Single camera volumetric velocity measurements using optical aberrations. *In: 12th Int. Symp. Flow Visualization, Göttingen, Germany*, 2006.

[94] Christian Cierpka, Rodrigo Segura, Rainer Hain, and Christian J Kähler. A simple single camera 3C3D velocity measurement technique without errors due to depth of correlation and spatial averaging for microfluidics. *Meas. Sci. Technol.*, 21(4), 2010. doi:10.1088/0957-0233/21/4/045401.

[95] Christian E Willert and Morteza Gharib. Three-dimensional particle imaging with a single camera. *Exp. Fluids*, 12:353–358, 1992. doi:10.1007/BF00193880.

[96] Klaus D Hinsch. Holographic particle image velocimetry. *Meas. Sci. Technol.*, 13(7):61–72, 2002. doi:10.1088/0957-0233/13/7/201.

[97] Daniel Schanz, Sebastian Gesemann, and Schröder A. Shake-the-box: lagrangian particle tracking at high particle image densities. *Exp. Fluids*, 57(70), 2016. doi:10.1007/s00348-016-2157-1.

[98] Stefano Discetti and Filippo Coletti. Volumetric velocimetry for fluid flows. *Meas. Sci. Technol.*, 29(4), 2018. doi:10.1088/1361-6501/aaa571.

[99] Theodor Scheimpflug. Improved Method and Apparatus for the Systematic Alteration or Distortion of Plane Pictures and Images by Means of Lenses and Mirrors for Photography and for other purposes. *GB Patent No. 1196*, 1904.

[100] Christian E Willert. Stereoscopic digital particle image velocimetry for application in wind tunnel flows. *Meas. Sci. Technol.*, (12), 1997. doi:10.1088/0957-0233/8/12/010.

[101] Bernhard Wieneke. Stereo-PIV using self-calibration on particle images. *Exp. Fluids*, 39:267–280, 2005. doi:10.1007/s00348-005-0962-z.

[102] Joseph V Boussinesq. Sur la résistance qu'oppose un fluide indéfini au repos, sans pesanteur, au mouvement varié d'une sphère solide qu'il mouille sur toute sa surface, quand les vitesses restent bien continues et assez faibles pour que leurs carrés et produits soient négligeables. *Comptes Rendus de l'Académie des Sciences*, 100:935–937, 1885.

[103] Alfred B Basset. On the Motion of a Sphere in a Viscous Liquid. *Phil. Trans. Roy. Soc. A*, 179:43–63, 1888. URL `http://www.jstor.org/stable/90514`.

[104] Adrian Melling. Tracer particles and seeding for particle image velocimetry. *Meas. Sci. Technol.*, 8(12), 1997. doi:10.1088/0957-0233/8/12/005.

[105] Michael G Olsen and Ronald J Adrian. Out-of-focus effects on particle image visibility and correlation in microscopic particle image velocimetry. *J. Fluid Mech.*, 29:166–174, 2000. doi:10.1007/s003480070018.

[106] Richard D Keane and Ronald J Adrian. Optimization of particle image velocimeters. I. Double pulsed systems. *Meas. Sci. Technol.*, 1(11):1–19, 1990. doi:10.1088/0957-0233/1/11/013.

[107] Bernhard Wieneke. PIV Uncertainty Quantification and Beyond. PhD thesis, Delft University of Technology, Delft, December 2017. doi:10.4233/uuid:4ca8c0b8-0835-47c3-8523-12fc356768f3.

[108] Jerry Westerweel and Fulvio Scarano. Universal outlier detection for PIV data. *Exp. Fluids*, 39:1096–1100, 2005. doi:10.1007/s00348-005-0016-6.

[109] Jerry Westerweel, Dana Dabiri, and Morteza Gharib. The effect of a discrete window offset on the accuracy of cross-correlation analysis of PIV recordings. *Exp. Fluids*, 23:20–28, 1997. doi:10.1007/s003480050082.

[110] Steven T Wereley and Carl D Meinhart. Second-order accurate particle image velocimetry. *Exp. Fluids*, 31:258–268, 2001. doi:10.1007/s003480100281.

[111] Fulvio Scarano. Iterative image deformation methods in PIV. *Meas. Sci. Tech.*, 13(1):1–19, 2002. doi:10.1088/0957-0233/13/1/201.

[112] Ferry F J Schrijer and Fulvio Scarano. Effect of predictor-corrector filtering on the stability and spa- tial resolution of iterative PIV interrogation. *Exp. Fluids*, 45(5), 2008. doi:0.1007/s00348-008-0511-7.

[113] Richard D Keane and Ronald J Adrian. Theory of cross-correlation analysis of PIV images. *Appl. Sci. Res.*, 49(3):191–215, 1990. doi:10.1007/BF00384623.

[114] Julio Soria. An investigation of the near wake of a circular cylinder using a video-based digital cross-correlation particle image velocimetry technique. *Exp. Thermal Fluid Sci.*, (2), 1996. doi:10.1016/0894-1777(95)00086-0.

[115] Carl D Meinhart, Steven T Wereley, and Mike H B Gray. Volume illumination for two-dimensional particle image velocimetry. *Meas. Sci. Technol.*, 11(6):809–814, 2000. doi:10.1088/0957-0233/11/6/326.

[116] Paul L van Gent, Bas W van Oudheusden, and Ferry F J Schrijer. Determination of mean pressure from PIV in compressible flows using the Reynolds-averaging approach. *Exp. Fluids*, 59(41), 2018. doi:10.1007/s00348-018-2487-2.

[117] Philipp Rogler, Roman Grzeszik, Stefan Arndt, and Manfred Aigner. 3D analysis of vapor and liquid phase of GDI injectors using laser induced exciplex fluorescence tomography in a high pressure/high temperature spray chamber. *SAE Tech. Pap.*, 2007-01-1827, 2007. doi:10.4271/2007-01-1827.

[118] Tillmann Bauer and Jürgen Könteger. PIV with high temporal resolution for the determination of local pressure reductions from coherent turbulent phenomena. *In: 3rd Int. Workshop on Particle Image Velocimetry, Santa Barbara, USA*, pages 101–106, 1999.

[119] Louis Souverein, Bas W van Oudheusden, and Fulvio Scarano. Particle image velocimetry based loads determination in supersonic flows. *In: 45th AIAA Aerospace Sciences Meeting and Exhibit, Reno, USA*, 2007. doi:10.2514/6.2007-50.

[120] Nils H Kling, Jochen Kriegseis, Lars Opfer, and Philipp Rogler. Analysis of air entrainment of gasoline direct injection (GDI) nozzles by means of time-resolved stereo fluorescence particle image velocimetry. *In: ICLASS 2018 14th Int. Conf. on Liquid Atomization & Spray Systems, Chicago, USA*, 2018.

[121] Nils H Kling, Jochen Kriegseis, Lars Opfer, and Philipp Rogler. Pressure evaluation of spray-induced flow by means of URANS and time-resolved stereo particle image velocimetry. *In: 19th Int. Symp. on Applications of Laser and Imaging Techniques to Fluid Mechanics, Lisbon, Portugal*, 2018.

[122] William Sutherland. LII. The viscosity of gases and molecular force. *Philosophical Magazine*, 5:507–531, 1893. doi:10.1080/14786449308620508.

[123] Andrea Sciacchitano and Bernhard Wieneke. PIV uncertainty propagation. *Meas. Sci. Technol.*, 27(8), 2016. doi:10.1088/0957-0233/27/8/084006.

[124] Iliass Azijli, Andrea Sciacchitano, Artur Ragni, Daniele Palha, and Richard P Dwight. A posteriori uncertainty quantification of PIV-based pressure data. *Exp. Fluids*, 57(72), 2016. doi:10.1007/s00348-016-2159-z.

[125] Benjamin H Timmins, Brandon M Wilson, Barton L Smith, and Pavlos P Vlachos. A method for automatic estimation of instantaneous local uncertainty in particle image velocimetry measurements. *Exp. Fluids*, 53:1133–1147, 2012. doi:10.1007/s00348-012-1341-1.

[126] John J Charonko and Pavlos P Vlachos. Estimation of uncertainty bounds for individual particle image velocimetry measurements from cross-correlation peak ratio. *Meas. Sci. Technol.*, 24(6), 2013. doi:10.1088/0957-0233/24/6/065301.

[127] Andrea Sciacchitano, Bernhard Wieneke, and Fulvio Scarano. PIV uncertainty quantification by image matching. *Meas. Sci. Technol.*, 24(4), 2013. doi:10.1088/0957-0233/24/4/045302.

[128] Bernhard Wieneke. PIV uncertainty quantification from correlation statistics. *Meas. Sci. Technol.*, 26(7), 2015. doi:10.1088/0957-0233/26/7/074002.

[129] Andrea Sciacchitano, Douglas R Neal, Barton L Smith, Scott O Warner, and Pavlos P Vlachos. Collaborative framework for PIV uncertainty quantification: comparative assessment of methods. *Meas. Sci. Technol.*, 26(7), 2015. doi:10.1088/0957-0233/26/7/074004.

[130] Peter R Hammond. Laser dye DCM, its spectral properties, synthesis and comparison with other dyes in the red. *Optics Communications*, 29(3):331–333, 1979. doi:10.1016/0030-4018(79)90111-1.

[131] Fulvio Scarano and Michel L Riethmuller. Iterative multigrid approach in PIV image processing with discrete window offset. *Exp. Fluids*, 26:513–523, 1999. doi:10.1007/s003480050318.

[132] Fulvio Scarano and Michel L Riethmuller. Advances in iterative multigrid PIV image processing. *Exp. Fluids*, 29:51–60, 2000. doi:10.1007/s003480070007.

[133] Charles B Williamham, William J Taylor, Joan M Pignocco, and Frederick D Rossini. Vapor Pressures and Boiling Points of Some Paraffin, Alkylcyclopentane, Alkylcyclohexane, and Alkylbenzene Hydrocarbons. *J. Res. Natl. Bur. Stand. (U.S.)*, 35(3):219–244, 1945. doi:10.6028/jres.035.009.

[134] Michael B Ewing and Jesus C Sanchez Ochoa. Vapor Pressures of n-Heptane Determined by Comparative Ebulliometry. *J. Chem. Eng. Data*, 50(5):1543–1547, 2005. doi:10.1021/je049562e.

[135] Vladimir Majer. Enthalpies of vaporization of pure substances modern experimental techniques and data handling. *Fluid Ph. Equilibria*, 20:93–110, 1985. doi:10.1016/0378-3812(85)90025-1.

[136] Scott E Parrish. Evaluation of Liquid and Vapor Penetration of Sprays from a Multi-Hole Gasoline Fuel Injector Operating Under Engine-Like Conditions. *SAE Int. J. Engines*, 7(2):1017–1033, 2014. doi:10.4271/2014-01-1409.

[137] Marizio Lazzaro. High-Speed Imaging of a Vaporizing GDI Spray: A Comparison between Schlieren, Shadowgraph, DBI and Scattering. *SAE Tech. Pap.*, 01:0326, 2020. doi:10.4271/2020-01-0326.

[138] Alexander Stroh, Yosuke Hasegawa, Philipp Schlatter, and Bettina Frohnapfel. Global effect of local skin friction drag reduction in spatially developing turbulent boundary layer. *J. Fluid Mech.*, 805: 303–321, 2016. doi:10.1017/jfm.2016.545.

[139] Bernhard Wieneke. Iterative reconstruction of volumetric particle distribution. *Meas. Sci. Technol.*, 24(2), 2012. doi:10.1088/0957-0233/24/2/024008.

[140] Ronald J Adrian and Chung-Sheng Yao. Pulsed laser technique application to liquid and gaseous flows and the scattering power of seed materials. *Appl. Opt.*, 24(1):42–52, 1985. doi:10.1364/AO.24.000044.

[141] Holger Nobach and Markus Honkanen. Two-dimensional Gaussian regression for sub-pixel displacement estimation in particle image velocimetry or particle position estimation in particle tracking velocimetry. *Exp. Fluids*, 38:511–515, 2005. doi:10.1007/s00348-005-0942-3.

[142] Douglas P Hart. Super-resolution PIV by recursive local-correlation. *J. Vis.*, 3:187–194, 2000. doi:10.1007/BF03182411.

[143] Matteo Novara, Daniel Schanz, Geisler Reinhard, Sebastian Gesemann, Christina Voss, and Andreas Schröder. Multi-exposed recordings for 3D Lagrangian particle tracking with Multi-Pulse Shake-The-Box. *Exp. Fluids*, 60(44), 2019. doi:10.1007/s00348-019-2692-7.

[144] Maziar Raissi, Paris Perdikaris, and George Em Karniadakis. Physics-informed neural networks: A deep learning framework for solving forward and inverse problems involving nonlinear partial differential equations. *J. Comp. Phys.*, 378:686–707, 2019. doi:10.1016/j.jcp.2018.10.045.

[145] Maziar Raissi, Yazdani Alireza, and George Em Karniadakis. Hidden fluid mechanics: Learning velocity and pressure fields from flow visualizations. *Science*, 367:1026–1030, 2020. doi:10.1126/science.aaw4741.

[146] George Em Karniadakis, Ioannis G Kevrekidis, Lu Lu, Paris Perdikaris, Sifan Wang, and Liu Yang. Physics-informed machine learning. *Nat. Rev. Phys.*, 3:422–40, 2021. doi:10.1038/s42254-021-00314-5.

[147] Shengze Cai, Zhiping Mao, Zhicheng Wang, Minglang Yin, and George Em Karniadakis. Physics-informed neural networks (PINNs) for fluid mechanics: a review. *Acta Mech. Sin.*, 2022. doi:10.1007/s10409-021-01148-1.

[148] Alexander Amini and Ava Soleimany. Introduction to Deep Learning [MOOC]. Retrieved from MIT 6.S191. *Massachusetts Institute of Technology*, 2021. URL `http://www.IntroToDeepLearning.com`.

[149] Charu C Aggarwal. *Neural Networks and Deep Learning: A Textbook*. Springer, Cham, 2018. ISBN 978-3-319-94462-3. doi:10.1007/978-3-319-94463-0.

[150] Atilim G Baydin, Barak Pearlmutter, Alexey A Radul, and Jeffrey Siskind. Automatic differentiation in machine learning: a survey. *J. Mach. Learn. Res.*, 18(153):1–43, 2018. URL `http://jmlr.org/papers/v18/17-468.html`.

[151] Xavier Glorot and Yoshua Bengio. Understanding the difficulty of training deep feedforward neural networks. *In: JMLR Workshop and Conference Proceedings, Sardinia, Italy*, 9:249–256, 2010. URL http://proceedings.mlr.press/v9/glorot10a.html.

[152] Diederik P Kingma and Jimmy Ba. Adam: A Method for Stochastic Optimization. *In: International Conference on Learning Representations, San Diego, USA*, 2014. URL https://arxiv.org/abs/1412.6980.

[153] Yeonjong Shin, Jerome Darbon, and George Em Karniadakis. On the convergence of physics informed neural networks for linear second-order elliptic and parabolic type PDEs, 2020. URL https://arxiv.org/abs/2004.01806.

[154] Frank Hutter, Jörg Lücke, and Lars Schmidt-Thieme. Fast computation of finite-time Lyapunov exponent fields for unsteady flows. *Künstl Intell*, 29:329–337, 2010. doi:10.1007/s13218-015-0381-0.

[155] George Haller and Guocheng Yuan. Lagrangian coherent structures and mixing in two-dimensional turbulence. *Phys. D: Nonlinear Phenom.*, 147(3):352–370, 2000. doi:10.1016/S0167-2789(00)00142-1.

[156] Shawn Shadden, Francois Lekien, and Jerrold Marsden. Definition and properties of Lagrangian coherent structures from finit-time Lyapunov exponents in two-dimensional aperiodic flows. *Phys. D: Nonlinear Phenom.*, 212:271–304, 2005. doi:10.1016/j.physd.2005.10.007.

[157] Steven L Brunton and Clarence W Rowley. Fast computation of finite-time Lyapunov exponent fields for unsteady flows. *Chaos*, 20: 017503, 2010. doi:10.1063/1.3270044.

[158] Frieder Kaiser, Jochen Kriegseis, and Dave Rival. The influence of edge undulation on vortex formation for low-aspect-ratio propulsors. *J. Fluid Mech.*, 883:A55, 2020. doi:10.1017/jfm.2019.908.

[159] Cameron Tropea, Alexander Yarin, and John F Foss. *Springer Handbook of Experimental Fluid Mechanics*. Springer Berlin, Heidelberg, 2007. ISBN 978-3-540-33582-5. doi:10.1007/978-3-540-30299-5.

[160] Liu Tianshu, John P Sullivan, Keisuke Asai, Christian Klein, and Yasuhiro Egami. *Pressure and Temperature Sensitive Paints*. Springer, Cham, 2021. ISBN 978-3-030-68055-8. doi:10.1007/978-3-030-68056-5.

[161] Benjamin Bork, Andreas Preusche, Florian Weckenmann, Grazia Lamanna, and Andreas Dreizler. Measurement of species concentration and estimation of temperature in the wake of evaporating n-heptane droplets at trans-critical conditions. *Proc. Combust. Inst.*, 36(2):2433–2440, 2017. ISSN 1540-7489. doi:10.1016/j.proci.2016.07.037.

[162] Robin R Jones, David C Hooper, Liwu Zhang, Daniel Wolverson, and Ventsislav K Valev. Raman Techniques: Fundamentals and Frontiers. *Nanoscale Res. Lett.*, 14(231), 2019. doi:10.1186/s11671-019-3039-2.

[163] Dana Dabiri. Digital particle image thermometry/velocimetry: a review. *Exp. Fluids*, 46:191–241, 2009. doi:10.1007/s00348-008-0590-5.

[164] Daniel Schmeling, Johannes Bosbach, and Claus Wagner. Development of Combined Particle Image Velocimetry and Particle Image Thermography for Air Flows. *In: International Heat Transfer Conference (IHTC14), Washington, DC, USA*, 2010.

[165] Daniel Schmeling, Johannes Bosbach, and Claus Wagner. Simultaneous measurement of temperature and velocity fields in convective air flows. *Meas. Sci. Technol.*, 25(3), 2014. doi:10.1088/0957-0233/25/3/035302.

[166] Satoshi Someya, Yanrong Li, and Koji Okamoto. Combined two-dimensional velocity and temperature measurements of natural convection using a high-speed camera and temperature-sensitive particles. *Exp. Fluids*, 50:65–73, 2011. doi:10.1007/s00348-010-0894-0.

[167] Alan C Eckbreth. *Laser Diagnostics for Temperature and Species in Unsteady Combustion*, pages 393–410. Springer Netherlands, Dordrecht, 1996. doi:10.1007/978-94-009-1620-3_18.

[168] Thomas Korn. Der effizienteste Weg zur CO2-Minderung: die neueste Generation von Wasserstoffverbrennungsmotoren (in German). *In:*

41. Internationales Wiener Motorensymposium, Vienna, Austria, 2: 264–277, 2020. doi:10.51202/9783186813121-II-264.

[169] Thomas Pauer, Heiko Weller, Erik Schünemann, Helmut Eichlseder, Peter Grabner, and Klaus Maria Schaffer. H2 ICE für zukünftige PKWs und leichte Nutzfahrzeuge (in German). *In: 41. Internationales Wiener Motorensymposium, Vienna, Austria*, 2:246–263, 2020. doi:10.51202/9783186813121-II-246.

Nomenclature

Dimensionles numbers

Symbol	Description
Ca	Cavitation number
Ja	Jakob number
$\overline{Ma}_\infty$	ensemble-averaged ambient Mach number
Oh	Ohnesorge number
Re	Reynolds number
Re_l	liquid Reynolds number
Re_p	particle Reynolds number
We	Weber number
We_l	liquid Weber number

Latin letters

upper case

Symbol	Description
A, A_1	cross-sectional area
A_{IW}	overlapping area of interrogation windows
B	variable
C	characteristic frequency
C_D	drag coefficient
D_{SH}	spray-hole diameter

D_α	aperture
E	variable
F_{drag}	drag
I	image intensity distribution
I_i	intensity profile of a light sheet with index i
I_{inter}	intersection intensity
I_n	noise intensity
I_p	particle image intensity
I_{p_i}	particle image intensity of a particle with index i
I_{res}	residual intensity after image matching
$\mathbf{J}_{IA}$	Jacobi matrix of a PIV-evaluated velocity field
L	objective function
L_b	share of the objective function that relates to the training of a PINN with boundary/initial conditions
L_e	share of the objective function that relates to the training of a PINN with modelling equations
L_m	share of the objective function that relates to the training of a PINN with measured velocity data
L_{SH}	spray-hole length
L_{jet}	length of the intact liquid column of a jet
L_x	spatial range in x-direction
L_y	spatial range in y-direction
L_z	spatial range in z-direction
M_i	optical magnification of the camera with index i
M_i	optical magnification for the dimension with index i
N	number of experiments/samples
N_b	number of data points used for the training of a PINN with boundary/initial conditions
N_e	number of data points used for the training of a PINN with modelling equations
N_m	number of data points used for the training of a PINN with velocities

N_k	number of neurons in the layer with index k
N_0	number of inputs of a neuron or neuronal network
N_{m+1}	number of outputs of a NN with m hidden layers
N_p	number of particles
$N_p^{(i)}$	number of particles at the exposure with index i
N_x	image resolution in x-direction
N_y	image resolution in y-direction
R	specific gas constant
$R_{u_i u_i}$	Reynolds normal stress with respect to u_i
$R_{u_i u_i,corr}$	corrected Reynolds normal stress with respect to u_i
$R_{u_i u_j}$	Reynolds shear stress with respect to u_i, u_j $(i \neq j)$
R_I	image cross-correlation function
R_{I_j}	image cross-correlation function with respect to the measurement plane with index j
$R_{I,max}$	maximum cross-correlation value
$R_{I,min}$	minimum cross-correlation value
S	Sutherland's temperature
S_i	line that describes the intersection of the image, object and principal plane of a camera with index i according to the Scheimpflug criterion
T	temperature
$\overline{T}$	ensemble-averaged temperature
T_0	reference temperature
T_c	critical temperature
T_{fuel}	fuel temperature
T_s	saturation temperature
T_∞	ambient gas temperature
$\overline{T}_\infty$	ensemble-averaged ambient gas temperature
U	object plane velocity component in X-direction
U_i	projected object plane velocity in x-direction for the camera with index i
U_{u_i}	standard uncertainty of u_i

$U_{\overline{u}_i}$	standard uncertainty of $\overline{u}_i$
$U_{\sigma_{U_{\overline{p}}}}$	standard uncertainty of $\sigma_{U_{\overline{p}}}$
$U_{\overline{U_{\overline{p}}}}$	standard uncertainty of the mean of $U_{\overline{p}}$
$\overline{U_{u_i}}$	mean of the standard uncertainty U_{u_i}
$\overline{U_{u_i}^2}$	mean square of the standard uncertainty U_{u_i}
$U_{\overline{p}}$	standard uncertainty of $\overline{p}$
$\overline{U_{\overline{p}}}$	mean standard uncertainty of $\overline{p}$
$U_{\overline{U_{u_i}^2}}$	standard uncertainty of $\overline{U_{u_i}^2}$
$U_{R_{u_i u_i}}$	standard uncertainty of $R_{u_i u_i}$
$U_{R_{u_i u_j}}$	standard uncertainty of $R_{u_i u_j}$
V	object plane velocity component in Y-direction
V_i	projected object plane velocity in y-direction for the camera with index i
$\overline{V}$	ensemble-averaged absolute velocity
$\overline{V}_\infty$	ensemble-averaged absolute ambient velocity
W	object plane velocity component in Z-direction
X	spatial coordinate
Y	spatial coordinate
Z	spatial coordinate
W	object plane velocity component in Z-direction
$\mathbf{W}^{(i)}$	tensor of weighting factors for the position with index i
$\mathbf{W}$	tensor of weighting factors
$\mathbf{W}_i$	tensor of weighting factors at the iteration with index i

lower case

Symbol	Description
a	activation function
c	circle of confusion

$c_{p,l}$	liquid heat capacity
d_e	particle image diameter
$\mathbf{d}_e$	vector describing the dimensions of a particle image
d_{e_i}	particle image dimension in i-direction
$\mathbf{d}_{e_i}$	vector describing the particle image dimensions of the particle with index i
$d_{e_{ij}}$	particle image dimension in i-direction of a particle located in measurement plane with index j
$\mathbf{d}_{e,p_j}$	vector describing the particle image dimensions of a characteristic particle image related to the measurement plane with index j
d_{ex_i}	particle image dimension in x-direction of the particle with index i
d_{ey_i}	particle image dimension in y-direction of the particle with index i
d_p	particle diameter
dt	time increment
$\mathrm{d}t_{PIV}$	interframing time
$\mathbf{dx}_{IA}$	vector describing the displacement of an IA-related particle ensemble
$\mathrm{d}x_{IA}$	displacement of an IA-related particle ensemble in x-direction
$\mathrm{d}y_{IA}$	displacement of an IA-related particle ensemble in y-direction
e_1	equation of mass conservation
$e_{2,i}$	momentum equation in i-direction
f	focal length
f	function
f_{acq}	acquisition frequency
f_i	focal length in i-direction
$\overline{f}_i$	ensemble-averaged body force in i-direction
$f_\#$	f-number
$f_{\#_i}$	f-number for i-direction

g	function
g	gravitational acceleration
h	latent heat
i	index
j	index
k	index
l	characteristic length scale
m	number of hidden layers
n, n_b, n_e, n_m	index
p	pressure
p_i	pressure at the position with index i
$\overline{p}$	ensemble-averaged pressure
p_{inj}	injection pressure
p_v	vapour pressure
p_∞	ambient gas pressure
$\overline{p}_b^{(n_b)}$	pressure boundary/initial condition with index n_b
$\hat{\overline{p}}$	predicted ensemble-averaged pressure
r_d	deformation ratio of the particle image
r_{peak_i}	cross-correlation peak ratio at the location of the particle with index i
$r_{peak,t}$	theoretical cross-correlation peak value
$\mathbf{s}$	shift vector
s_i	image distance
s_o	object distance
t	time
t_i, t_j	time with index i or j
$t_b^{(n_b)}$	time of the data point with index n_b used for the training of a PINN with boundary/initial conditions
$t_e^{(n_e)}$	time of the data point with index n_e used for the training of a PINN with modelling equations
$t_m^{(n_m)}$	time of the data point with index n_m used for the training of a PINN with measured velocity data

u	velocity in x-direction
u_{DNS}	velocity in x-direction of DNS data
u_i	image plane velocity component in x-direction of the camera with index i
u_i	velocity component with index i
$u_{i,n}$	velocity component with index i of the n^{th} sample
$\overline{u}_i$	ensemble-averaged velocity component with index i
$\overline{u}_{m_i}^{(n_m)}$	measured ensemble-averaged velocity component with index i at the data point with index n_m
u_i'	fluctuation of the velocity component with index i
$\hat{\overline{u}}_i$	predicted ensemble-averaged velocity component with index i
u_f	fluid velocity
$\overline{u_f^2}$	fluid kinetic energy
u_p	particle velocity
$\overline{u_p^2}$	particle kinetic energy
u_∞	free stream velocity in x-direction
v	specific volume
v	velocity in y-direction
v_{DNS}	velocity in y-direction of DNS data
v_i	image plane velocity component in y-direction of the camera with index i
v_l	liquid/jet velocity
v_{rel}	relative velocity
v_∞	ambient flow velocity in y-direction
x	spatial coordinate
x	pixel shift in image cross-correlation
$x_{b_i}^{(n_b)}$	spatial coordinate in the direction with index i of the data point with index n_b used for the training of a PINN with boundary/initial conditions
$x_{e_i}^{(n_e)}$	spatial coordinate in the direction with index i of the data point with index n_e used for the training of a PINN with modelling equations

$x_{m_i}^{(n_m)}$	spatial coordinate in the direction with index i of the data point with index n_m used for the training of a PINN with measured velocity data
x_j	input with index j
$\mathbf{x}$	vector of inputs
$\mathbf{x}$	image plane vector position
x_i	spatial coordinate with index i
x_i	image plane position in x-direction of the particle with index i
$\mathbf{x}_i$	image plane vector position of the particle with index i
$\mathbf{x}_i^{(j)}$	image plane vector position of the particle with index i at the time with index j
x_{IA}	x-coordinate of the IA centroid
y	spatial coordinate
y	pixel shift in image cross-correlation
y_i	image plane position in y-direction of the particle with index i
$\hat{y}$	output of a neuron
$\hat{y}_i$	output with index i
$\mathbf{y}$	known solution of a neural network
$\hat{\mathbf{y}}$	vector of the predicted solution of a neural network
w	velocity in z-direction
w_{DNS}	velocity in z-direction of DNS data
w_j	weighting factor with index j
$w_{j,i}^{(k)}$	weighting factor with indices i, j and k
w_∞	ambient flow velocity in z-direction
z	spatial coordinate
z	out-of-focus coordinate
z_{ij}	distances between the focal line with index i and the measurement plane with index j
$z_{m,j}$	value of a neuron with indices m and j

Greek letters

upper case

Symbol	Description
Δl	dual-plane spacing
Δp	differential pressure
Δp_{loss}	pressure loss
$\mathbf{\Gamma}$	set of image plane particle positions $\mathbf{x}_i$
$\mathbf{\Gamma}^{(1)}$, $\mathbf{\Gamma}^{(2)}$	set of image plane particle positions $\mathbf{x}_i$ at the first or second exposure
$\mathbf{\Lambda}$	set of particle image intensities I_{p_i}
$\mathbf{\Lambda}^{(i)}$	set of particle image intensities I_{p_i} at the exposure with index i
$\mathbf{\Omega}$	set of particle image deformations $\mathbf{d}_{e_i}$
Ψ	range of evaluation
Ψ_b	range used for the training of a PINN with boundary/initial conditions
Ψ_m	range used for the training of a PINN with measured velocity data
Θ	arbitrary quantity
$\overline{\Theta}$	ensemble-average of an arbitrary quantity

lower case

Symbol	Description
α	mutual camera angle
α_i	angles between the z-axis and the particle light ray in the xz-plane with respect to the camera with index i.
α_{SC}	spray cone angle

β_i	angles between the z-axis and the particle light ray in the yz-plane with respect to the camera with index i.
β	parameter for the approximation of particle images
χ_b	weighting factor used for the training of a PINN with boundary/initial conditions
χ_e	weighting factor used for the training of a PINN with modelling equations
χ_m	weighting factor used for the training of a PINN with measured velocity data
δ_l	light-sheet width
ϵ_{geom}	threshold of the CPI geometrical criterion
ϵ_{int}	threshold of the CPI image-matching criterion
ϵ_{corr}	threshold of the CPI cross-correlation criterion
γ	heat capacity ratio
λ	wavelength of light
μ	dynamic viscosity
μ_i	position of the light sheet with index i
μ_0	dynamic viscosity at the reference temperature T_0
μ_f	fluid dynamic viscosity
μ_l	liquid dynamic viscosity
ω_c	highest frequency
ρ	density
$\rho\overline{u_i'u_i'}$	Reynolds normal stress with respect to u_i'
$\rho\overline{u_i'u_j'}$	Reynolds shear stress with respect to u_i', u_j' $(i \neq j)$
ρ_f	fluid density
ρ_l	liquid density
ρ_p	particle density
ρ_{u_i,u_j}	cross-correlation coefficients with indices i and j
ρ_v	vapour density
φ_{SH}	spray-hole inclination angle
τ	bivariate normal distribution

θ_0	inflow thickness of a turbulent boundary flow
σ_i	standard deviation used for the characterisation of the intensity profile of a light sheet with index i
σ_{corr}	depth of correlation
σ_i	standard deviation with index i
σ_l	liquid surface tension coefficient
σ_{u_i}	standard deviation of the velocity u_i
$\sigma^2_{u_i}$	variance of the velocity u_i
$\sigma^2_{u_i u_j}$	covariance of u_i and u_j with $i \neq j$
$\sigma_{U_{\overline{p}}}$	standard deviation of $U_{\overline{p}}$
$\sigma_{U_{u_i}}$	standard deviation of the standard uncertainty U_{u_i}
σ_z	depth of field
ξ	time variable
ζ	step size of the gradient descent method

Mathematical symbols

Symbol	Description
$\partial(\dots)/\partial(\dots)$	partial derivative
$\mathrm{D}(\cdots)/\mathrm{D}t$	material derivative
$\mathrm{grad}(\cdots)$	gradient
$\max(\cdots)$	maximum
$\min(\cdots)$	minimum
$\mathbb{N}$	normal distribution
$\mathrm{O}(\cdot)$	order of magnitude

Abbreviations

Symbol	Description
APTV	Astigmatism Particle Tracking Velocimetry
BBO	Basset-Boussinesq-Oseen

C	Components
CFD	Computational Fluid Dynamics
CPI	correlation-based particle identification
CMOS	Complementary metal-oxide-semiconductor
D	Dimensions
DCM	4-(Dicyanomethylene)-2-methyl-6-(4-dimethylaminostyryl)-4H-pyran
DEHS	Di-Ethyl-Hexyl-Sebacat
DNS	Direct Numerical Simulation
DOF	depth of field
DPA	Dual-Plane Astigmatism
DPSA	Dual-Plane Stereo Astigmatism
DSPIV	Dual-Plane Stereo Particle Image Velocimetry
FOV	field of view
GDI	gasoline direct injection
GPU	graphics processing unit
HPIV	Holographic PIV
IA	interrogation area
IPR	Iterative Particle Reconstruction
IW	interrogation window
LIF	laser-induced fluorescence
LDV	laser-Doppler velocimetry
Micro-PIV	microscopic Particle Image Velocimetry
Nd:YAG	Neodymium-doped Yttrium Aluminum Garnet
OD	optical density
PDE	partial differential equation
PDV	phase-Doppler velocimetry
PINN	physics-informed neuronal network
PIV	Particle Image Velocimetry
PTV	Particle Tracking Velocimetry
PSF	point spread function

RDE	Real Driving Emissions
RMS	root mean square
SMD	Sauter mean diameter
SOI	start of injection
STB	Shake-the-box
stereo-PIV	stereoscopic Particle Image Velocimetry
Tomo-PIV	tomographic Particle Image Velocimetry
URANS	Unsteady Reynolds-Averaged Navier-Stokes
XPIV	multi-plane stereoscopic Particle Image Velocimetry

List of Figures

List of Tables

Publications and Conference Contributions

Journal publications

Nils H Kling, Jochen Kriegseis, Lars Opfer and Philipp Rogler. Pressure evaluation of spray-induced flow in the framework of a statistical approach based on URANS and ensemble averaging. *Meas. Sci. Technol.*, 30(2), 2019. doi:10.1088/1361-6501/ab12b7.

Nils H Kling, Jochen Kriegseis, Lars Opfer and Philipp Rogler. Dual-plane stereo-astigmatism: a novel method to determine the full velocity gradient tensor in planar domain. *Meas. Sci. Technol.*, 31(8), 2020. doi:10.1088/1361-6501/ab7283.

Nils H Kling, Lars Opfer, Bettina Frohnapfel, Philipp Rogler and Jochen Kriegseis. Analysis of the spray-gas interaction of a single GDI jet by means of velocimetry-based pressure evaluation. *At. Sprays*, 32(7), 2022. doi:10.1615/AtomizSpr.2022042103

Conferences

Nils H Kling, Jochen Kriegseis, Lars Opfer and Philipp Rogler. Analysis of air entrainment of gasoline direct injection (GDI) nozzles by means of time-resolved stereo fluorescence particle image velocimetry. *ICLASS 2018 14th Int. Conf. on Liquid Atomization & Spray Systems*, 2018.

Nils H Kling, Jochen Kriegseis, Lars Opfer and Philipp Rogler. Pressure evaluation of spray-induced flow by means of URANS and time-resolved stereo particle image velocimetry. *19th Int. Symp. on Applications of Laser and Imaging Techniques to Fluid Mechanics*, 2018.

Nils H Kling, Florian Haller, Jochen Kriegseis, Lars Opfer and Philipp Rogler. An assessment of the correlation-based particle identification (CPI) method in the framework of Dual-Plane Stereo-Astigmatism (DPSA). *13th International Symposium on Particle Image Velocimetry* , 2019.

Supervised student theses

Miao Zhang. Background Oriented Schlieren (BOS) und Druckvalidierung im Bereich der sprayinduzierten Strömung (in German). Master thesis, Karlsruhe Institute of Technology (KIT), Karlsruhe, January 2019.

Florian Haller. Dual Plane Stereo Astigmatism Particle Tracking Velocimetry - Evaluation of the methodology and the post-processing algorithm. Master thesis, Karlsruhe Institute of Technology (KIT), Karlsruhe, March 2019.

Kerrin Fischer. Analyse der sprayinduzierten Strömung mittels Particle Image Velocimetry (in German). Bachelor thesis, Hochschule für Angewandte Wissenschaften Hamburg (HWI), Hamburg, March 2019.